The essential role of Cytohesin-2 as a regulator of intracellular transport

Dissertation

zur

Erlangung des Doktorgrades (Dr. rer. nat.)

der

Mathematisch-Naturwissenschaftlichen Fakultät

der

Rheinischen Friedrich-Wilhelms-Universität Bonn

vorgelegt von

Carsten Küsters

aus Emmerich am Rhein

Bonn, 2024

Angefertigt mit Genehmigung der Mathematisch-Naturwissenschaftlichen
Fakultät der Rheinischen Friedrich-Wilhelms-Universität Bonn

Gutachter/Betreuer: Prof. Dr. Waldemar Kolanus
Gutachten: Prof. Dr. Jörg Höhfeld
Tag der Promotion: 18.12.2024
Erscheinungsjahr: 2025

Table of contents

Table of Figures

List of Tables

Preliminary remarks

I hereby declare that I wrote the present dissertation without sources other than indicated in this thesis and without help from third parties. The experiments presented here were designed and performed by myself, except for:

- Analysis of Nes- and Alb-Cre conditional knockout mice (Fig. 3.2B, D-J), gene expression analysis in neonatal liver tissue (Fig. 3.3B, C), lectin flow cytometry, and WFDC2 Western Blots (Fig. 3.23B, F) were performed by Dr. Bettina Jux
- Mass spectrometry and raw data analysis of differential centrifugation assays (Fig. 3.13A, B; Fig. 3.14A) were performed by Dr. Sebastian Kallabis (who also provided the respective methods section) and Anushka Kudaliyanage (Felix Meissner Lab, UKB) on a collaborative basis.
- Mass spectrometry of neonatal plasma was performed by Dr. Marc Sylvester (Core Facility Analytical Proteomics, University of Bonn). Data analysis (Fig. 3.23E) was performed by Dr. Farhad Shakeri and Andreas Buness (Core Unit for Bioinformatics Data Analysis, University of Bonn). They also provided the respective methods section.

Murine gene and protein symbols were formatted according to the guidelines of “The Journal of Clinical Investigation”.

- Genes, mRNA and genotypes: italicized, first letter capitalized (e. g. *Cyth2*)
- Proteins: non-italicized, capitalized (e. g. CYTH2)

Amino acids are written in IUPAC code.

List of abbreviations

2-DG	2-Deoxy-d-glucose
3G-isoform	3-glycine isoform
4E-BP1	Eukaryotic Translation Initiation Factor 4E Binding Protein 1
Aβ protein	Amyloid beta protein
Alb	Albumin
AMP	Adenosine monophosphate
AMPK	AMP-Activated Protein Kinase
ARF	ADP-ribosylation factor
ARL1	ADP ribosylation factor like GTPase 1
ATP	Adenosine triphosphate
BAT	Brown adipose tissue
BCA	Bicinchoninic acid
ddH_2O	Double-distilled water
BrefA	Brefeldin A
BSA	Bovine serum albumine
C1galt1	Core 1 Synthase, Glycoprotein-N-Acetylgalactosamine 3-Beta-Galactosyltransferase 1
C1galt1c1	C1GALT1 Specific Chaperone 1
CASTOR1	Cytosolic Arginine Sensor for MTORC1 Subunit 1
CCV	Clathrin-coated vesicle
CEBPa	CCAAT Enhancer Binding Protein Alpha
cDNA	complementary DNA
ConA	Concanavalin A
CRISPR/Cas9	Clustered regularly interspaced palindromic repeats/CRISPR-associated protein 9
Cyth2	Cytohesin-2
DIA	Data-independent acquisition
DNA	Desoxyribonucleic acid
dNTPs	Desoxyribonucleoside triphosphates
DOCK180/Elmo	Dedicator Of Cytokinesis 1/Engulfment And Cell Motility 1
E. coli	Escherichia coli, bacteria
EGF	Epidermal growth factor
ER	Endoplasmic reticulum
FCCP	Carbonyl cyanide-4 (trifluoromethoxy) phenylhydrazone
FCS	Fetal calf serum
Fuc	Fucose
G6PC	Glucose-6-Phosphatase
Gal	Galactose
GalNAc	N-acetylgalactosamine
GAP	GTPase-activating protein

GATOR1	GAP activity towards Rags-1
GDI	Guanine nucleotide dissociation inhibitor
GDP	Guanosine biphosphate
GEF	Guanine nucleotide exchange factor
GFP	Green fluorescent protein
GFP	Green fluorescent protein
GlcNAc	N-acetylglucosamine
GRASP	Golgi Reassembly and Stacking Protein
GRC	Genetic Resource Center
GSK3b-TIP60	Glycogen Synthase Kinase 3 Beta-Lysine Acetyltransferase 5
GTP	Guanosine triphosphate
HEK293T	Human embryonic kidney; clone 293T
HRP	Horse reddish peroxidase
HSP90-CDC37	Heat Shock Protein 90 Alpha Family Class A Member 1-Cell Division Cycle 37
JIP3	Mitogen-Activated Protein Kinase 8 Interacting Protein 3
KO	Knockout
Lamp2	Lysosome-associated membrane protein 2
LB	Lysogeny broth
LC3	Microtubule Associated Protein 1 Light Chain 3
LC-MS	Liquid chromatography-mass spectrometry
LFQ	Label-free quantified
Man	Mannose
MAPK1/MAPK3	Mitogen-Activated Protein Kinase 1/3
MEFs	Murine embryonic fibroblasts
MHC	Major histocompatibility complex
mRNA	messenger ribonucleic acid
mTOR	Mammalian target of rapamycin
mTORC1	Mammalian target of rapamycin complex 1
MTT	3-(4,5-dimethylthiazol-2-yl)-2,5-diphenyltetrauolium bromide
Myh6	Myosin Heavy Chain 6
Myo18a	Myosin XVIIIA
Myog	Myogenin
Nes	Nestin
NPC1	Niemann Pick Disease Type 1
p70S6K	Ribosomal Protein S6 Kinase B1
PAM	Protospacer adjacent motif
PFA	paraformaldehyde
PBS	Phosphate-buffered saline
PC	Principal component
PCK1	Phosphoenolpyruvate Carboxykinase 1
PCR	Polymerase chain reaction
Pen/Strep	Penicillin/Streptomycin

PFA	Paraformaldehyde
PH	Pleckstrin homology
PI3K	Phosphatidylinositide-3-Kinase
PKC	Protein kinase C
PLD	Phospholipase D
PNA	Peanut agglutinin
PCR	Polymerase chain reaction
PPM1D	Protein Phosphatase, Mg2+/Mn2+ Dependent 1D
PAM	Protospacer adjacent motif
PtdInsP	Phosphatidylinositol phosphate
RAG	Ras Related GTP Binding
RAGC	Ras Related GTP Binding C
Ran	Ras-related nuclear protein
Ras	Rat sarcoma virus
SDB-RPS	Polystyrene-divinylbenzene reversed phase sulfonate
Rheb	Ras homolog enriched in brain
RT	Room temperature
sgRNA	Single guide RNA
Sia	Sialic acid
SLC1A5	Solute Carrier Family 1 Member 5
SPF	Specific pathogen-free
TGFb	Transforming growth factor β
TGN	Trans-Golgi network
TSC	Tuberous sclerosis complex
ULK1	Unc-51 Like Autophagy Activating Kinase 1
V-ATPase	Vacuolar ATPase
Wfdc2	WAP Four-Disulfide Core Domain 2
WGA	Wheat germ agglutinin
WT	Wild type

1 Introduction

1.1 Intracellular transport

A key feature of living cells is compartmentation, the separation of the intracellular space by membranes into smaller volumes. Within these vacuoles, vesicles, and organelles physicochemical milieus are created and maintained to meet the criteria of the different biochemical reactions necessary for cellular survival and proliferation. Besides a controlled of pH and ion content, biochemical reagents and required enzymes are contained in these milieus and separated from each other. This separation allows simultaneous opposing reactions, for instance, the synthesis and consumption of ATP (adenosine triphosphate; [5]).

To reach their destiny many smaller substances diffuse over shorter distances or are transported passively by long-range fluid flows within the cell. Larger particles and many proteins rely on active, motor-driven transport [6]. Most proteins are transported in larger protein complexes or membrane-bound on vesicular structures [7]. Important example processes involving active transport are receptor signaling, endocytosis, and the secretion of proteins [8–11]. The coordination of intracellular transport requires tight regulation, and members of the *Ras* (rat sarcoma virus) superfamily of small GTPases were found to orchestrate this network, namely the subfamilies of RAB and ARF (ADP ribosylation factor) GTPases [9, 11].

1.2 The Golgi apparatus

The Golgi apparatus is considered the central organelle of the secretory pathway, which transports proteins from the site of their synthesis in the endoplasmic reticulum (ER) through the Golgi apparatus and further to the plasma membrane. About 30% of all proteins in a cell are either secreted or membrane-bound [12].

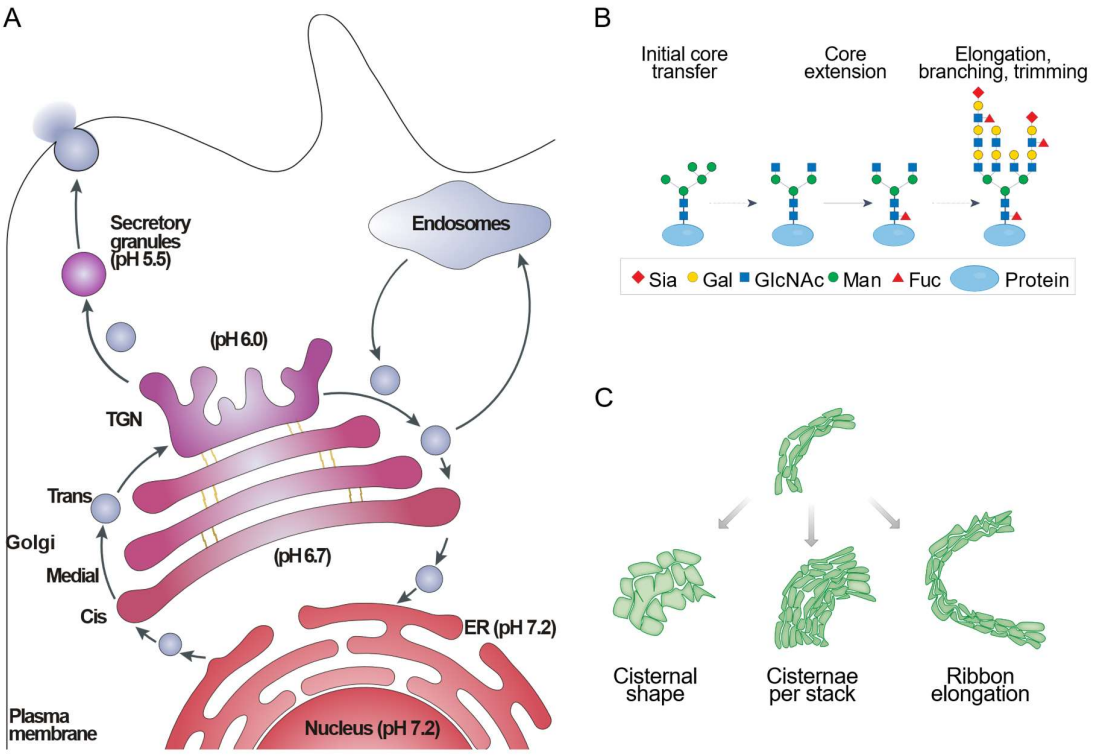

Figure 1.1: The Golgi apparatus is the central organelle of the secretory pathway
A) Scheme of the secretory pathway. Proteins synthesized at the ER pass the Golgi apparatus from the Cis-Golgi, via medial cisternae and the Trans-Golgi towards the trans-Golgi network (TGN). The TGN dispatches cargo towards the plasma membrane and exchanges material with the endosomal network. Retrograde trafficking and connections of the Golgi cisternae by golgins and GRASP proteins (yellow lines) maintain Golgi structure and functionality. The intra-luminal pH declines along the secretory pathway. ER, endoplasmic reticulum; TGN, trans-Golgi network. Modified from [1–3]. **B)** Simplified protein glycosylation as one of the posttranslational modifications occurring in the Golgi apparatus. Initially, during core transfer a sugar moiety is attached to a protein, which is extended in several steps. The final reactions create a complex and elongated glycan chain on the glycan core structure. Fuc, fucose; Gal, galactose; GlcNAc, N-acetylglucosamine; Man, mannose; Sia, sialic acid. Modified from [2]. **C)** Golgi volume and surface area are dynamic and differ between cell types and states. Cisternal shape mainly affects the Golgi volume-to-surface ratio, whereas the number of cisternae per stack, or the elongation of the Golgi ribbon increase both volume and surface area of the Golgi apparatus. Modified from [4].

Therefore, all these proteins travel through the secretory pathway. While traveling through the Golgi apparatus, proteins are posttranslationally modified. Structural or functional defects of the Golgi are implicated in various diseases and pathologic conditions such as neurodegenerative diseases, infectious diseases, and cancer [13].

1.2.1 Golgi morphology

The Golgi apparatus is a stack of flat membrane compartments, cisternae, which are connected by small, dynamic, and tubular membrane extensions, forming the Golgi ribbon (Fig. 1.1A; [14, 15]). Three distinct areas of the Golgi can be assigned: the ER-facing cis-Golgi, the medial Golgi, and the trans-Golgi. The trans-Golgi network (TGN) is not part of the Golgi apparatus, but is finally the site of vesicle exchange with the periphery [16, 17, 4].

The structural integrity of the Golgi is maintained and re-established after e.g. mitosis by golgins and members of the GRASP (Golgi Reassembly and Stacking Protein) protein family [18]. These are transmembrane proteins residing in the Golgi membranes and extend long coiled-coil domains into the cytoplasm. These tether-like extensions bind each other in homo- and heterotypic ways or via additional proteins such as ARF and RAB GTPase family members [19, 20]. The tight connection between golgins and RAB GTPases is supported by the notion that these proteins appear to be co-evolved from lower to higher eukaryotes [18].

1.2.2 Golgi function

The Golgi apparatus is a sorting complex, that not only dispatches proteins for the plasma membrane but also other destinations such as lysosomes or the endosomal compartment [4]. Sorting towards these destinations was shown to be pH-dependent [21]. Besides its role in protein sorting, the Golgi apparatus is involved in lipid biosynthesis, acts as a signaling platform for different pathways (e.g., the mTOR signaling cascade), and functions as a membrane source for dynamic adaptation of the plasma membrane [22, 23]. Another major function of the Golgi is posttranslational modification affecting protein stability, binding affinity, and localization [4]. Target proteins undergo proteolytic processing, sulfation, or glycosylation [24–26].

Glycosylation describes the enzymatic attachment of sugar moieties to C-, N-, and O-atoms of the target protein and affects about 85% of the secreted proteins (Fig. 1.1B; [27–29]). It is a cascade of core glycoside transfer, trimming, and extension of the final sugar residues, which show a broad range of complexity [28].

The highly organized structure of the Golgi ensures the correct order of reactions [25, 30]. Additionally, proper transportation of cargo but also glycosylating enzymes (glycosyltransferases) is crucial for the posttranslational modification during the Golgi passage [25, 30]. This transport involves members of the ARF and RAB GTPase family, for instance, RAB6, RAB33b, and RAB34 as well as ARF1-5, ARL1 (ADP ribosylation factor like GTPase 1), ARL3, and ARL5 [31, 32].

1.2.3 Regulation of Golgi morphology and function

Golgi size varies remarkably between cell states and cell types and reflects not only the number of cisternae but also the volume and surface of them (Fig. 1.1C; [4]). It was described that the number of Golgi cisternae is constant within one cell type, but can vary a lot between different cells. Epithelial cells usually have only a few cisternae, while specialized secreting cells often contain Golgi compartments built up from 10 to 12 cisternae [33]. In contrast, cisternal shape and volume fluctuate more often, e.g. during mitosis or differentiation [34–36].

Golgi size is often correlated with cargo load and the expression of Golgi constituents [37, 4]. It was shown that a blockage of secretion increases the volume of the TGN, which can cause a volume increase of the preceding cisternae as well [33, 16]. Further, inhibition of retrograde transport from the Golgi to the ER causes expansion of the Golgi complex [38]. Protein synthesis stimulated e.g., by certain growth factors during differentiation, leads to an increased cargo load within the ER and subsequently the Golgi. As a consequence, Golgi size increases upon growth factor stimulation, however, this occurs only transiently [4]. It was proposed that the unfolded protein response of the ER might be one mechanism accompanying the volume increase of the Golgi upon growth factor signaling, as it increases the processing capacity of the Golgi by induction of Golgi enzyme expression [39]. When the Golgi processing capacity does not suffice for the cargo load, for instance upon inhibition of glycosylation, Golgi stress can occur, leading to selective autophagy of Golgi material. Impairment of this degradation also causes an increase in Golgi volume [40–43].

The shape of Golgi cisternae is important regarding its role as a membrane source and signaling platform. The flat structure of the cisternae leads to a high surface-to-volume ratio of these compartments and it has been shown that the actin cytoskeleton and Myo18a (Myosin XVIIIA) are involved in the maintenance of that flattened conformation [44]. Regulation of the cisternal surface in response to glucose stimulation of pancreatic β-cells was reported by Noske and colleagues [45]. Additionally, preceding cytokinesis enlargement of the Golgi was observed mainly by elongation of the cisternae [46].

The tight connection between Golgi structure and function can be observed upon genetic depletion or pharmaceutic intervention disrupting the Golgi ribbon. Disruption of the Golgi ribbon can reduce secretion and lead to altered posttranslational modification of proteins, which were found in a wide range of diseases, such as viral and bacterial infections, cancer, and neurodegenerative diseases. In viral and bacterial infections, pathogens manipulate MHC (Major histocompatibility complex) class I expression for immune evasion or hijack Golgi-derived vesicles as multiplication sites [47–50]. In various cancer types changes in the Golgi apparatus alter the glycosylation of adhesion molecules, modulating the invasiveness and metastatic potential of cancer cells [51–54]. Furthermore, neurodegenerative diseases are often accompanied by fragmentation of the Golgi, which is not necessarily the cause of disease but can affect disease progression and outcome [55–57].

1.3 Endosomes

A major origin of intracellular vesicles is the plasma membrane, where surface receptors, large protein complexes, and fluid components of the extracellular space are internalized by endocytosis. Endocytic vesicles are transported to and fuse with early endosomes, the major sorting vacuole for material derived from the exterior or plasma membrane [58, 59]. From early endosomes cargo can enter the degradative route via the late endosome to lysosomes, can be recycled to the plasma membrane, or be transported towards the trans-Golgi network [58–60]. Cargo sorting and transportation by endosomes are implicated in various biological processes such as cell polarization, cell migration, and cell division [61, 62, 31, 63, 64].

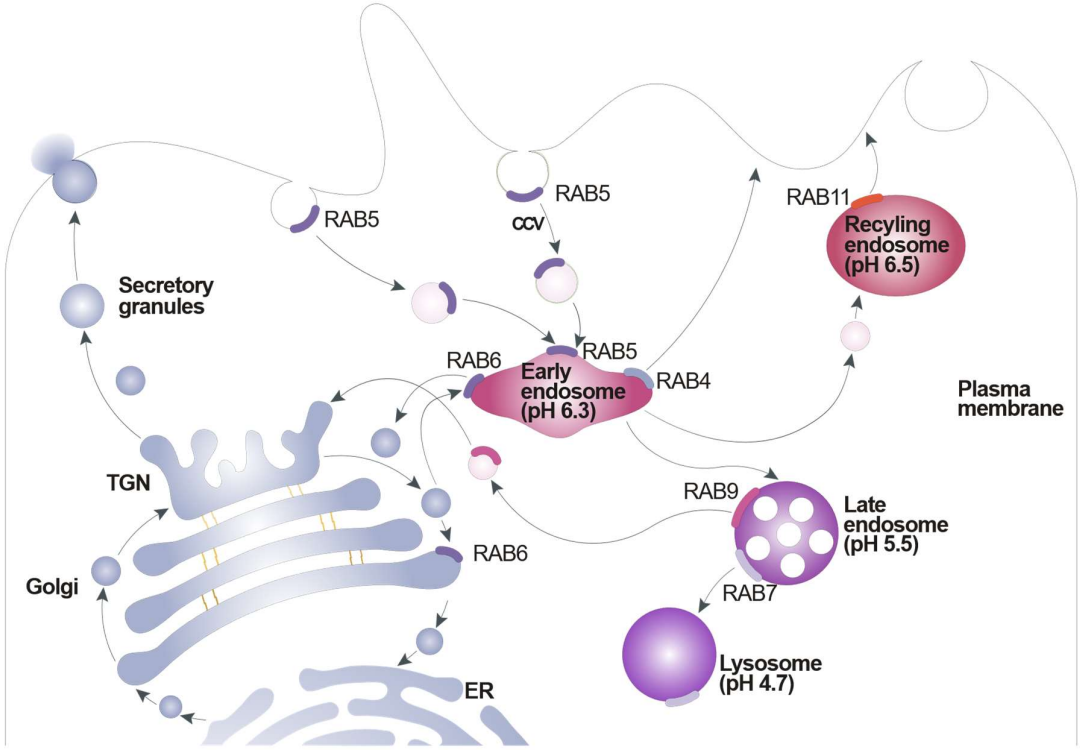

Figure 1.2: The endosomal network
Scheme of the endosomal trafficking routes including central Rab GTPases. After Rab-mediated endocytosis, cargo is transported clathrin-free or in clathrin-coated vesicles to the early endosome, also known as the sorting endosome. From the early endosome, cargo is either recycled to the plasma membrane by Rab4 (directly) and by Rab11 (through the recycling endosome), or transported to the late endosome. Late endosomal content enters the lysosome in a Rab7-dependent mechanism for degradation. Along this degradative route the intra-luminal pH decreases, while no pH-changes occur between early and recycling endosomes. Additionally, the early endosome exchanges cargo with the TGN in a Rab6-dependent mechanism and a Rab9-mediated material flow connects the late endosome with the TGN. CCV, clathrin-coated vesicle; ER, endoplasmic reticulum; TGN, trans-Golgi network. Modified from (1, 3).

1.3.1 The endosomal network

The early endosome is the first entry point of material delivered from the plasma membrane or the extracellular space, which is why it is also called the sorting endosome (Fig. 1.2; [58, 59]). RAB5 is the main GTPase associated with the early endosome and is considered a marker for this organelle [58, 59]. Transport from the early endosome to the late endosome involves the acidification of the endosomal lumen by the vacuolar ATPase (V-ATPase) and a conversion process, during which the RAB5-positive endosome acquires more RAB7 protein while losing RAB5 and its effector proteins. Finally, the RAB7-positive late endosome fuses with the lysosome for degradation of its content by lysosomal enzymes [65–67]. Alternatively, if not destined for degradation, late-endosomal content is transported in a RAB9-dependent fashion to the TGN [68]. Additionally, there are direct transport routes from the early endosome to the trans-Golgi network, mediated by RAB6 [69, 70]. Plasma membrane receptors can be recycled from early endosomes either directly controlled by RAB4, or via a RAB11-mediated transport through the recycling (also segregating) endosome [71]. Recycling of endosomal material not passing the late endosome does not require V-ATPase-mediated acidification of the endosomal lumen [58–60].

1.3.2 Regulation of the endosomal network

Endosomal numbers and size are mainly regulated by homo- and heterotypic fusion and fission events [72, 73]. Fusion of endosomal vesicles is controlled by RAB GTPases specific for a certain endosomal subcompartment, e.g. RAB5 for early endosomes, RAB7 for late endosomes, etc. [12]. How RAB GTPases shape the endosomal compartment was demonstrated by overexpression of mutant RAB5: Constitutively active RAB5 causes swelling of early endosomes and prevents the transition to late endosomes, as RAB7 is acquired but RAB5 is not removed from these large vesicles [11]. Constitutively inactive RAB5 on the other hand reduces the size of early endosomes [11]. It was also shown that blocking endocytosis by knockdown of RAB5 reduces the size and number of early endosomes and this reduction is propagated through the late endosomes to the lysosomal compartment

[73]. Physiologically, the number of early endosomes increases for instance upon treatment of cells with epidermal growth factor (EGF), which causes receptor-induced endocytosis mediated by RAB5 [74].

Besides RAB GTPases, the family of ARF GTPases plays a role in vesicle formation and thereby endosomal trafficking [32]. Palamidessi and colleagues reported that activated Rac is transported to the plasma membrane for actin remodeling in a RAB5- and ARF6-dependent manner [64]. Also, MHC class I and interleukin 2 receptor subunit alpha trafficking depend on ARF6, as well as the recycling of E-cadherin [75–77]. Moreover, endosome recycling during cytokinesis relies on ARF6 [78]. Importantly, it was shown that constitutively active ARF6 leads to enlarged endocytic vesicles and blocks the recycling of MHC class I molecules, which did not affect clathrin-dependent cargo [76].

1.4 mTOR signaling

Intracellular transport processes were also described to play a role in signaling events. Besides surface receptors such as the TGFb and EGF receptor, which rely on endosomal trafficking for full signaling activity, the mammalian target of rapamycin (mTOR) is recruited to the lysosomal surface for activation [79]. Additionally, the small GTPases ARF1 and RAB5 have both been implicated in mTOR activation in a Drosophila study [80]. In a more recent study, it was shown in mammalian cells that Arf1 is involved in the glutamine- and asparagine-dependent activation of mTOR [81].

The mammalian target of rapamycin (mTOR) is the central signaling protein to integrate metabolic information ranging from nutrient availability (amino acids, glucose), over energy levels (ATP concentration) to growth factor signals (Fig. 1.3A). Upon signaling from these sources, mTOR initiates an anabolic program leading to cell growth, proliferation, and differentiation as well as the synthesis of proteins, lipids, and DNA building blocks. However, mTOR is additionally regulated by cellular stress such as hypoxia or DNA damage. Under nutrient-poor conditions or upon stress signals, mTOR downstream targets block anabolism and initiate katabolic processes to either provide nutrients recycled from degraded cellular material or to remove the cellular stressors in terms of waste management [82–85].

The protein kinase mTOR is part of two distinct complexes, mTORC1 and mTORC2 (mammalian target of rapamycin complex 1 and 2). Both are involved in metabolic signaling and share interaction partners and constituents, but also differ in certain components and functions, for instance through their specific subunits Raptor (in mTORC1) and Rictor (in mTORC2). The mTORC1 complex is characterized by its susceptibility to rapamycin and the main metabolic switch between anabolism and catabolism. It is directly affected by amino acids, energy availability, and signaling of growth factors. In contrast, mTORC2 appears to act

A

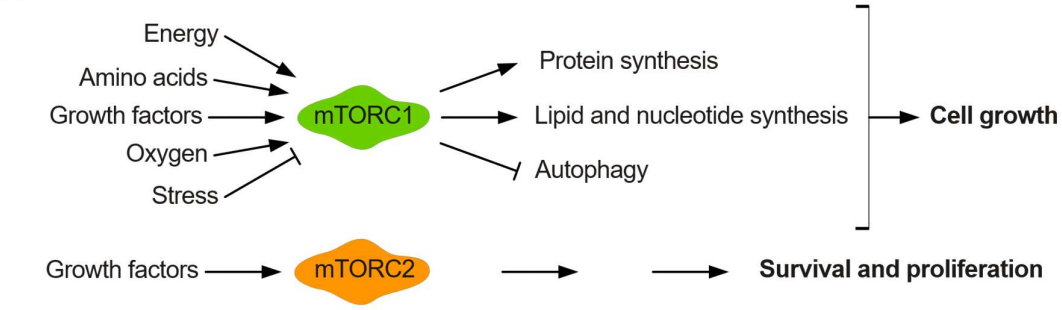

B

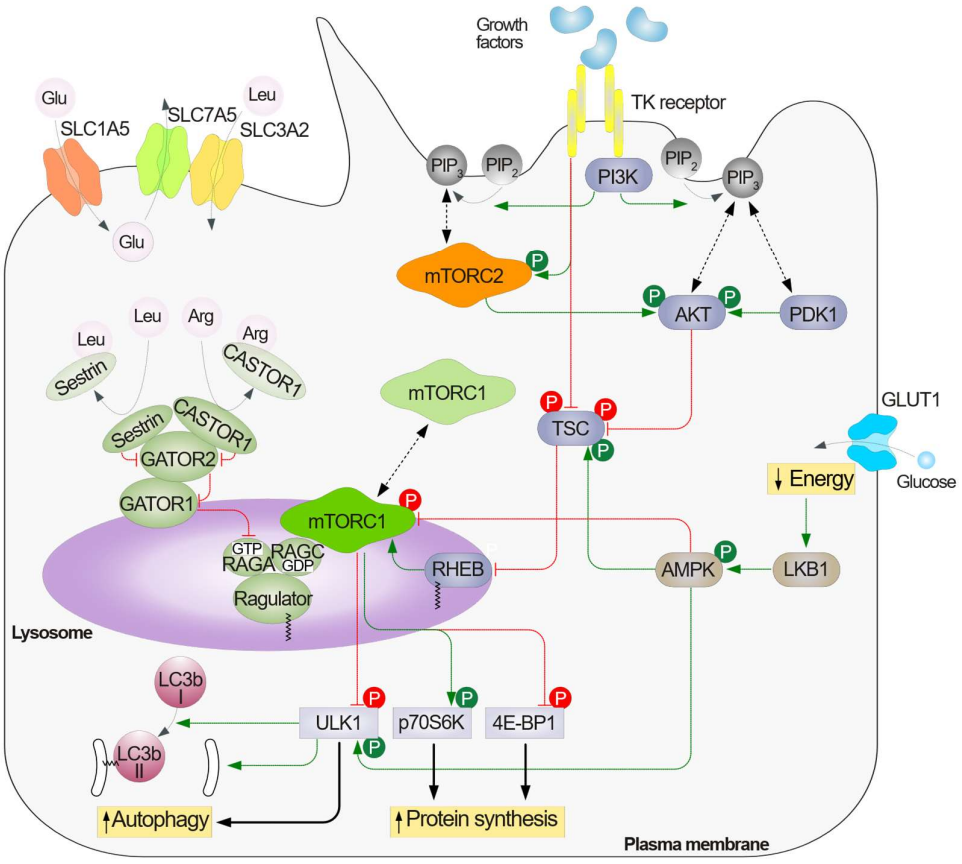

Figure 1.3: mTOR is the central coordinator of cellular metabolism
A) Mammalian target of rapamycin is part of two distinct complexes, mTORC1 and mTORC2. While mTORC1 integrates the metabolic state and the presence of growth factor or stress signals to block autophagy and initiate anabolism for cell growth, mTORC2 mainly receives growth factor signals to license the cell for survival and proliferation (85). **B)** Scheme of mTOR activation. To coordinate metabolism, mTORC1 and mTORC2 integrate a variety of stimuli: (1) Amino acids are transported into the cell (or released from lysosomal degradation of peptides) by channel and carrier proteins such as SLC7A5. Amino acid sensors such as Sestrins or CASTOR1 bind leucine or arginine, respectively, and dissociate from GATOR2. Subsequently, GATOR2 is free to block the activity of GATOR1, a GTPase-activating protein and therefore inhibitor of RagA and RagB. Consequently, under amino acid rich conditions Rag GTPases, located at the lysosomal surface by the Ragulator scaffold, remain active and recruit mTORC1. (2) Lysosome-attached Rheb, another GTPase, activates Rag-recruited mTORC1. Rheb activity is inhibited by the tuberous sclerosis complex (TSC), which is controlled and inhibited by growth factor receptors (tyrosine kinase receptors) and AKT downstream of PI3K-mediated generation of PtdIns(3,4,5)P3. AKT activity is additionally promoted by mTORC2, which is also activated by growth factor receptors and recruited to the plasma membrane upon PtdIns(3,4,5)P3 production. (3) mTORC1 activity is restricted upon depletion of amino acids or growth factors, but also upon stress signals (DNA damage, shortage of energy etc.), which often cumulate in the activation of AMPK. AMPK blocks mTORC1 activation via direct phosphorylation of the mTORC1 complex, and by promoting TSC activity and thereby Rheb inhibition. Activated mTORC1 phosphorylates downstream targets such as p70S6K and 4E-BP1 to induce protein synthesis, and ULK1 to block autophagy induction. TSC, tuberous sclerosis complex. Modified from (82).

more downstream of insulin receptor signals depending on membrane recruitment by phosphatidylinositol (3,4,5)-triphosphate (PtdIns(3,4,5)P_3). The mTORC2 complex modulates growth factor receptor signaling, fine-tunes differentiation processes and glucose homeostasis, and inhibits apoptosis. The importance of tight mTOR regulation as described below becomes apparent in cancer cells and inflammatory diseases [82–85].

1.4.1 Upstream signaling events of mTORC1

The activation of mTORC1 is associated with its recruitment to the lysosomal surface by the RAG-Ragulator complex under amino acid-rich conditions (Fig. 1.3B; [86–89]). The RAG GTPases (Ras Related GTP Binding) are under the control of the Ragulator complex, acting as a GEF for the RAG GTPases [86]. The corresponding GAP is GATOR1 (GAP activity towards Rags-1), which itself is under the control of the inhibitory protein complex GATOR2. When amino acid levels are low, amino acid sensors such as Sestrin2 and CASTOR1 (Cytosolic Arginine Sensor For MTORC1 Subunit 1) are free to bind and sequester GATOR2, which releases GATOR1 to deactivate the RAG GTPases [86, 90, 91]. Amino acid availability is partially under the control of amino acid transporters such as SLC1A5 (Solute Carrier

Family 1 Member 5), SLC7A5, and SLC3A2, which act together as a bidirectional transport system for branched and essential amino acids [92].

When mTORC1 is recruited to the lysosome under amino acid-rich conditions, it is activated by another GTPase bound to the lysosomal surface, namely RHEB (Ras homolog enriched in brain; [93, 88]). RHEB is controlled by the tuberous sclerosis complex (TSC), which acts as a GAP and inactivator for Rheb [94, 95]. However, upon growth factor signaling, the TSC is phosphorylated and inhibited, for instance by AKT [96, 97].

Additionally, AMPK (AMP-Activated Protein Kinase) can inhibit mTORC1 activation by phosphorylation of the TSC and the mTORC1 component Raptor. AMPK integrates different forms of cellular stress, acting as a break for mTORC1 signaling and an inducer of katabolic processes. Stress signals activating AMPK include e.g., insufficient energy levels (high concentrations of AMP), hypoxia, and DNA damage [98–101]. For several years now, it is under debate whether mTOR activation only occurs at the lysosomal surface or might happen e.g., at the Golgi or plasma membrane as well [102].

1.4.2 Downstream signaling events of mTOR

The mTORC1 protein complex binds its downstream targets via the Raptor subunit. Active mTORC1 phosphorylates several other proteins, the most investigated ones are probably p70S6K (Ribosomal Protein S6 Kinase B1), 4E-BP1 (Eukaryotic Translation Initiation Factor 4E Binding Protein 1), and ULK1 (Unc-51 Like Autophagy Activating Kinase 1). Phosphorylation of p70S6K leads to its activation, causing the phosphorylation of the S6 ribosomal protein and initiation of protein synthesis. Phosphorylation of both 4E-BP1 and ULK1 is inhibitory: It causes 4E-BP1 to release translation initiation factor E4 to initiate translation, and it prevents ULK1 from binding AMPK, which is one of the ULK1-activating kinases, thereby blocking the induction of autophagy. These mTOR targets contain many phosphorylation sites and the exact role and interplay of the distinct sites is not fully understood yet. However, several phosphorylation events are investigated intensely and serve as indicators for mTORC1 activity [82–85].

In contrast to the regulation of anabolism or autophagy by mTORC1, the fine-tuning of metabolism by mTORC2 is understood less, and mainly studied in cancer or diabetes, but also brain development and aging [103]. It was demonstrated in different models that interference with mTOR activity can induce the expression of *PCK1* (Phosphoenolpyruvate Carboxykinase 1) and *G6PC* (Glucose-6-Phosphatase), two enzymes involved in gluconeogenesis [104, 105]. Presumably, this regulation is based on the inhibition of mTORC2, while mTORC1 is still active, and involves modulation of AKT signaling by phosphorylation at serine residue 473 (S473; [106, 107]). Amino acids can fuel gluconeogenesis or ketogenesis. A connection between amino acids and glucose levels was already found in the 1970s when infants small for their age and with hypoglycemic blood glucose were observed to have elevated levels of branched-chain amino acids [108]. More studies in rats and humans could show that especially branched-chain amino acids improve insulin sensitivity and glucose tolerance, often accompanied by reduced gluconeogenesis [109–112]. Recent studies, especially in yeast, identified mTORC2 as a regulator of plasma membrane homeostasis, for instance by modulation of sphingolipid metabolism [113].

1.4.3 Focus on ULK1

As ULK1 is of particular interest in this thesis, the following paragraph will elaborate more on ULK1, its function, and specifically its regulation. ULK1 and its close homolog ULK2 are the main inducers of autophagy. They have partially redundant but also specific functions, as determined by *in vivo* and *in vitro* knockout (KO) models. Autophagy at basal levels is a cellular waste management process, which is induced upon starvation under the control of mTOR and AMPK. Under nutrient-rich conditions, mTORC1 phosphorylates ULK1 at multiple sites. One of these is serine residue 757 (S757), which is well investigated, serves as a marker of mTORC1 activity, and prevents the interaction of ULK1 and AMPK. Upon starvation many of these phosphorylations are removed, enabling AMPK to interact with and activate ULK1. Activated ULK1 acts as a kinase for several autophagy genes,

thereby controlling the formation of phagophores, their elongation, and finally fusion with lysosomes [114–116, 85].

Besides metabolic signaling, cellular stress can induce autophagy by activation of ULK1. Examples are ER stress, the response being mediated by GSK3b-TIP60 (Glycogen Synthase Kinase 3 Beta-Lysine Acetyltransferase 5) to prevent apoptosis [117–119], hypoxia leading to mitophagy under the control of HSP90-CDC37 (Heat Shock Protein 90 Alpha Family Class A Member 1-Cell Division Cycle 37), or genotoxic stress causing dephosphorylation of ULK1(S637) by PPM1D (Protein Phosphatase, Mg2+/Mn2+ Dependent 1D; [120, 121]). Additionally, the regulation of ULK1 involves transcriptional and translational control as well as the degradation of ULK1. Prolonged starvation, associated with prolonged autophagic activity, induces the degradation of ULK1. At the same time, it reduces its translation while increasing *Ulk1* mRNA expression [122]. In breast cancer, it was shown that MAPK1/MAPK3 (Mitogen-Activated Protein Kinase 1/3) signals cause the degradation of ULK1 [122, 123]. Importantly, degradation of ULK1 was observed in inhibitor studies to be mediated by the proteasome as well as the autophagosomal degradation route [122, 123]. Unclear is, where in the cell ULK1 is regulated by its upstream kinases and phosphatases.

1.5 Regulation of GTPases

Small GTPases are essential regulators of intracellular transport processes (see section 1.1). A common feature of small GTPases is their activation cycle, which involves the exchange of a bound GDP (guanosine diphosphate) molecule for a GTP (guanosine triphosphate) molecule (Fig. 1.4A). This activation step often requires the action of guanine nucleotide-exchange factors (GEFs), proteins binding the GDP-loaded GTPase, stabilizing its conformation, and allowing the nucleotide exchange based on higher intracellular concentrations of GTP compared to GDP. GTP-loaded GTPases are considered active and recruit effector proteins to exert specific functions. To inactivate the small GTPases, bound GTP is hydrolyzed to GDP, assisted by a GTPase-activating protein (GAP) as the intrinsic GTPase activity of the Ras superfamily members is usually very low. Simultaneously, activation

cycles of RAB and ARF GTPases involve cycles of membrane binding and dissociation. Active ARF GTPases attach to membranes with an N-terminal myristolated domain, which becomes inaccessible upon GTP-hydrolysis leading to membrane dissociation of the GTPase. In the case of RAB GTPases, the prenylated C-terminus facilitates the membrane recruitment, masked in the GDP-loaded form by another set of regulatory proteins, RAB GDP dissociation inhibitors (GDIs). Based on their specific recruitment, ARF- and especially RAB GTPases not only orchestrate vesicular transport but also create the identity of the bound structures (see section 1.3.1; [8–11, 32]).

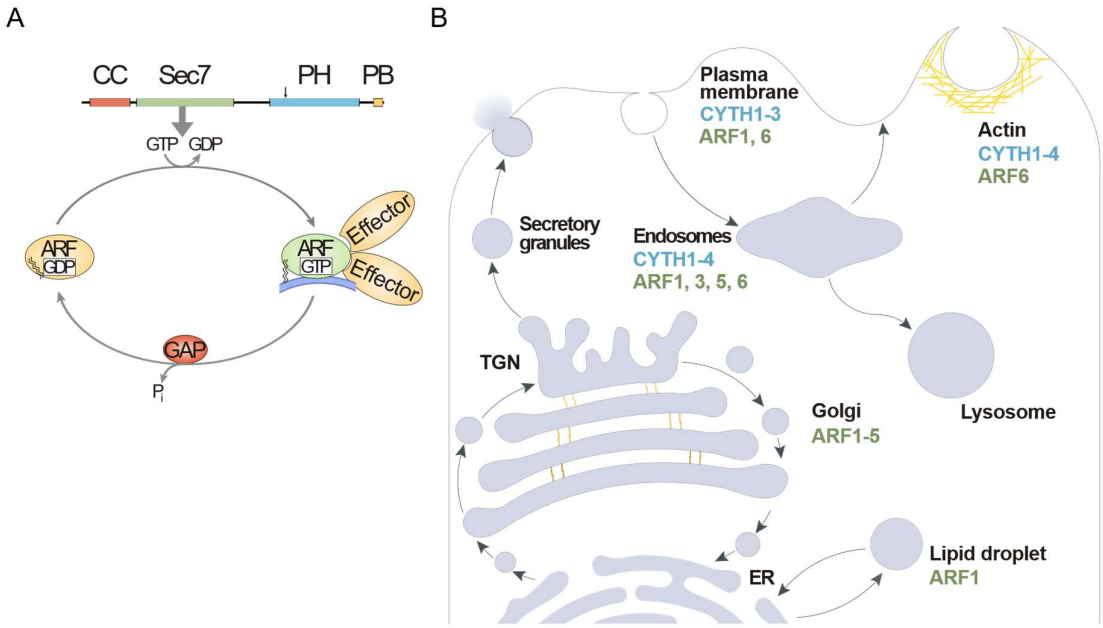

Figure 1.4: ARF GTPases and cytohesins regulating membrane traffic and cortical actin
A) Protein domain structure of Cyth2 with the N-terminal coiled-coil domain, the C-terminal PH domain and polybasic motif, and the central Sec7 domain. The small arrow indicates the position of the isoform-specific 2G/3G motif. The Sec7 domain activates Arf GTPases (ARF1/6 as detected in cell-based assays; biochemical promiscuity for all ARF-GTPases), promoting the nucleotide exchange of the GTPase from GDP-bound to a GTP-bound state. This activation leads to membrane attachment of the Arf GTPase and recruitment of effector proteins. Arf GAPs promote the hydrolase activity of the GTPases, leading to the conversion of GTP to GDP and the inactivation of the Arf GTPase. The GTPase undergoes a conformational change masking the lipid anchor and dissociating from the membrane. **B)** Different Arf GTPases have been detected at diverse sites within the cell, suggesting unique and partially redundant functions of these proteins. Most of them were found attached to the Golgi compartment and endosomal vacuoles. Worth noting, Arf1 is unique at lipid droplets, Arf1 and Arf6 are so far the only two Arf GTPases found at the plasma membrane, and Arf6 seems to play an exclusive role in the regulation of the cortical actin cytoskeleton. Cytohesins were found at endosomes and the plasma membrane, and were described to regulate the cortical actin cytoskeleton. Modified from (11, 32).

1.6 Cytohesin-2

Small GTPases control many processes in cells and their activity is regulated by GEF and GAP proteins. A group of cytosolic ARF GEFs was identified at the end of the last century, the cytohesin protein family with its four members cytohesin-1 to -4 (CYTH1-4; [124–127]). While CYTH1 was initially described as an interactor of β2-integrins, in cell-free assays all cytohesins were identified as potential ARF GEFs. They belong to the group of small ARF GEFs and are therefore unaffected by the inhibitor Brefeldin A (BrefA), a Golgi-disrupting substance known to block ARF activation by the group of large ARF GEFs [128].

1.6.1 CYTH2 structure and isoforms

All cytohesin proteins comprise a central Sec7 domain, which is homologous to the yeast Sec7 protein and facilitates the GEF function for ARF GTPases (Fig. 1.4A). The Sec7 domain is flanked by an N-terminal coiled-coil domain and a C-terminal pleckstrin homology (PH) domain. Additionally, a polybasic motif was described at the far C-terminus of the cytohesin family members [129].

The coiled-coil domain is involved in protein-protein interactions and was described to be sufficient but also required for CYTH2 targeting to the Golgi apparatus [130–133]. However, recruitment of cytohesins was mainly observed at the plasma membrane, mediated by the PH domain, which binds phosphatidylinositol phosphates (PtdInsPs) produced for instance by PI3K (Phosphatidylinositide-3-Kinase; [134]). The PH domain of cytohesins is expressed in two isoforms, which differ solely in a single glycine residue. While the 3-glycine-isoform (3G-isoform) binds to both PtdIns(4,5)P_2 and PtdIns(3,4,5)P_3, the 2G-isoform shows a clear preference for PtdIns(3,4,5)P_3 [135]. This phenomenon was structurally delineated in 2004 by Cronin and colleagues [136]. It was further reported that activated ARF1 and ARF6 (GTP-loaded) and ARL4 are able to recruit cytohesin proteins through interaction with the cytohesin PH domain [137, 138]. The recruitment of cytohesins by activated ARF GTPases suggests the potential for a positive feedback loop [139, 138]. As the Sec7 domain of cytohesins shows promiscuity towards ARF1 and ARF6 in cell-free activation assays, their intracellular

specificity might depend on the recruiting interaction partner [124, 140, 141]. Finally, the polybasic motif at the far C-terminus of cytohesins was reported to autoinhibit their activity towards ARF GTPases. Cytohesins fulfill their GEF activity only when the autoinhibited state is released by binding to PtdInsPs or as mentioned activated ARF1, ARF6, or ARL4 [137]. DiNitto could additionally show that cytohesin activity is promoted by PKC-dependent (Protein kinase C) phosphorylation events at the poly-basic motif [142].

1.6.2 CYTH2 function

The present study focuses on *Cyth2* and while the cytohesins share a common domain structure, their functional implications are rather diverse (Fig. 1.4B). CYTH2 was reported to activate ARF6 at the plasma membrane, leading to the recruitment of a DOCK180/Elmo (Dedicator Of Cytokinesis 1/Engulfment And Cell Motility 1) complex, which further activates Rac1 to reorganize the cortical actin cytoskeleton [143]. Rac1 activation in concert with PLD (Phospholipase D) activity downstream of CYTH2-ARF6 signaling was shown to stimulate the migration of epithelial cells [144].

CYTH2-mediated activation of ARF1 at the plasma membrane was observed to be involved in macropinosome formation and infection of cells with Salmonella [145]. Besides its activity at the plasma membrane, CYTH2 was found to associate with the V-ATPase. The endosomal proton pump recruits CYTH2 in a pH-dependent manner and also interacts with ARF6. Interference with the recruitment of CYTH2 to the V-ATPase or with CYTH2 GEF activity was shown to reduce endocytosis [146]. Impairment of the endocytic pathway by loss of *Cyth2* was additionally found in an influenza infection model [147]. Depletion of *Cyth2* seemed to reduce the transport of viral particles from early to late endosomes, thereby decreasing viral replication. *In vivo,* infection experiments could further show that cytohesin inhibition with SecinH3 delayed disease progression in mice [147]. CYTH2-ARF6-dependent membrane trafficking was further proposed to feed into the autophagic degradation pathway, as siRNA-mediated depletion of either protein reduced the conversion of LC3 (Microtubule Associated Protein 1 Light Chain 3 Alpha), a key process during autophagosome formation [148].

The cytohesin family was also associated with insulin receptor signaling, as the pan-cytohesin inhibitor SecinH3 hampered hepatic insulin signaling [149]. Genetic studies in Drosophila and mice investigating the role of steppke (cytohesin homolog in the fruit fly) and *Cyth3*, respectively, supported these observations: steppke mutants showed growth defects and decreased activation of AKT in larvae [150], *Cyth3*-deficient mice had impaired insulin signaling in liver tissue [151]. Whether CYTH2 is involved in growth factor signaling as well remains elusive.

Early studies of the cytohesin family could show that the coiled-coil domain of CYTH1 and CYTH2 associates with the Golgi apparatus or a Golgi-like compartment, respectively [146, 132]. In cell-free activation assays CYTH1-3 were able to activate ARF1, the ARF GTPase mainly associated with Golgi function, and overexpression experiments with CYTH3 and CYTH2 caused Golgi fragmentation and a blockage of the secretory pathway [152, 153]. Whether these observations are biologically relevant or artificial products of the respective experimental conditions remains to be investigated.

During *in vivo* experiments with KO mice for *Cyth1* and *Cyth2* (the latter being Schwann cell-specific), reduced activation of ARF6 was observed in the nervous system as well as decreased myelin thickness and production of myelin protein zero [154, 155]. In inflammatory and neuropathic pain models, central nervous system-specific loss of *Cyth2* in mice reduced mechanical allodynia, a condition of pain sensation due to “innocuous stimuli” [156, 157]. Recently, it was observed that *Cyth2*-deficient mice display reduced eosinophilic inflammation in an ovalbumin-induced rhinitis model [158]. While these studies contribute to the understanding of the *in vivo* role of *Cyth2*, they did not link the cellular phenotypes described earlier to their *in vivo* observations. Despite the proof of ARF-GTPase activation downstream of CYTH2, the subsequent cellular processes were not investigated. Speculations attribute the CYTH2-ARF6 effects mainly to the rearrangement of the cytoskeleton with an involvment of Rac1, the ELMO/DOCK complex and JIP3 and 4 (Mitogen-Activated Protein Kinase 8 Interacting Protein 3 and 4) and vaguely to membrane trafficking [156, 154, 155].

1.7 Aim of the study

The role of *Cyth2* and its protein family members was intensively studied *in vitro*, and a variety of cellular processes seem to be affected by the small ARF-GEFs. *Cyth2* was associated with cortical actin organization, the endocytic pathway, and growth factor receptor signaling [150, 146, 151, 148, 143]. However, *in vivo* studies about the role of *Cyth2* are sparse and report only minor consequences of the genetic depletion of *Cyth2* in mice, despite broader implications for the protein in cell systems [157, 156, 158, 154]. Additionally, the *in vivo* observations are barely linked to cellular phenotypes reported before.

The present study intends to remedy this desideratum, analyzing the phenotype of conventional *Cyth2*-deficient mice, which were previously generated by Dr. Bettina Jux. Live-observations coupled with gross anatomical examination and biochemical approaches were used to access the health state of mice after *Cyth2* depletion. To support the interpretation of the *Cyth2* deficiency phenotype, tissue-specific *Cyth2* knockout mice were exploited for comparison. Aiming to link the *in vivo* observations with cellular processes and a molecular mechanism, the CRISPR/Cas9 system was utilized to generate *Cyth2*-deficient cell lines. *In vitro* assays were conducted in accordance with the murine phenotype.

As the cellular function of *Cyth2* was diversely described, and ARF GTPases and their regulators have always been associated with transport processes, a central goal of this study was the identification of these transport processes and the organelles affected by *Cyth2*. Therefore, an unbiased and global organellar fractioning approach was chosen, separating organelles and cellular compartments based on their precipitation and identifying precipitated proteins by mass spectrometry. Simultaneously, this approach aimed to assess the cellular distribution of CYTH2. For the purpose of validation and further investigation, immunofluorescence analysis was chosen to describe morphological changes of identified organelles in various cell types. In order to delineate the requirement for CYTH2 GEF activity regulating cellular transport mechanisms, inhibitor assays with SecinH3 and rescue experiments with GEF-silent mutants of *Cyth2* were performed.

Finally, to transfer the *in vitro* findings to the murine phenotype, functional consequences were assessed and *in vitro* as well as *in vivo* findings were evaluated as potential causes for the murine phenotype.

2 Material and methods

2.1 Material

2.1.1.1 Devices

Device	Model, company (office)
Autoclave	135T, H + P Medizintechnik (Oberschleißheim, Germany)
	DX-150, Systec (Linden, Germany)
Balance	JB2002-G/FACT, Mettler Toledo (Greifensee, Switzerland)
	AG285, Mettler Toledo (Greifensee, Switzerland)
Binocular	Wild Heerbrugg (Bad Dürkheim, Germany)
Blood glucose meter	ACCU-CHEK® Aviva Nano, Roche (Mannheim, Germany)
Blotting equipment	Mini Trans-Blot Cell, Bio-Rad (Munich, Germany)
Centrifuge	Avanti J-20XP, Beckman Coulter (Munich, Germany)
	5810R, 5424 and 5415R, Eppendorf (Hamburg, Germany)
CO_2 incubator	CB, Binder (Tuttlingen, Germany)
	EcoCell 55, MMM Medcenter (Munich)
Dounce homogenisator	VWR (Darmstadt, Germany
Dissecting set	FST Dumont Biology (Heidelberg, Germany)
High-performing liquid	Dionex Ultimate 3000 RSLC nano, Dionex (Idstein, Germany)
chromatography system	Easy nLC 1200, Thermo Fisher Scientific (Waltham, USA)
Electropheresis chamber	Polymehr (Paderborn, Germany)
(agarose gels)	
Electropheresis chamber (SDS-	Mini Trans-Blot Cell, Bio-Rad (Munich, Germany)
PAGE)	
Electroporator	Gene Pulser Xcell, Bio-Rad (Munich, Germany)
Flow cytometer	LSR, BD Bioscience (Heidelberg, Germany)
Gel documentation	Gel Max, Intas (Göttingen, Germany)
Heat block	Thermomixer compact, Eppendorf (Hamburg, Germany)
Laminar flow hood	BioFlow, BDK (Sonnenbühl-Genkingen, Germany)
	HeraSafe KS, Thermo Scientific (Waltham, USA)
	BioAir ®, Euroclone Division (Pero, Italy)
Liquid chromatrography (LC)	Easy nLC 1200, Thermo Fisher Scientific (Waltham, USA)
system	Dionex Ultimate 3000 RSLC, Dionex GmbH (Idstein, Germany)
Magnetic stirrer	Combimac RCT, IKA (Staufen, Germany)
Magnetic stirrer	ARE heating magnetic stirrer, VELP scientica (Usmate, Italy)
Mass spectrometer	Exploris 480, Thermo Fisher Scientific (Waltham, USA)

	Orbitrap Fusion Lumos, Thermo Fisher Scientific (Bremen, Germany)
Microplate reader	Infinite M200, Tecan (Männedorf, Switzerland)
Microscope	Axiovert 100, Zeiss (Jena, Germany)
	LSM 880+ Airyscan, Zeiss (Jena, Germany)
Neubauer chamber	Marienfeld (Lauda-Königshofen, Germany)
Orbital shaker	innova44, New Brunswick, Eppendorf (Hamburg, Germany)
Orbital shaker	Stuart SI500 Incubator, orbital shaker (Keison Products, Chelmsford, UK)
PCR cycler	Vapoprotect, Eppendorf (Hamburg, Germany)
	Biometra T3 Thermocycler, Analytik Jena (Jena, Germany)
	C1000 Touch Thermal Cycler, Bio-Rad (Munich, Germany)
PH meter	MP220, Mettler Toledo (Greifensee, Switzerland)
Pipette controller	Pipetus-Akku, Hirschmann Laborgeräte (Eberstadt, Germany)
	Accu-jet pro, Brand (Wertheim, Germany)
Pipettes	ErgoLine, StarLab (Helsinki, Finland)
	Pipetman Classic, Gilson (Middleton, USA)
Power supply	EV-243, Consort (Turnhout, Belgium)
	Elite300Plus, Schütt Labortechnik (Göttingen, Germany)
Real-time PCR cycler	CFX96, Bio-Rad (Munich, Germany)
Rocker	WS-10, Edmund Bühler (Hechingen, Germany)
Roller mixer	RS-TR05, Phoenix Instrument (Garbsen, Germany)
Rotation wheel	Neolab Rotator, Neolab (Heidelberg, Germany)
Scanner	CanoScan 9000F Mark II, Canon (Tokio, Japan)
Seahorse analyzer	Seahorse XFe96 Analyzer, Agilent (Santa Clara, USA)
Spectrophotometer	NanoDrop 2000, Thermo Scientific (Waltham, USA)
Tissue homogenizer	Precellys, Bertin (Rockville, USA)
Ultracentrifuge	Optima LE-80K Ultracentrifuge, Beckman Coulter (Munich, Germany)
Vacuum pump	AC02, HLC BioTech (Bovenden, Germany)
Vortex mixer	UNIMAG ZX3, VELP scientica (Milan, Italy)
Waterbath	WNE, Memmert (Schwabach, Germany)

2.1.1.2 Consumables

Consumable	Model, company (office)
Analytical column (MS)	30 cm, 75 µm diameter, 1.9 µm ReproSil-Pur 120 C18-AQ, Dr. Maisch (Ammerbuch-Entringen, Germany) 40 cm, 75 µm diameter, 3 µm ReproSil-Pur 120 C18-AQ, Dr. Maisch (Ammerbuch-Entringen, Germany)
Blood collection tubes	Microvette® CB 300 µl, Lithium-Heparin, Sarstedt (Nümbrecht, Germany)
Blood glucose test strips	ACCU-CHEK® Aviva, Roche (Mannheim, Germany)
Capillary tips	Roth (Karlsruhe, Germany)
Cell culture plates and multiwell plates	Greiner Bio-one (Frickenhausen, Germany)
Cell scaper 25 cm	Cell Scraper 2-Posit. Blade 25, Sarstedt (Nümbrecht, Germany)
Cell strainer	EASYstrainer 70 µm, Greiner Bio-one (Frickenhausen, Germany)
Cell strainer	EASYstrainer 40 µm, Greiner Bio-one (Frickenhausen, Germany)
Cover slips	Marienfeld GmbH (Lauda-Königshofen, Germany)
Electroporation cuvettes	4 mm, Biozym (Vienna, Austria)
Falcon tubes	Greiner Bio-one (Frickenhausen, Germany)
Filter paper	Whatman No.4, Schleicher and Schuell (Dassel, Germany)
Filter tips	10/200/1000 µl, Sarstedt (Nümbrecht, Germany)
Flow cytometry tubes	Sarstedt (Nümbrecht, Germany)
Glass beads (acid-washed)	Sigma-Aldrich (St. Louis, USA)
Glass pasteur pipettes	Brand (Wertheim, Germany)
Micro tubes	2 ml, Sarstedt (Nümbrecht, Germany)
Microscope slides	Marienfeld (Lauda-Königshofen, Germany)
Needles	sterican, Braun Melsungen (Melsungen, Germany)
Nitrocellulose membrane	BioTrace NT nitrocellulose membrane, Pall Corporation (Pensacola, USA)
Parafilm	Bemis (Neenah, USA)
PCR tubes	200 µl Thin Wall Tubes, Axygen (Tewksbury, USA)
Petri dishes	10 cm, Greiner Bio-one (Frickenhausen, Germany)
Pipette tips	10/200/1000 µl, Carl Roth (Karlsruhe, Germany)
polystyrene-divinylbenzene reversed phase sulfonate double-layer stage tips	In-house production; Affinisep (Le Houlme, Frankreich)
Radiographic film	Hyperfilm MP, Amersham Biosciences (Buckinghamshire, UK)

Reaction tubes	0.5/1/2 ml, Starlab (Ahrensburg, Germany)
RT-PCR plates	Bio-Rad (Munich, Germany)
RT-PCR seals	Bio-Rad (Munich, Germany)
Seahorse consumables	Seahorse Flux Paks, Agilent (Santa Clara, USA)
Serological pipettes	5/10/25 ml, Greiner Bio-one (Frickenhausen, Germany)
Stage tips	SDB-RPS, Affinisep (Le Houlme, France)
Sterile filters	0.2 and 0.45 µm, Schleicher and Schuell (Dassel, Germany)
Syringes	Braun (Melsungen, Germany)
Tubes for ultracentrifugation	QuickSeal Polypropylene, Beckman (Munich, Germany)

2.1.1.3 Chemicals

Reagent	Company (office)
2-Mercaptoethanol	Roth (Karlsruhe, Germany)
Acetic acid	Carl Roth (Karlsruhe, Germany)
Acetone	Carl Roth (Karlsruhe, Germany)
Acetonitrile	Sigma-Aldrich Chemie (Munic, Germany)
Acrylamide/Bisacrylamide solution (30%)	Roth (Karlsruhe, Germany)
Agarose	Invitrogen/Life Technologies (Carlsbad, USA)
Ammonium acetate	Carl Roth (Karlsruhe, Germany)
Ammonium chloride (NH_4Cl)	Sigma-Aldrich (St. Louis, USA)
Ammonium persulfate (APS)	Roth (Karlsruhe, Germany)
Ampicillin	Carl Roth (Karlsruhe, Germany)
Antipain	Sigma-Aldrich (St. Louis, USA)
Aprotinin	Carl Roth (Karlsruhe, Germany)
Benzamidin	Sigma-Aldrich (St. Louis, USA)
Beta-Glyerolphosphate	Sigma-Aldrich (St. Louis, USA)
Bovine serum albumin (BSA)	Roth (Karlsruhe, Germany)
Bromphenol blue	Roth (Karlsruhe, Germany)
Butanol	Carl Roth (Karlsruhe, Germany)
Caesium chloride	Carl Roth (Karlsruhe, Germany)
Calcium chloride anhydrous	Carl Roth (Karlsruhe, Germany)
Calcium phosphate	Carl Roth (Karlsruhe, Germany)
Chloroform	Roth (Karlsruhe, Germany)
Deoxynucleotides (dNTPs)	Thermo Fisher Scientific (Waltham, USA)
Developing solution (Adefo Citroline2000)	Adefo-Chemie (Neu-Isenburg, Germany)

Diamidinophenylindole (DAPI)	Sigma-Aldrich (Taufkirchen, Germany)
Dimethyl sulfoxide (DMSO)	Roth (Karlsruhe, Germany)
Disodium phosphate (Na_2HPO_4)	Carl Roth (Karlsruhe, Germany)
Dithiothreit (DTT)	Carl Roth (Karlsruhe, Germany)
DNA loading dye (6x)	Thermo Scientific (Waltham, USA)
Ethanol	VWR (Darmstadt, Germany)
Ethidium bromide	Carl Roth (Karlsruhe, Germany)
Ethylenediaminetetraacetic acid (EDTA)	Sigma-Aldrich (St. Louis, USA)
Ethyleneglycotetraacetic acid (EGTA)	Sigma-Aldrich (Taufkirchen, Germany)
Fibronectin	Sigma-Aldrich (Taufkirchen, Germany)
Formic acid	Sigma-Aldrich Chemie (Munic, Germany)
Glucose	Carl Roth (Karlsruhe, Germany)
Glycerol	Grüssing (Filsum, Germany)
Glycine	Carl Roth (Karlsruhe, Germany)
HEPES	Carl Roth (Karlsruhe, Germany)
Hydrochloric acid (HCl)	Roth (Karlsruhe, Germany)
Igepal CA-630	Sigma-Aldrich (St. Louis, USA)
Iron (III) nitrate x $9H_2O$	Sigma-Aldrich (Taufkirchen, Germany)
Isopropanol	VWR (Darmstadt, Germany)
L-amino acids	Sigma-Aldrich (Taufkirchen, Germany)
LB-Agar	GIBCO/Life Technologies (Carlsbad, USA)
Leupeptin	Carl Roth (Karlsruhe, Germany)
linear polyacrylamide (LPA)	GenElute LPA, Merck (Darmstadt, Germany)
Magnesium chloride ($MgCl_2$)	Carl Roth (Karlsruhe, Germany)
Magnesium sulfate anhydrous	Carl Roth (Karlsruhe, Germany)
Methanol	VWR (Darmstadt, Germany
Milk powder	Roth (Karlsruhe, Germany)
Mounting medium (fluoroshield)	ImmunoBioScience (Mukilteo, USA)
natrium deoxycholate	Carl Roth (Karlsruhe, Germany)
Paraformaldehyde (PFA)	Roth (Karlsruhe, Germany)
Phenol	Carl Roth (Karlsruhe, Germany)
Phenylmethylsulfonyl fluoride (PMSF)	Carl Roth (Karlsruhe, Germany)
Ponceau S	Roth (Karlsruhe, Germany)
Potassium acetate	Carl Roth (Karlsruhe, Germany)
Potassium bicarbonate	Sigma-Aldrich (Taufkirchen, Germany)
Potassium chloride (KCl)	Carl Roth (Karlsruhe, Germany)
RNA loading dye (2x)	New England Biolabs (Ipswich, USA)
Saccharose	Carl Roth (Karlsruhe, Germany)

Sodium acetate	Carl Roth (Karlsruhe, Germany)
Sodium azide (NaN_3)	Roth (Karlsruhe, Germany)
Sodium chloride (NaCl)	Carl Roth (Karlsruhe, Germany)
Sodium deoxycholate (Na-Doc)	Carl Roth (Karlsruhe, Germany)
Sodium dihydrogen phosphate 2x H_2O	Carl Roth (Karlsruhe, Germany)
Sodium dodecyl sulfate (SDS)	Roth (Karlsruhe, Germany)
Sodium fluoride (NaF)	Carl Roth (Karlsruhe, Germany)
Sodium hydroxide (NaOH)	Carl Roth (Karlsruhe, Germany)
Sodium pyrophosphate	Sigma-Aldrich (Taufkirchen, Germany)
Sodium vanadate	Sigma-Aldrich (Taufkirchen, Germany)
Tetramethylethylendiamine (TEMED)	Sigma-Aldrich (Taufkirchen, Germany)
Tris	Carl Roth (Karlsruhe, Germany)
Triton X-100	Roth (Karlsruhe, Germany)
TRIzol Reagent	Thermo Scientific (Waltham, USA)
Trypanblue solution	Sigma-Aldrich (St. Louis, USA)
Tween20	Carl Roth (Karlsruhe, Germany)
Water, molecular biology reagent	Sigma-Aldrich (Taufkirchen, Germany)

2.1.1.4 Kits and enzymes

Product	Company (office)
BsmBI-v2	New England Biolabs (Ipswich, USA)
CyQUANT™ NF Cell Proliferation Assay	Thermo Fisher Scientific (Waltham, USA)
DNAse I	Thermo Fisher Scientific (Waltham, USA)
Dreamtaq DNA Polymerase (+Buffer)	Thermo Scientic (Waltham, USA)
Gene Ruler 1 kb DNA ladder	Thermo Fisher Scientific (Waltham, USA)
Gene ruler 100 bp DNA ladder	Thermo Fisher Scientific (Waltham, USA)
High-Capacity cDNA Reverse Transcription Kit	Applied Biosystems/Life Technologies (Carlsbad, USA)
iST 96x sample preparation kit	Preomics (Martinsried, Germany)
iTaq Universal SYBR Green Supermix	Bio-Rad (Munich, Germany)
L-Amino Acid Quantitation Kits (MAK002)	Sigma-Aldrich (Taufkirchen, Germany)
NucleoSpin Gel&PCR Clean-up Kit	Macherey-Nagel (Düren, Germany)
Phusion high fidelity polymerase	New England Biolabs (Ipswich, USA)
Pierce BCA Protein Assay Kit	Thermo Fisher Scientific (Waltham, USA)

Pierce ECL Plus Western Blotting Substrate	Thermo Fisher Scientific (Waltham, USA)
Precision Plus Protein All Blue Standard	Bio-Rad (Munich, Germany)
Rnase A	Thermo Fisher Scientific (Waltham, USA)
T4 DNA ligase (+ buffer)	New England Biolabs (Ipswich, USA)
T4 PNK	New England Biolabs (Ipswich, USA)
Trypsin/Lys-C	Promega (Walldorf, Germany)

2.1.2 Cell culture reagents

2.1.2.1 Media and supplements

Product	Company (office)
2-Mercaptoethanol	Thermo Fisher Scientific (Waltham, USA)
dialized FCS (26400044)	Invitrogen/Life Technologies (Carlsbad, USA)
DMEM (P04-01159)	PAN-Biotech (Aidenbach, Germany)
DMEM (P04-03550)	PAN-Biotech (Aidenbach, Germany)
Dimethyl sulfoxide (DMSO)	Carl Roth (Karlsruhe, Germany)
Ethylenediaminetetraacetic acid (EDTA)	Merck (Darmstadt, Germany)
fetal calf serum (FCS), heat-inactivated	Sigma-Aldrich (St. Louis, USA)
Glucose solution	PAN-Biotech (Aidenbach, Germany)
Hank's balanced salt solution (HBSS) + Ca^{2+}	PAN-Biotech (Aidenbach, Germany)
HBSS w/o Ca^{2+} and Mg^{2+}	PAN-Biotech (Aidenbach, Germany)
IMDM (21980065)	Thermo Fisher Scientific (Waltham, USA)
Opti-MEM trademark	Gibco (Karlsruhe, Germany)
Penicillin/Streptomycin (Pen/Strep)	PAA (Pasching, Austria)
phosphate-buffered saline (PBS)	PAN-Biotech (Aidenbach, Germany)
recominant murine GM-CSF	Peprotec (Hamburg, Germany)
Trypsin/EDTA	PAN-Biotech (Aidenbach, Germany)
VLE-RPMI 1640	Biochrom (Berlin, Germany)

2.1.2.2 Inhibitors and cell culture reagents

Product	Company (office)
2-DG (CN96.2)	Carl Roth (Karlsruhe, Germany)
3-(4,5-dimethylthiazol-2-yl)-2,5-diphenyltetrauolium bromide (MTT)	Sigma-Aldrich (St. Louis, USA)
Antimycin A (A8674-1G)	Sigma-Aldrich (Taufkirchen, Germany)
Bafilomycin A1	Mechemexpress, (Sollentuna, Sweden)
Brefeldin A (BrefA)	Sigma-Aldrich (Taufkirchen, Germany)
Cycloheximid	Hölzel-Biotech (Köln, Germany)
FCCP (Cay25218-10)	Cayman Chemical (Ann Arbor, USA)
MG-132	Sigma-Aldrich (Taufkirchen, Germany)
Neutral Red	Carl Roth (Karlsruhe, Germany)
Oligomycin	Calbiochem/Merck (Darmstadt, Germany)
Polybrene Infection/Transfection Reagent	Merck (Darmstadt, Germany)
Puromycin dihydrochloride	Sigma-Aldrich (St. Louis, USA)
Rapamycin	Carl Roth (Karlsruhe, Germany)
Rotenone (R8875-1G)/Antimycin	Sigma-Aldrich (Taufkirchen, Germany)
SecinH3	Tocris (Bristol, UK)

2.1.3 Antibodies and dyes

2.1.3.1 Primary antibodies Western Blotting

Target	Species	Clone	Dilution	Company (office)	Order number
AKT	rabbit	-	1:1000	Cell Signaling	9272
AMPK alpha	rabbit	23A3	1:1000	Cell Signaling	2603
CYTH2	mouse	H7	1:500	Santa Cruz Biotechnology	sc-374640
GAPDH	mouse	6C5	1:10000	Acris	ACP001P
Golgin-97 (GOLGA1)	rabbit	D8P2K	1:1000	Cell Signaling	13192
LAMP1	rabbit	-	1:1000	Sigma	L1418
LC3b	rabbit	-	1:1000	Cell Signaling	2775
mTOR	rabbit	7C10	1:1000	Cell Signaling	2983
p62	guinea pig	-	1:1000	Progen	GP62-C
p70S6K	rabbit	-	1:1000	Cell Signaling	9202

Phospho AMPK(T172)	rabbit	40H9	1:1000	Cell Signaling	2535
Phospho p70S6K(T389)	rabbit	-	1:1000	Cell Signaling	9205
Phospho Raptor (S792)	rabbit	-	1:1000	Cell Signaling	2083
Phospho-4E-BP1(T36/47)	rabbit	236B4	1:1000	Cell Signaling	2855
Phospho-AKT(S473)	rabbit	D9E	1:1000	Cell Signaling	4060
Phospho-AKT(T308)	rabbit	-	1:1000	CellSignaling	9275
Phospho-ULK1(S757)	rabbit	-	1:1000	Cell Signaling	6888
ULK1	rabbit	D8H5	1:1000	Cell Signaling	8054
Vinculin	mouse	hVIN-1	1:5000	Sigma	V9131
Wfdc2	rabbit	-	1:1000	Thermo Fisher	PA5-80227

2.1.3.2 Secondary antibodies Western Blotting

Target	Species	Conjugate	Dilution	Company	Article number
Guinea pig IgG (H+L)	Goat	HRP	1:10000	Jackson ImmunoResearch	106-035-003
Mouse IgG	Horse	HRP	1:5000	Cell Signaling	7076
Rabbit IgG	Goat	HRP	1:5000	Cell Signaling	7074

2.1.3.3 Primary antibodies immunofluorescence

Target	Species	Clone	Dilution	Company	Article
Anti-Golgin-97	rabbit	D8P2K	1:100	Cell Signaling	13192
Anti-LAMP2	rat	GL2A7	1:100	abcam	ab13524
Anti-mTOR	rabbit	7C10	1:200	Cell Signaling	2983
Anti-RAB5	rabbit	D95F2	1:100	Cell Signaling	9367
Anti-RAB7	rabbit	C8B1	1:50	Cell Signaling	3547
N-Cadherin	mouse	32/N-Cadherin	1:50	BD / Transduction Laboratories	#610920

2.1.3.4 Secondary antibodies immunofluorescence

Target	Species	Fluorochrome	Dilution	Company	Article number
Mouse IgG (H+L)	Goat	Alexa Fluor 647	1:200	Jackson ImmunoResearch	115-605-166
Rabbit IgG (H+L)	Goat	Alexa Fluor 488	1:200	Life Technologies	A11034
Rat IgG (H+L)	Goat	Alexa Fluor 647	1:200	Thermo Fisher	A21247

2.1.3.5 Lectins

Lectin	Fluorochrome	Company	Article number
Concanavalin A (Con A)	Alexa Fluor 488	Thermo Fisher Scientific (Waltham, USA)	C11252
Peanut Agglutinin (PNA)	Alexa Fluor 488	Thermo Fisher Scientific (Waltham, USA)	L21409
Wheat Germ Agglutinin (WGA)	Alexa Fluor 555	Invitrogen/Life Technologies (Carlsbad, USA)	W32464

2.1.4 Oligonucleotides

2.1.4.1 Genotyping primer

Target	Primer name	Sequence (5'→3')
Cyth2	Pscd2 WT1 screen for	CAGAAATGCCAGGGCTTTCTCAGC
	Pscd2 WT1 screen rev	GCATAGGTTTCAGGGCTGGAAAACAC
	Pscd2 FRT screen rev	CGGAAGGAATGCCCAGCCAAAAT
Cre-recombinase	CRE for	CCGGTCGATGGAGTGA
	CRE rev	GGCCCAAATGTGGATA

2.1.4.2 Sequencing primer

Target/purpose	Primer name	Sequence (5' - 3')
pLentiCRISPRv2 gRNA insertion	hU6-F	GAGGGCCTATTTCCCATGATT
Cyth2 isoform identification	mpscd2 rev qPCR	GAGCTGTCCCTTATTGTTGGGAATC
	Seq m*Cyth2* exon 3 for	CCTTCCTGGCTCTTCCTGTG

Mouse *Cyth2* CRISPR/Cas9-induced mutations	Seq m*Cyth2* exon 3 rev	GCCTGCGAGAAGAGCTAAGT
Human *Cyth2* CRISPR/Cas9-induced mutations	Seq h*Cyth2* exon 2 for	ACACATCCTCTCCCAGCTCT
	Seq h*Cyth2* exon 2 rev	TTCCTGCCCATTGCCATCTT

2.1.4.3 qPCR primer

target	primer name	Sequence (5'→3')
mouse *G6pc1*	mG6pc1 for	AGC TGA ACG TCT GTC TGT CC
	mG6pc1 rev	TTC TCC AAA GTC CAC AGG AG
mouse *Gck*	mGck for	GAA CAA CAT CGT GGG ACT TC
	mGck rev	AGC TCC ACA TTC TGC ATC TC
mouse *Pklr*	mPklr for	CAT TGC TGT GAC TCG TTC TG
	mPklr rev	CAC AAT CAC CAG ATC ACC AA
mouse *Pck1*	mPck1 for	TGC CGG AAG AGG ACT TTG AG
	mPck1 rev	CAC TTG ATG AAC TCC CCA TC

2.1.4.4 sgRNAs

sgRNA library Brie	Mouse *Cyth2*	
sgRNA ID	sgRNA target sequence	Targeted exon
13826	AGCCATTGGGGACTACCTAG	4
13827	TTTGCAGTAAGACCTTGCAG	3 (finally used)
13828	GTTGCATAAGCAGTATCTCT	6
13829	CCTTCACAATCCCAATGTCA	7

sgRNA library Brunello	Human *Cyth2*	
sgRNA ID	sgRNA target sequence	Targeted exon
24354	ACTGCTGCAGAACACACCCG	4
24355	CATGAACCGGGGCATCAACG	7
24356	GCTCAGTGAAGCCATGAGCG	2 (finally used)
24357	GGTGACCGTACCTCTCCCCC	4

2.1.5 Plasmids

Plasmid /Backbone	Description	Gene	Mutation	Marker	E. coli	Addgene no.	Depositing lab
pLentiCRISPRv2	Lentiviral transfer			-	Stbl3	52961	Addgene
pMD2.g	Lentiviral envelope			-	DH5α	12259	Sven Burgdorf
psPAX2	Lentiviral packaging			-	DH5α	12260	Sven Burgdorf
pN1	Overexpression	*Cyth2*-2G	None	RFP (5´Tag)	DH5α		Waldemar Kolanus
pN1	Overexpression	*Cyth2*-2G	E156K	RFP (5´Tag)	DH5α		Waldemar Kolanus
pN1	Overexpression	*Cyth2*-2G	DCC (2-46AS)	RFP (5´Tag)	DH5α		Waldemar Kolanus
pN1	Overexpression	*Cyth2*-3G	None	RFP (5´Tag)	DH5α		Waldemar Kolanus
pN1	Overexpression	*Cyth2*-3G	E156K	RFP (5´Tag)	DH5α		Waldemar Kolanus
pN1	Overexpression	*Cyth2*-3G	DCC (2-46AS)	RFP (5´Tag)	DH5α		Waldemar Kolanus

2.1.6 Software

Software	Company (office)
Imaris 9	Bitplane (Zürich, Schweiz)
Image Studio Lite	LI-COR Biosciences (Lincoln, USA)
R and R studiio	-
Prism 9/10	GraphPad Software (Boston, USA)
Perseus	MPI for Biochemistry (Martinsried, Germany)
Excel	Microsoft Corporation (Redmond, USA)
Wave 2.4.1	Agilent (Santa Clara, USA)
Affinity Designer 2	Serife (Europe) Ltd. (Nottingham, UK)

2.2 Methods

2.2.1 Animal Experimental Techniques

2.2.1.1 Knockout mouse lines

Mice were bred and kept in accordance with the German Animal Welfare Act at the Genetic Resources Center (GRC) of the LIMES Institute, University of Bonn.

Breedings and experimental procedures for the burdened mouse lines were approved by LANUV NRW (Landesamt für Natur, Umwelt und Verbraucherschutz Nordrhein-Westfalen; Aktenzeichen 84-02.04.2015.A496; Aktenzeichen Folgeantrag: 81-02.04.2021.A058) and conducted accordingly. Mice were kept under specific pathogen-free (SPF) conditions, with ad libitum access to water and food and in individually ventilated cages. A 12 h/12 h light-and-dark cycle was maintained as well as a temperature of 22 °C. Genotypes were determined by polymerase-chain reaction (PCR, see 2.2.1.2).

Conditional KO mice were generated by crossing the *Cyth2* KO with a Flp-deleter mouse [159] to remove the β-Galactosidase cassette and transcriptional stop from the *Cyth2* locus, which became active then and was excisable via its loxP sites by Cre recombinase expression.

Mouse line	International nomenclature	Source
Cyth2	B6N-*Cyth2*tm1a(EUCOMM) Wtsi>/Ibcm	European Mouse Mutant Archive (EMMA), Italy
Cyth2$^{fl/fl}$	B6N-*Cyth2*tm1a(EUCOMM) Wtsi>/Ibcm	European Mouse Mutant Archive (EMMA), Italy
alphaMyHC-Cre	B6N-Tg(Myh6-cre)2182Mds	

2.2.1.2 Genotyping of knockout mice

To determine the genotype of KO mice, biopsies (tail tips from newborns or ear punches from adult mice) were taken from the animals and deoxyribonucleic acid (DNA) was isolated by incubation with 200 µl of 50 mM NaOH solution for 20 min at 95 °C. The isolation was stopped by addition of 75 µl Tris/HCl pH 8 followed by centrifugation for 4 min at 4000 rpm and 4 °C to spin down remaining tissue. The samples were stored at 4 °C.

Polymerase chain reaction (PCR) was performed to amplify the genomic loci of interest. The reaction mix was prepared on ice in PCR strips and subjected to the thermocycler protocol as follows. After PCR, the samples were separated by agarose gel electrophoresis (1.2% agarose in 1xTAE buffer) to determine the size of the generated amplicons. Briefly, agarose was dissolved in 1xTAE buffer, ethidium bromide was added and a gel was cast and allowed to polymerize for 15-20 min at RT (room temperature). The digested sample was mixed with 6x loading dye and

the samples were subjected to electrophoresis for 20-45 min at 100 V next to a commercially available DNA ladder. Finally, DNA was visualized with a Gel Max documentation system.

Cyth2 PCR reaction mix	
2 µl	10x DreamTaq buffer
0.4 µl	dNTPs (10 mM)
1 µl	Pscd2 WT1 screen for (10 µM)
1 µl	Pscd2 WT1 screen rev (10 µM)
1 µl	Pscd2 FRT screen rev (10 µM)
0.2 µl	DreamTaq polymerase
2 µl	DNA
12.4 µl	Water

Step	Temp.	Time	
Initial denaturation	95 °C	3 min	
Denaturation	95 °C	45 s	35x
Annealing	64.5 °C	45 s	
Elongation	72 °C	1 min	
	72 °C	5 min	
	4 °C	∞	

Expected band sizes: WT 531 bp, KO 800 bp, floxed allele 687 bp.

Cre PCR reaction mix	
0.5 µl	CRE for (10 µM)
0.5 µl	CRE rev (10 µM)
10 µl	2xONE Taq polymerase
0.8 µl	BSA
1 µl	DNA
7.2 µl	Water

Step	Temp.	Time	
Initial denaturation	94 °C	2 min	
Denaturation	94 °C	30 s	28x
Annealing	58 °C	30 s	
Elongation	68 °C	45 s	
	68 °C	5 min	
	4 °C	∞	

Expected band sizes: Cre recombinase 280 bp

- TAE buffer (1x): 40 mM Tris, 20 mM acetic acid, 1 mM EDTA, pH 8
- 6x Loading Dye: 0.25% bromophenolblue, 0.25% Xylene cyanol FF, 30% glycerol

2.2.1.3 Dissection of organs from newborn mice

Newborn *Cyth2* KO mice were sacrificed about 6 h after birth by decapitation. Bodies and heads were transferred to a PBS-containing petri dish and the dissection was performed using a binocular and sterile instruments. Organs were either snap-frozen in liquid nitrogen or stored in PBS on ice until embedding in cryomedium for native sections. Brains were harvested as one piece, only separating the olfactory bulbs when snap-frozen or separated sagittally for embedding. Skin samples were

taken from the back close to the neck to also get access to the brown adipose tissue (BAT). The thyroid gland was removed and the chest cavity opened to harvest the thymus, lung and heart. After taking the quadriceps femoris as a muscle sample, the abdominal cavity was opened and all inner organs removed. All organs were separated and stored at -80 °C (diaphram, liver, stomach, pancreas, spleen, intestines, kidney, adrenal glands, bladder), apart from the reproductive tract, which was only checked for the sex of the animals. The intestine was split in parts, so that a piece of the duodenum, the jejunum and the colon was taken.

2.2.1.4 Blood glucose measurements and plasma collection from newborn mice

To analyze blood from newborn animals, a commercially available blood glucose meter (Accu-CHEK® Aviva Nano, Roche) was used. Mice were decapitated and the blood glucose measurement strip was held to the open wound immediately. By capillary force a small amount of blood transferred into the measurement strip. Further, the remaining blood was collected with a pipette and transferred to a lithium-heparin-containing microvette before clotting. The microvette was stored on ice until centrifugation at 2000 rpm for 5 min to separate blood cells from plasma. The plasma supernatant was transferred to fresh tubes and stored as 10 µl aliquots at -80 °C to avoid thawing and freezing cycles of the sample.

2.2.1.5 Dissection of hearts from adult mice

In order to analyze cardiac tissue of heart-specific KO mice, adult animals were sacrificed by carbon dioxide (CO_2) inhalation to prevent heavy bleeding in the chest cavity by cervical dislocation. The chest cavity was opened, lungs removed and the heart harvested carefully cutting all connective tissue and vessels. For microscopy, hearts were perfused with cold PBS through the aorta under a binocular avoiding air bubbles. With blood or PBS within all vessels, hearts were put on a tissue and weight “dry” before being put in PBS again.

For cryosectioning, the tissue was stored in cold PBS until embedding in cryomedium as one piece and long-term storage at -80 °C. 10 to 14 µm tissue sections were cut using a cryostat, and sections were mounted on a microscopy

slide to be stored at -80 °C again. For biochemical and molecular biology analysis, heart chambers were separated with scissors and stored in different tubes. The septum was stored with the left ventricle. Tissue samples were snap-frozen in liquid nitrogen and stored at -80 °C.

2.2.1.6 L-Amino acid detection

Plasma amino acids from newborn mice were quantified using the L-Amino Acid Quantification Kit (MAK002, Sigma-Aldrich) according to the manufacturer's instructions. Briefly, for the colorimetric detection in a 96-well format the standard and all samples were filled into individual wells and filled up to 50 µl volume with L-Amino Acid Assay Buffer. Per sample, 3 µl plasma were used without any pre-processing. The reaction mix was prepared (46 µl L-Amino Acid Assay Buffer, 2 µl L-Amino Acid Probe and 2 µl L-Amino Acid Enzyme Mix per well) and added to the samples and standard. Samples were mixed briefly on a horizontal shaker, protected from light and incubated for 30 min at 37 °C. Finally, absorbance was measured with a plate reader (infinite M200, Tecan) at 570 nm, a standard curve was generated and the plasma amino acid concentration calculated for each sample.

2.2.2 Cell culture and *in vitro* assays

2.2.2.1 Cell culture of cell lines

C2 myoblasts (murine, muscle fiber precursor cells) were cultured in DMEM-based (P04-03550) medium supplemented with 15% fetal calf serum (FCS), 1% penicillin-streptomycin (Pen/Strep), 1% non-essential amino acids and 2% sodium pyruvate at 37 °C within a 5% CO_2 atmosphere. Passages were performed every 48 h, as this strict schedule ensured reproducible results. For splitting or seeding, the cells were washed with PBS once after medium removal. Cells were detached from the culture plates by incubation with trypsin/EDTA for 8-10 min at 37 °C, resuspended and cell numbers were determined with a Neubauer counting chamber. 10^5 cells per 6 cm cell culture plate were centrifuged at 280 g for

5 min at RT to get rid of the trypsin-containing medium and seeded in a total volume of 4 ml fresh medium [160, 161].

A7r5 (rat, smooth muscle cells) cells were kept at 37 °C with 5% CO_2 in low glucose DMEM without phenol red (P04-01159). Supplements to the medium were 10% FCS, 1% Pen/Strep and 1% L-glutamine and the cells were split every three to four days. To do so, cells were detached using trypsin/EDTA for 10 min at 37 °C, counted and centrifuged at 1800 g for 5 min. Cells were seeded at 10^5 cells per 6 cm cell culture dish in 4 ml fresh medium [162].

HEK293T (human, embryonic kidney; clone 293T) cells were cultured in DMEM (P04-03550) containing 10% FCS and 1% Pen/Strep at 37 °C with 5% CO_2 and split every two to three days simply at a 1:8-1:10 ratio in 10 ml medium per 10 cm cell culture dish. HEK cells were detached flushing the dishes and re-suspended to get a single-cell solution.

MuTu DC1940 (murine, dendritic cells) cells were cultured and kindly provided by Nicole Dörffer, previously gifted to the laboratory by Hans Acha-Orbea [163]. Briefly, the semi-adherent cells were subcultured at 70-80% confluency, while collecting the supernatant and incubating the remaining adherent cells with 2 mM EDTA for 2-5 min at 37 °C. All cells were centrifuged for 5 min at 300 g, the supernatant was removed and the cells resuspended in fresh medium (IMDM, supplemented with 10% FCS, 100 µg/ml Pen/Strep, 50 µM 2-Mercaptoethanol), seeded at $2x10^6$ cells per 10 cm cell culture dish and cultured for three to four days at 37 °C and 5% atmospheric CO_2. For experiments presented in this thesis, only inactivate MuTu cells were used.

2.2.2.2 Generation and culture of murine embryonic fibroblasts (MEFs)

Beside immortalized cell lines, MEFs are a widely used cell biological tool for *in vitro* assays. As an additional cell type analyzed in certain aspects of this work, MEFs were isolated from the *Cyth2* KO mouse line following the instructions of [164]. To do so, plug matings of heterozygous *Cyth2* KO mice were performed and on day E13.5 embryos were dissected in PBS. Heads were utilized for DNA isolation and subsequent genotyping as described above (2.2.1.2; using 400 µl 50 mM NaOH and

150 µl Tris/HCl pH 8), while all internal organs were removed and the remaining tissue was transferred to a new dish with fresh PBS.

The following steps were performed under sterile cell culture conditions, where the embryos were rinsed with fresh PBS. The embryos were transferred to a fresh dish containing 3 ml trypsin/EDTA and dissociated by pipetting 2-4 times. Another 2 ml trypsin/EDTA were added and carefully mixed with a pipette, followed by incubation for 5-10 min at 37 °C. Embryos were dissociated again followed by another incubation step, at which end the sample was transferred to a 50 ml tube. The volume was doubled by addition of MEF medium with Pen/Strep and sample were left to allow larger tissue pieces to settle to the bottom of the tube. The cell suspension was transferred to a fresh tube avoiding the larger pieces and spun for 5 min at 1000 g and RT. The supernatant was removed, the MEFs of one embryo resuspended and plated in 10 ml MEF medium (with Pen/Strep) on a 10 cm tissue culture dish. MEFs were cultured at 37 °C with 5% atmospheric CO_2.

MEFs were passaged at confluency after 2-3 days. Briefly, medium was removed and cells washed with HBSS (without Ca^{2+} or Mg^{2+}). HBSS was discarded, trypsin/EDTA added and cells incubated for 3-5 min at 37 °C. When all cells were detached, the reaction was stopped adding the same volume of MEF medium without Pen/Strep. MEFs where collected, counted and centrifuged at 1000 g and RT for 5 min. Pellets were resuspended in fresh MEF medium without Pen/Strep and seeded at 10^6 cells per 10 cm dish or adjusted densities for experimental purposes in 6-wells or on coverslips.

2.2.2.3 *In vitro* inhibitor assays

For inhibition of protein degradation, ARF GTPase signaling or the mTOR pathway by the respective inhibitors, cells were seeded two days before the experiment at a density as if under culturing conditions (to reach confluency on the day of the experiment or harvesting) in 6- or 12-well tissue culture plates (alternatively on coverslips for microscopy). To guarantee equal inhibitor concentrations, pre-conditioned medium was partially recovered from the wells, leaving the same volume per well. Recovered medium was pooled and used to prepare inhibitor and control working solutions. Equal amounts of working solution

were added to the wells, ensuring that culture conditions were only altered by the solvents and inhibitors used.

Final inhibitor concentrations, solvent controls and incubation times are listed below. After the respective incubation time, medium was removed, cells washed carefully with cold PBS and scraped off the plates to be collected in 1.5 ml reaction tubes. The cells were centrifuged twice at full speed and 4 °C to remove most of the PBS from the tube. Cell pellets were snap-frozen in liquid nitrogen and stored at -80 °C or processed immediately. Cells on coverslips were fixed for 20 min in 4% paraformaldehyde/PBS (PFA/PBS) solution and washed with PBS afterwards.

Inhibitor	Final concentration	Solvent (and ctrl treatment)	Incubation time (if not stated otherwise)
MG-132	10 µM	DMSO	1 h
SecinH3	50 µM	DMSO	4 h
Brefeldin A	5 µg/ml	ethanol	4 h
Cycloheximid	50 µM	Water (cell culture grade)	1 h
Bafilomycin A1	1 µM	DMSO	1 h
Rapamycin	1 µM	DMSO	1 h

All inhibitors were stored according to the manufacturer's instructions in aliquots to prevent repeated freezing and thawing. Of note, SecinH3 tends to precipitate at the concentrations used in this thesis due to its hydrophobicity. The final concentration of its solvent DMSO was 0.4% to keep as much SecinH3 in solution as possible. Cell viability was assessed microscopically and was not affeced. Experimentally, SecinH3 was diluted in the maximal volume of DMSO before medium was added carefully to the solution.

2.2.2.4 *In vitro* starvation and feeding experiments

Similar to the inhibitor assay, feeding experiments were performed two days after seeding the cells, when they almost reached confluency. Of note, starvation experiments were performed at larger scales (6 cm or 10 cm dishes instead of 6- and 12-well plates), as starved cells had dramatically reduced protein amounts. Complete deprivation of nutrients, hereafter simply called starvation, was performed

by incubation of cells in starvation medium (HBSS supplemented with 1% full culture medium). Before the incubation, cells were washed with starvation medium once to remove remaining full medium.

All re-feeding experiments included 1-2 h pre-conditioning of cells in starvation medium, before the respective feeding condition was applied. To test the effect of a specific nutrient component (e.g., amino acids), dialyzed FCS was used, which only contains residual amounts of smaller molecules such as glucose or amino acids and therefore is primarily a source of proteins and growth factors. The starvation and re-feeding media were prepared in the laboratory based on the composition of DMEM medium used in standard culture conditions.

2.2.2.5 Lectin staining and flow cytometry

To analyze glycosylation of surface proteins C2 myoblasts were stained with fluorophore-coupled lectins, which bind glycoside structures on surface molecules of cells comparable to antibodies in a very specific and high-affinity manner. Thereby, surface expression of certain glycoside moieties were measurable by flow cytometry. These stainings and measurements were performed by Dr. Bettina Jux. In brief, C2 myoblasts were harvested with 2 mM EDTA in PBS. Cells were stained with Alexa Flour 488 conjugated Lectins (Thermo Fisher: Con A-Alexa488 conjugate C11252; PNA-Alexa488 conjugate L21409, WGA-Alexa555 conjugate W32464) according to the manufacturer's instrucations and measured with a FACS Canto II. Analysis was done with FlowJo™ (v.10).

2.2.2.6 Neutral Red assay

Neutral Red assays were performed to measure cell densities and thereby determine proliferation rates of C2 myoblasts. About 90 min after seeding, or at the end of the growth period, 40 µg/ml Neutral Red were added to the cells in medium containing only 1% FCS. Cells were incubated for 60 min at 37 °C with 5% atmospheric CO_2, followed by a washing step with PBS at RT. Cells were destained with 1% acetic acid in 50% ethanol and 49% ddH_2O. Samples were shaken for 10 min in a linear fashion at the Tecan plate reader, followed by

fluorescence measurements with excitation at 530 nm and emission detection at 645 nm wavelength (mean of 25 flashes per well). A standard curve with increasing cell numbers was measured to calculate the cell numbers at the seeding time points as well as at the end of the growth period.

2.2.2.7 Plasmid transfection for rescue experiments in C2 myoblasts

To gain mechanistic insight in the regulation of endosomes and the Golgi apparatus by CYTH2, rescue and overexpression experiments were performed in C2 myoblasts, WT and KO clones. The cells were seeded on cover slips. After adhering, they were transfected with the appropriate plasmids (2.1.5, 3.5.3) using jetOPTIMUS® (Polyplus transfection®) according to the manufacturer's instructions. After 48 hours cells were fixed with 4% PFA/PBS and stained for analysis of endosomes and the Golgi apparatus. Dr. Bettina Jux performed most of the transfections.

2.2.2.8 Sea Horse Assay

In order to access the global metabolic properties of *Cyth2*-deficient cells, C2 myoblasts were subjected to glycolytic and mitochondrion stress test in SeaHorse assays. The day before the experiment, calibration medium and the cartridge with 200 µl ddH_2O per well put in the utility plate were incubated at 37 °C but otherwise atmospheric conditions overnight. $4x10^3$ C2 myoblasts per well were seeded onto the Agilent Plate and incubated under standard culture condition. On the experimentation day, water in the cartridge was exchanged with calibration medium and the cartridge was filled with the injections (see table below). Cell culture medium was removed from the Agilent Plate and 180 µl SeaHorse medium added to each well. The cells were incubated at 37 °C under atmospheric conditions until the assay started. The meanwhile prewarmed (37 °C) SeaHorse analyzer was set up, the cartridge and the Agilent Plate with the cells inserted. Preparation of the assay consumables was done by Laura Schlautmann, AG Burgdorf.

The software protocol ran on Wave 2.4.1, all data were exported to Excel files and all medium was removed from the Agilent Plate, which was then stored at -20 °C

until cell count determination using CyQUANT™ for normalization of all data. The CyQUANT™ NF Cell Quantification mix was prepared (50 µl/96-well; 20% of 5xHBSS, 80% ddH2O, 1:500 Component A), added to the wells of interest and incubated for 30 min at 37 °C. Fluorescence measurements were performed using a plate reader with 485 nm excitation wavelength and 530 nm of emission wavelength. Data were analyzed using Excel following the instructions of the Mito-stress test and Glycolytic Stress test user guides.

Slot	Volume	Mito-Stress test stimuli	final concentration
A	20 µl	Oligomycin	1 µM
B	22 µl	FCCP	4 µM
C	25 µl	Rotenon/Antimycin	0.5 µM
D	27 µl	2-DG	0.5 µM

2.2.3 Microscopy

2.2.3.1 Immunofluorescence staining of cells

In order to visualize proteins within cells and cellular structures, immunofluorescence stainings were performed. Cells were seeded onto coverslips and cultured on them for one to two days under standard culture conditions. For HEK293T cells, MuTu cells and MEFs, coverslips were coated with fibronectin for 1 h at RT in PBS at 50 µg/ml before, washed with PBS and either stored at 4 °C in PBS or used immediately. Cells were washed with PBS, fixed with 4% PFA/PBS for 20 min at RT, and washed with PBS again. Afterwards, coverslips were stored in PBS at 4 °C for a couple of days or stained immediately.

The cells were permeabilized and blocked in 2% BSA/0.2% TritonX100/PBS for 30 min at RT in wells followed by primary antibody staining in 1% BSA/0.1% TritonX100/PBS for 1 h at RT in a humidified chamber. Coverslips were washed three times in cold PBS for 5 min each, followed by secondary antibody staining in 0.05% TritonX100/PBS for 45 min at RT and another three washing steps. Finally, the coverslips were dipped into desalted water and mounted with Fluoroshield™ containing 1 ng/µl DAPI onto glass microscopy slides. Before each incubation step, coverslips were put up against a plate to allow all remaining fluid to be soaked up in a tissue, to prevent any dilution of the following staining solution. Coverslips were sealed after the Fluoroshield™ was dry with nail polish.

2.2.3.2 Confocal Microscopy of tissue and cells

Cells were imaged using an inverted, confocal laser scanning microscope (LSM880 with Airyscan) with 63x magnification. Cells were imaged as z-stacks (0.1 µm steps) covering the whole cell volume. Laser configuration and intensity settings were re-used in all experiments of an experimental set to increase comparability. For each experimental condition, two to three z-stacks were taken. Analysis of subcellular structures and cell size was performed with Imaris 9.

2.2.4 Analysis of microscopic stacks with IMARIS 9

2.2.4.1 Cell detection

Cells were detected with the Imaris 9 cell detection algorithm as cell bodies with a single nucleus. Nuclei were detected as spots based on the DAPI signal with an estimated diameter of 8 µm. Intensity thresholds were manually adjusted to catch every nucleus of completely imaged cells as one object. Cell bodies were detected optimally based on the fluorescence of a surface marker protein or the rather unspecific fluorescence of intracellular structures stained. Manual thresholding ensured the detection of complete cell bodies. The automated detection of cells allowed only a single nucleus per cell and separated cells by fluorescence intensity due to lower intensity at cell borders. Finally, incomplete cells at the image borders or obviously false detections were omitted and parameters of the remaining cells exported for further analysis.

2.2.4.2 Golgi detection

The surface detection algorithm was used to identify Golgi structures with a default surface grain size of 0.141 µm and elimination of background fluorescence with a default diameter of 0.529 µm for the largest sphere to be able to fit into any detected structure. The intensity threshold was set manually, as Golgi intensities varied between experiments as well as images within experiments. Detected surface structures smaller than 400 volumen pixel (“voxel”) were excluded automatically. Remaining surfaces were grouped as a single Golgi stack, discarding those which were not entirely captured during the imaging process, not clearly separable from a neighboring cell’s Golgi stack or obviously dispersed or divided due to cell division

processes or dying cells. Surface parameters for identified Golgi stacks, such as volume and ellipticity (Fig. 2.1), were exported and further analyzed.

A

a	b	c	ep	eo	Shape
1	1	1	0.00	0.00	Sphere
1	1	3	0.89	0.16	prolate Spheroid
1	3	3	0.09	0.89	oblate Spheroid
3	3	3	0.00	0.00	Sphere

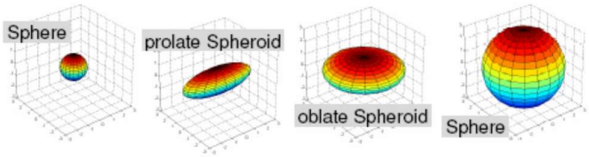

Figure 2.1: Description of spheroids
Spheres are physically preferable in terms of surface tension, however, many compartments within the cell are not perfectly round. Ellipticity describes spheroids as either prolate, when a spheric object is extended in one spatial dimension, leading to an elongated shape. Spheric objects extended in two dimensions are more disc-shaped and described as oblate. Imaris 9 Reference Manual.

2.2.4.3 Analysis of RAB5-, RAB7 and LAMP2-positive spots

To analyze endosomal (RAB5, RAB7) and lysosomal (Lysosome-associdated membrane protein 2; LAMP2) structures, the Imaris 9 spot detection algorithm was used. Default settings were applied apart from the estimated size, which was set to 0.5 µm in diameter. The detection intensity threshold was set to automatic thresholding to ensure an unbiased analysis of spots. This way, each picture was analyzed individually without bias by the experimenter, but still taking intensity variations due to staining variances into account. Spots detected in areas which were outside a cell were removed manually. Spots within cells were matched with that cell to be able to calculate the spot/cell volume ratio for each individual cell. Spot parameters were exported and further analyzed.

2.2.4.4 Co-localization of LAMP2 and mTOR

Co-staining of two or more proteins is used to show potential protein-protein interactions, recruitment of proteins to specific sites of a cell or distinction of organelles. Co-localization of LAMP2 and mTOR was tested in C2 myoblasts by co-staining of both proteins as described above (2.2.3.1). Z-stacks were imaged and overlapping fluorescence intensities of the two proteins analyzed with the co-loc algorithm of Imaris 9. Pearson's correlation of intensities was taken as a measure for protein co-localization.

2.2.5 Protein biochemistry

2.2.5.1 Protein isolation

To analyze protein expression levels via Western Blot, tissue samples and cells were lyzed in MRC buffer (see composition below; protease inhibitors were added immediately before lysis), which inhibits phosphatase activity to preserve the phosphorylation status of proteins of interest. Tissue samples were smashed in cold buffer and on ice with a small pestle, cells were forcefully resuspended. Lysis took place on ice with a short vortex every five minutes for 20 min in total, followed by centrifugation at 13.200 g for 5 min at 4 °C to precipitate remaining cell fragments and DNA.

MRC lysis buffer (final conc.)	
50 mM	Tris/HCl
1 mM	EGTA
1 mM	EDTA
10 mM	β-glycerol phosphate
50 mM	Sodium fluoride
5 mM	Sodium phosphate
1 mM	Sodium vanadate
270 mM	Sucrose
1%	TritonX100

Protease inhibitors (final conc.)	
1 mM	Benzamidine
2 µg/ml	Antipain
10 µg/ml	Leupeptin
10 µg/ml	Aprotinin
1:1000	PMSF(from saturated stock)

2.2.5.2 Determination of Protein concentrations

Protein concentrations of supernatants from lysed samples were determined by BCA assay (bicinchoninic acid assay; Pierce™ BCA Protein Assay Kits) following the manufacturer's instructions in a 96-well format and using a BSA standard. Briefly, 3 µl lysate or protein standard solution were pipetted into a 96-well, 200 ml BCA solution (reagents A:B mixed at a 50:1 ratio) were added and the samples incubated for 10 min at 65 °C. Afterwards, absorbance was measured with a plate reader (infinite M200) at 562 nm. A standard curve was fitted and the protein concentrations for each sample calculated.

2.2.5.3 SDS-PAGE, Western Blotting

To determine the expression of specific proteins, protein lysates were subjected to SDS-PAGE (using the MiniTrans-Blot Cell system) to be separated by molecular weight. Separated proteins were transferred by wet blotting onto nitrocellulose membranes to be detected using specific antibodies.

Equal amounts of protein per sample were prepared in fresh tubes and mixed with 5x sample buffer (see composition below), boiled for 5 min at 95 °C and filled onto a self-made SDS-polyacrylamide gel. Gels were prepared in advance, pouring resolving gels (8-15%) depending on the molecular weight of the proteins of interest first, and filling a stacking gel with only 5% acrylamide on top. Electrophoresis was performed at 80 V first, increasing the voltage to 120 V whence the leading front moved into the separating gel. The leading front was allowed to run out of the gel, then electrophoresis was stopped and wet blotting was performed to transfer the proteins from the gel onto a nitrocellulose membrane at 80 V and 4 °C for 2 h (for the composition of the transfer buffer see below).

Transfer efficiency was assessed by Ponceau staining of the membrane (0.1% Ponceau S in 5% acetic acid) and membranes were scanned to use the unspecific protein stain as a loading control and normalization reference. Ponceau was removed with tris-buffered saline with Tween (TBST; see composition below) and nitrocellulose membranes were blocked with 5% non-fatty milk powder in TBST for 1 h at RT. Primary antibodies were incubated according to 2.1.3.1 at 4 °C rotating in falcon tubes overnight. Membranes were washed three times with TBST for five minutes and subjected to horse reddish peroxidase (HRP)-coupled secondary antibodies for 1 h at RT as denoted in the 2.1.3.2. Secondary antibodies were washed away with TBST three times for 5 min each and membranes were incubated with enhanced chemiluminescence (ECL) substrate solutions for 1-2 min at RT followed by developing with standard, light-sensitive radiographic films in a dark chamber. Films were developed, fixed and washed with water, dried and scanned.

Membranes were used multiple times and regenerated by intense washing with TBST. Stripping procedures were avoided. Instead, detection of proteins with specific antibodies was planned in a way, that weak protein signals were detected first and strong signals last (e.g., housekeeping proteins). Additionally, host species

of primary antibodies were altered as much as possible (switching from mouse to rabbit and back) and detected proteins did not have similar molecular weights. Phospho-proteins and their respective total protein control were detected on separate membranes, processing samples and membranes simultaneously.

- 5x samples buffer: 100 mM Tris/HCl (pH 6.8), 4% SDS, 1% bromophenol blue, 25% glycerin, 200 mM DTT
- Laemmli Running Buffer: 25 mM Tris, 250 mM glycine, 0.1% SDS
- Transfer buffer: 20% methanol in 200 mM glycine, 25 mM Tris
- TBST: 0.05 M Tris, 140 mM sodium chloride, 0.05% Tween20, pH7.9

2.2.5.4 Semi-quantitative analysis of protein expression

Chemiluminescence-based detection of proteins with HRP-coupled antibodies is considered semi-quantitative, because there is no linear correlation between protein amounts and signal intensity. Semi-quantitative analysis of scanned radiographic films was performed using the Image Studio Lite software. Specific protein bands were marked as a region of interest (ROI) and pixel intensities detected compared to a subtracted background in close proximity to the specific bands. The same way, Ponceau intensities were measured in an area around the proteins of interest or over the complete membrane. Ponceau intensities were used to normalize the measurements of protein intensities, calculating the ratio between protein signal and Ponceau signal.

2.2.6 Molecular biology

2.2.6.1 Isolation of RNA from tissue samples and cells

To analyze the transcriptional activity of specific genes, RNA was isolated from tissue and cell samples using TRIzol™ reagent. Small pieces of tissue were homogenized in 1000 µl TRIzol in a Precellys 24 homogenisator with 0.4 g of small glass beads for 2 min. As this process produces some heat, samples were stored on ice afterwards to adjust to RT again. After 5 min incubation, 200 µl chloroform were added and the samples vortexed for 15 s. After 2-3 min incubation, samples were centrifuged for 15 min at full speed and RT. The resulting upper, aqueous

phase was recovered and transferred to a fresh tube. 500 µl isopropanol were added and the samples mixed by inverting the tubes. Samples were left for 10 min at RT, followed by centrifugation for 10 min at 14000 rpm at RT. The supernatant was discarded and the pelleted RNA washed twice with 1 ml 75% ethanol, spinning in between at 14000 rpm and 4 °C for 5 min. After removing the ethanol thoroughly, samples were dried at RT for 5-10 min and the RNA solved in nuclease-free water (10 µl at least; incubation at 55 °C improves this process). RNA isolation of smaller tissue samples or cell pellets was performed using half the volumes of all reagents. Exceptionally low amounts of RNA were isolated adding 2 µg linear polyacrylamide (LPA) per sample to the TRIzol™ reagent and RNA precipitation in isopropanol at -20 °C overnight.

Concentrations of dissolved RNA were determined with a spectrophotometer (NanoDrop 2000), RNA was stored at -20 °C until further processing.

2.2.6.2 cDNA synthesis

Before gene expression analysis using quantitative PCR, isolated RNA needs to be transcribed into complementary DNA (cDNA). To do so, 1 µg of RNA was incubated with 1 µl DNAse 1 (1 U; in 1 µl DNAse 1 buffer and nuclease-free water; total volume of 10 µl) in PCR strips for 15 min at 37 °C to remove DNA contaminations from the sample. Addition of 1 µl EDTA and incubation for 10 min at 75 °C stopped the DNAse digest. For the cDNA synthesis, the High Capacity cDNA Reverse Transcription Kit was used. The MultiScribe™ Reverse Transcriptase was prepared in a master mix (according to the manufacturer's instructions) and added to each sample, followed by incubation at 25 °C for 10 min, reverse transcription at 37 °C for 120 min and enzyme deactivation for 5 min at 85 °C. cDNA samples were kept at 4 °C afterwards or stored at -20 °C until further use.

2.2.6.3 qPCR

To analyze gene expression on the mRNA level, qPCRs were performed on the cDNA generated from isolated RNA samples. The iTaq™ Universal SYBR® Green Supermix and custom-designed primers (2.1.4.3) spanning exon-exon junctions

were used. In brief, for each sample primer pairs for the respective target genes (0.75 µl per sample and primer), 7.5 µl iTaq™ Universal SYBR® Green Supermix and 5 µl water were prepared as a master mix and pipetted into wells of the qPCR plates. 1 µl sample cDNA was added, water served as control, and the plate was subjected to PCR cycling with the CFX 96 PCR cycler. Analysis was performed using Excel and the delta-cc method [165].

2.2.6.4 *Cyth2* transcript sequencing for isoform expression analysis

Cyth2 is expressed in two isoforms in different tissues and cell types. These two isoforms are only distinguished by a small exon encoding for a single glycine, and therefore called 2G- or 3G-isoforms. Isolation of RNA, cDNA synthesis (2.2.6.1, 2.2.6.2) and subsequent sequencing of the PCR-amplified *Cyth2* transcript were used to analyze the relative expression levels of each isoform.

PCR to amplify full length *Cyth2* transcripts was performed using the reaction mix and thermocycler settings below. PCR products were separated on a 1% agarose gel (see 2.1.4.1), the respective bands at 1200 bp were isolated using the NucleoSpin Gel&PCR Clean-up kit and send for Sanger Sequencing (GATC, Eurofins). The sequence data were analyzed using the Tide-tool for genome editing (Brinkman, 2014).

Phusion PCR	
4 µl	5x Phusion™ HF Buffer
0.4 µl	DNTPs (10 mM)
1 µl	for (10 µM)
1 µl	rev (10 µM)
0.6 µl	DMSO
0.2 µl	Phusion™ High-Fidelity DNA Pol.
1 µl	DNA
11.8 µl	Water

Step	Temp.	Time	
Initial denaturation	98 °C	30 s	
Denaturation	98 °C	5-10 s	35x
Annealing			
Elongation	72 °C	1 min	
	72 °C	5 min	
	4 °C	∞	

2.2.7 Generation of knockout cells using CRISPR/Cas9

2.2.7.1 Generation of *Cyth2* KO cells using CRISPR/Cas9

Using the Clustered Regularly interspace Short Palindromic Repeats/ CRISPR-associated protein-9 (CRISPR/Cas9) system, KO organisms can be generated. The

unspecific Cas9 endonuclease binds a small scaffold single guide RNA (sgRNA), which further extends from the complex and guides the Cas9 enzyme with a 20-base pair target sequence to a specific site in the genome. Endonuclease-triggered DNA repair mechanisms can introduce small insertions and deletions, which might cause frameshift mutations in the respective target gene.

In this thesis, the CRISPR/Cas9 system combined with lentiviral transduction was used to generate *Cyth2* KO cell lines based on the protocol from [166]. First, sgRNAs target sequences were taken from the Human and Mouse CRISPR KO Pooled Library (Brunello and Brie library, respectively; [167]) for gene editing and designed as primer pairs with a 5'CACCG- overhang at the forward sequences and 5'AAAC- and 3'C- overhangs to the reverse sequence of the sgRNAs. The 3' end contained the protospacer adjacent motif (PAM) sequence as designed for the library. All four sgRNAs for *Cyth2* from both the human and mouse library were tested and processed in parallel.

The sgRNA-primers were phosphorylated for 30 min at 37 °C, followed by enzyme inactivation and denaturation at 95 °C for 5 min. Samples were cooled down to 25 °C with a temperature decrease of 5 °C per min. For the reaction mix compare table below.

sgRNA oligonucleotides were cloned into the pLentiCRISPRv2 vector (Transfer plasmid, #52961), which contains two expression cassettes for hSpCas9 and the chimeric guide RNA expression, as well as a puromycin resistance for cell selection. Cloning was performed using BsmBI restriction and Golden Gate assembly, which enabled backbone digestion and insert ligation within a single reaction. Phosphorylated and annealed oligonucleotides were diluted 1:10 and used for the reaction described in the table below. Reactions were performed in 15 cycles of 37 °C for 5 min followed by 20 °C incubation for another 5 min.

Oligo annealing mix	
1 µl	Oligo 1 (Stock 100 µM)
1 µl	Oligo 2 (Stock 100 µM)
1 µl	10x T4 Ligation Buffer (NEB)
6.5 µl	ddH2O
0.5 µl	T4 PNK (NEB)

Step	Temp.	Time
Oligo phosphorylation	37 °C	30 min
Denaturation	95 °C	5 min
Annealing	Ramp down	5 °C/min
	4 °C	

Golden Gate Assembly mix		Step	Temp.	Time	
2.5 µl	10x T4 Ligase BufferBsmBI-v2	Digestion	37 °C	5 min	
1 µl	BsmBI-v2	Ligation	20 °C	5 min	15x
0.25 µl	DTT (Stock 100 mM)		4 °C	∞	
0.125 µl	BSA (Stock 20 mg/ml)				
0.125 µl	T4 Ligase				
1 µl	Diluted oligo duplex				
1 µl	Plasmid backbone (25 ng/µl)				
19 µl	Ultrapure water				

2.2.7.2 Heat shock transformation of E. coli

To amplify ligated pLentiCRISPRv2 plasmids, 2 µl of the ligation mix were used to transform Stbl3 E. coli bacteria. 50 µl chemo-competent bacteria suspension were mixed gently with the ligation mix on ice, transferred to a water bath and incubated for 45 seconds at 42 °C (heat shock). Transformed bacteria were immediately cooled down on ice, 300 µl lysogeny broth (LB) medium were added and E. coli were incubated for 1 h at 37 °C while shaking to recover. Finally, about 80% of transformed bacteria were seeded onto agar plates containing selection antibiotics (100 µg/ml ampicillin). After overnight incubation at 37 °C, a single clone from each plate was picked and expanded over 16 h in 4 ml LB medium (containing 100 µg/ml ampicillin) at 37 °C and shaking with 280 rpm.

2.2.7.3 Plasmid preparation

In order to verify the correct insertion of sgRNAs into the pLentiCRISPRv2 vector, plasmids were isolated from the bacteria overnight cultures. 3-4 ml of bacterial suspension were pelleted by centrifugation at 1000 g at RT for 2 min. The pellet was taken up in 200 µl of Solution I (for composition, see below) containing 0.1 µg/ml RNase A. Lysis of bacteria started with addition of 400 µl Solution II and careful inverting of the tubes. After 3-5 min 300 µl Solution III were added to stop lysis and the samples were centrifuged for 10 min at 13000 rpm and 4 °C to remove cell debris. The supernatant was transferred to a new tube and 300 µl phenol-chloroform (1:1 mixture, lower phase) were added. The samples were briefly vortexed and centrifuged for 5 min at 13000 rpm and 4 °C. The upper, aqueous phase was

recovered and plasmid DNA was precipitated in a fresh tube by addition of 800 µl isopropanol. Plasmid DNA was pelleted by centrifugation at full speed for 5 min and at 4 °C and washed twice with 70% ethanol and spinning for 1 min at 13000 rpm and 4 °C. After careful removal of the supernatant, pellets were allowed to air-dry for a few minutes, before being dissolved in 50-80 µl nuclease-free water. Plasmid concentrations were measured with a spectrophotometer (NanoDrop 2000) and the DNA was stored at -20 °C.

Isolated plasmids were digested with restriction enzymes and the resulting fragments separated by agarose gel electrophoresis to determine the quality of the isolation and verify, whether a correct clone was picked. If the digested plasmids showed the expected band sizes, intact plasmid DNA was sent for Sanger Sequencing (GATC, Eurofins) to verify correct insertion of sgRNAs.

- Solution I: 10 mM EDTA, 25 mM Tris, 50 mM glucose, pH 8
- Solution II: 0.2 M sodium hydroxide, 1 % SDS (w/v), pH 13
- Solution III: 3 M potassium acetate, 2 M acetic acid, pH 5

2.2.7.4 Lentivirus production

To generate lentiviral particles for target cell transduction, HEK293T cells were seeded the day before to reach 60-70% confluence on the day of transfection. Per 10 cm dish HEK cells were co-transfected with 3 µg psPAX2 packaging plasmid (#12260), 1.5 µg pMD2.G envelop plasmid (#12259) and 6 µg plentiCRISPRv2 for the respective sgRNA using the calcium phosphate transfection method. The plasmids were mixed in 0.3 ml 0.25 M calcium chloride and the mix was added dropwise, while shaking on a vortex, to 0.3 ml 2xHBS transfection buffer. After 15 min incubation at RT, the transfection mixture was added to the HEK cells and incubated for 6-8 h at 37 °C. The medium was exchanged and the cells were incubated another 48 h for virus production.

The virus-containing supernatant was collected and sterile-filtered (0.45 µm pores). 8 µg/ml polybrene were added and the virus supernatant was stored at -20 °C. To test for sufficient transfection of HEK cells, a GFP-plasmid transfection was performed in parallel.

- 2xHBS transfection buffer: 42 mM HEPES, pH7.5, 274 mM NaCl, 10 mM KCl, 1.4mM Na_2HPO_4, 15 mM D-glucose

2.2.7.5 Target cell transduction

For lentiviral transduction C2 myoblasts, A7r5, HEK293T, and MuTu cells were seeded in 6-well plates. The day after, 1 ml of virus-containing and polybrene-supplemented supernatant were added to the wells, the plates were sealed with parafilm and centrifuged for 60 min at 761 g at RT. After 24 h incubation under culture conditions the virus supernatant was replaced with fresh medium. Cells were incubated for another 24 h under culture conditions, then the selection with puromycin was started. The optimal puromycin concentration for each cell line was determined prior using the MTT assay (see 2.2.7.7). As a control for the selection process, the vitality of non-transduced cells was observed.

2.2.7.6 Subcloning of transduced cells

After antibiotics selection, cells were expanded and first batches were frozen for long-term storage. KO efficiency of the different sgRNAs was tested by Western Blot for CYTH2 of transduced batches. Cells with an obvious decrease in CYTH2 protein expression were subcloned to generate single-cell lineages. Unfortunately, this was not possible for A7r5 cells because no cell survived the single-cell culture. Expanded clones were tested again for CYTH2 protein expression by Western Blot. DNA extraction was performed for promising clones and Sanger Sequencing confirmed the targeted KO of *Cyth2*. Wildtype clones were part of the transduction process and simply unaffected due to silent mutations. In contrast, wildtype batches (A7r5 cells) were never transduced.

2.2.7.7 MTT assay

In order to determine an optimal puromycin concentration for cell selection after lentiviral transduction, an MTT viability assay was performed [168]. C2 myoblasts were seeded in technical triplicates in a 96-well plate and cultured overnight. The next day, puromycin treatment was started with increasing concentrations (0-4

µg/ml) of puromycin. Untreated cells were used as a control, cell-free but medium-containing wells were used for background subtraction.

After 72 h treatment, cell viability was accessed by addition of 3-(4,5-dimethylthiazol-2-yl)-2,5-diphenyltetrauolium bromide (MTT) with 0.1 mg MTT per well. During incubation at 37 °C for 4-5 h, cells were allowed to metabolize the MTT, resulting in microscopically visible crystals. 200 µl stopping solution (2% HCl/isopropanol) were added. Protected from light and gently shaking, cells were incubated at RT overnight to resolve the crystals. Finally, the absorbance per well was measured with a plate reader (infinite M200) at 570 nm.

2.2.8 Differential centrifugation and mass spectrometry

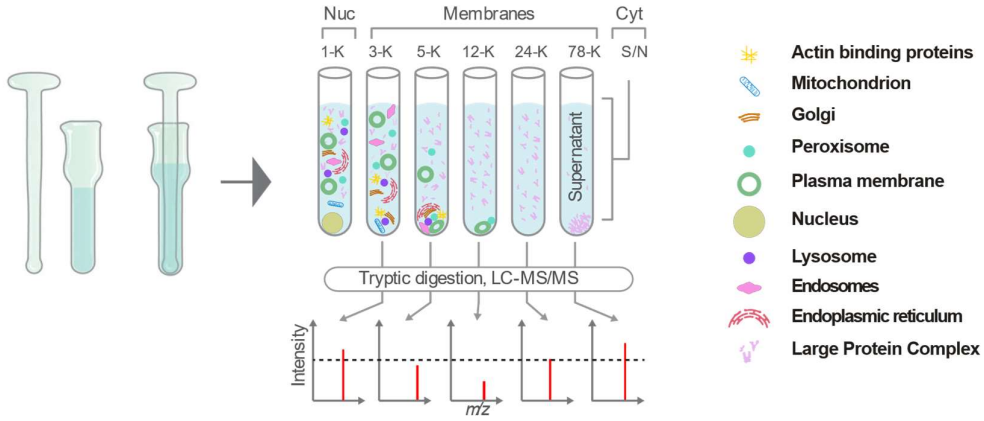

Figure 2.2: Workflow of differential centrifugation
WT and Cyth2-deficient C2 myoblasts were lysed using a dounce homogenizer. Samples were then subjected to sequential centrifugation steps with increasing centrifugation speed. Based on the different precipitation behavior cellular membranous compartments are separated into an array of fractions. Fractions containing organelles and protein complexes, but not the nuclei (1-K) or soluble monomeric proteins (supernatant of 78-K) were analyzed by HPLC/MS to determine protein abundance. Modified from (Itzhak et al. 2016). Nuc, Nuclear fraction; Cyt, Cytosolic fraction.

2.2.8.1 Organellar fractioning by differential centrifugation

To access global changes in organelle size, shape or density by depletion of *Cyth2*, differential centrifugation of homogenized cells was performed, followed by mass spectrometric analysis of the different fraction. Differential centrifugation separates cellular organelles by sedimentation behavior, assuming that larger organelles (e.g., the nucleus) already pellet at low g-forces, while smaller organelles (e.g., peroxisomes) stay in suspension and need higher centrifugation speed for

sedimentation. An adapted experimental procedure from Itzhak and colleagues was conducted (Fig. 2.2; [169]; adaptation by Felix Meissner Lab, UKB). Differential centrifugation was performed in the laboratory with help from Dr. Bettina Jux. Samples were further processed, measured and data analyzed by Dr. Sebastian Kallabis (who provided the respective methods section) and Anushka Kudaliyanage (Felix Meissner Lab, UKB).

Briefly, C2 cells were harvested and washed once in ice-cold hypotonic lysis buffer (see below). Cells were lysed in hypotonic lysis buffer in a dounce homogenizer with 20 strokes. Cell homogenate was immediately mixed with 10% v/v hypertonic sucrose buffer to restore the sucrose concentration to 250 mM. The cell lysate/supernatant was sequentially centrifuged at 1000 g, 10 min.; 3000 g, 10 min.; 5500 g, 15 min.; 12200 g, 20 min; 24000 g, 20 min.; 78400 g, 30 min. The pellet was resuspended in modified RIPA-buffer (see below). Samples were stored at -20 °C until analysis.

- Hypotonic lysis buffer: 25 mM Tris pH 7.5, 50 mM Sucrose, 0.2 mM EGTA, 0.5 mM $MgCl_2$, protease inhibitors (2.2.5.1)
- Hypertonic sucrose buffer: 25 mM Tris pH7.5, 2.5 M Sucrose, 0.2 mM EGTA, 0.5 mM $MgCl_2$, protease inhibitors (2.2.5.1)
- Modified RIPA buffer: 150 mM NaCl, 1%TritonX100, 0.5% NaDoc, 0.1% SDS, 50 mM Tris pH7.5, protease inhibitor (2.2.5.1)

2.2.8.2 Mass spectrometry of organellar fractions

Proteins enriched in organellar fractions as well as from total cell lysate were denatured using urea lysis buffer (see below). After incubation at RT for 30 min, urea concentrations were diluted to less than 1 M using 50 mM Tris-HCl. Proteins were enzymatically digested at RT with Trypsin/Lys-C at a 1:100 enzyme-to-protein ratio for 16 hours. On the next day, the digestion was stopped by adding 10% formic acid to a final concentration of 1% and peptides were desalted using a modification of the stage tip protocol [170]. In-house-made polystyrene-divinylbenzene reversed phase sulfonate (SDB-RPS) double-layer stage tips were activated by the addition of 100 µl pure methanol. Tips were washed with 100 µl buffer B (see below) and equilibrated with 100 µl buffer A (see below). Digested peptides were loaded onto the stage tips

with a volume equivalent to 20 µg of initial protein input material and following were desalted by one wash of 100 µl buffer A and two washes of 100 µ buffer B. Elution of peptides was achieved by the addition of 60 µl of 1% ammonia in acetonitrile. After each step, centrifugation was carried out at 800 g for two minutes or until all liquid passed through the double layer. Finally, eluted peptides were vacuum-dried, and dissolved in buffer R (see below), peptide concentrations were determined, and 400 ng was used for injection into the liquid chromatography-mass spectrometry (LC-MS) system.

Proteomics measurements were carried out with an ultrahigh-performing liquid chromatography Easy nLC 1200 system coupled on-line to an Exploris 480 tandem mass spectrometer. Peptides were chromatographically separated on an in-house produced analytical column (30 cm length, 75 µm inner diameter, 1.9 µm ReproSil-Pur 120 C18-AQ filling material) and using a 90 min gradient consisting of buffer A and B. Starting at 4%, the amount of Buffer B was linearly increased to 25% over 70 min at a flow of 300 nl/min. Buffer B was then linearly increased to 55% over 8 min and finally to 95% within 2 min. The analytical column was washed at 95% B for another 10 min.

Eluting peptides were on-line-transferred into the MS system by nanoelectrospray ionization operated at a constant voltage of 2.4 kV. Samples were analyzed in data-independent acquisition (DIA) mode. In brief, full MS spectra were recorded at a resolution of 120,000, a scan range of 380-1,020 m/z, an AGC target of 100%, and an injection time of 55 ms. DIA fragment spectra were recorded at a resolution of 15,000, an AGC target of 1,000% and an injection time of 22 ms. In total, 75 DIA windows of 8 m/z window sizes were selected spanning a range from 400-1,000 m/z. Precursors were fragmented at an HCD collision energy of 31% and measured in centroid mode.

- Urea lysis buffer: 6 M urea, 2 M thiourea, 10 mM Tris-(2-carboxyethyl)-phosphine, 30 mM 2-chloroacetamide in 50 mM Tris-HCl pH 8.5
- Buffer B: 80 % acetonitrile, 0.1% formic acid in LC-MS-grade water
- Buffer A: 0.1% formic acid in LC-MS-grade water
- Buffer R: 2% acetonitrile, 1% formic acid in LC-MS-grade water

2.2.8.3 Data analysis of organellar fractions

Mass spectrometry raw data were processed with the DIA-NN software tool [171]. A spectral library was predicted *in silico* from the UniProt SWISS-PROT Mus musculus database (version from 2021-11-18) with trypsin as the digesting enzyme, maximum number of missed cleavages set to 1 and cysteine carbamidomethylation enabled as a fixed modification. The scan window radius was set to 7 and mass accuracies were fixed to 2.08e-05 (MS2) and 3.6e-06 (MS1), respectively. Precursor masses were fixed to min 380 m/z and max 1,020 m/z with peptide sequence lengths from 7-30. Peptide-spectra matches were filtered at an FDR<0.01. Identified precursors were further filtered in R on Lib.Q.Values and Lib.PG.Q.Values<0.01. Label-free quantified (LFQ) protein intensities were carried out with the maxLFQ algorithm implemented in the DIA-NN R package [172].

The statistical analysis was performed with the Perseus software suite (v. 1.6.15; [173]). The following steps were performed consecutively to identify proteins which changed organellar localization upon protein KO. Firstly, summed intensities were calculated for each protein within wildtype or KO separately. Summed intensities were then subtracted individually from intensities in each fraction to get relative protein abundance. Delta abundance per protein was calculated per fraction by subtracting KO relative abundance from WT relative abundance to reveal proteins changing organellar localization upon genotype. Only proteins present in each fraction of KO and WT were considered for multidimensional significance testing (threshold = 0.05, Quantile = 0.55, iterations = 100, Benjamini-Hochberg FDR). Proteins with significantly different localizations were Z-score normalized and used for hierarchical clustering (Euclidean distance, clustering = k-means, 300 starting points, 10 iterations). Finally, enriched gene ontology terms enriched in individual clusters compared to all proteins were identified by Fisher's Exact testing (Benjamini-Hochberg FDR = 0.05).

2.2.9 Mass spectrometry of neonatal plasma

Mass spectrometry of neonatal plasma was performed by Dr. Marc Sylvester (Core Facility Analytical Proteomics, University of Bonn). Data analysis was performed by Dr. Farhad Shakeri and Andreas Buness (Core Unit for Bioinformatics

Data Analysis, University of Bonn*)*. They also provided the following methods section.

All chemicals were purchased from Sigma unless otherwise noted (Sigma-Aldrich). Plasma samples were centrifuged for 1 min at 2,000 g. Of the supernatant, 50 µg of protein per plasma sample were subjected to in-solution digestion with the iST 96x sample preparation kit according to manufacturer's recommendations (3 h digestion).

Peptides were separated with a Dionex Ultimate 3000 RSLC nano HPLC system. 10 µg peptides were dissolved in 10 µL 0.1% formic acid (FA, solvent A) and 1 µl was injected onto an analytical column (400 mm length, 75 µm inner diameter, ReproSil-Pur 120 C18-AQ, 3 µm). Peptides were separated during a linear gradient from 5% to 35% solvent B (90% acetonitrile, 0.1% FA) at 300 nl/min over a 180 min. The LC was coupled to an Orbitrap Fusion Lumos mass spectrometer. Data-independent acquisition was performed with the following scan parameters: 47 windows of 15 Da plus 0.5 Da overlap covering m/z 399.5 to 1105.5. Isolated ions were fragmented with higher energy collision induced dissociation (HCD) with 22%, 27%, and 32% stepped collision energy. Fragments were detected in the Orbitrap detector (profile mode) with a resolution of 30,000 in the range of 200-1800 m/z. AGC target was 500,000, maximum injection time 50 ms. Every 3 s an MS1 scan was recorded in the range of 350-1500 m/z, resolution = 120,000.

Data processing was performed with DIA-NN 1.8.1 [171] in library-free mode based on the Uniprot mouse reference proteome with isoforms (2023_03). The following parameters were applied: tryptic cleavage with one missed cleavage, variable modification of methionine by oxidation, acetylation of protein N-terminus, static modification of cysteine by carbamidomethylation, output filtered at 1% FDR.

The statistical analyses of the DIA-NN precursor ion quantities were carried out in the R environment (R version 4.2.3; [174]) using an in-house developed workflow. Quantities with more than 65% missing values were removed. The data were variance-stabilized and transformed using the VSN package version 3.64.0 [175] and missing values were imputed using the method "v2-mnar" of the msImpute package version 1.6.0 [176]. The data were aggregated on protein level using Tukey's median polish method. The statistical analysis to identify differentially

abundant proteins was performed with the limma package version 3.52.4 [177]. To account for correlations, present in the same litter of mice, litter was modelled as random effect in the statistical analysis while using litter as blocking parameter in the function duplicateCorrelation. The resulting p-values of the statistical contrast between the KO and wildtype condition were adjusted for multiple testing and the false discovery rates (FDR) were calculated by the Benjamini-Hochberg method.

2.2.10 Statistics and computational analysis

Statistical analysis and data processing not described in the respective sections was performed using Microsoft Excel and GraphPad Prism 9.0 and 10.0. The statistical tests used are denoted in the figure legends, p-values below 0.05 were considered significant. Graphs were prepared using GraphPad Prism, R Studio [174], and Perseus [173].

3 Results

3.1 Analysis of *Cyth2*-deficient mice

The role of *Cyth2* was intensively studied in cell models and biochemical assays, but there is next to no *in vivo* research on *Cyth2*. The few studies involving animal models that investigated the function of *Cyth2* were performed with the pan-cytohesin inhibitor SecinH3, or based on conditional KO models for *Cyth2*. Therefore, *Cyth2*-deficient mice were generated in the laboratory and the phenotypic outcome was analyzed.

3.1.1 Full-knockout postnatal lethality is accompanied by impaired feeding

Breeding statistics revealed that homozygous mutants for *Cyth2* were absent at the age of three weeks in the mouse colonies (Fig. 3.1A). Genotyping of mice at this age identified about 33% of animals to be wildtype and 67% bearing the *Cyth2* mutation heterozygously, which corresponds to the Mendelian ratios if the homozygous mutation is considered to be lethal. To further investigate the lack of homozygous mutants at the age of three weeks, newborn mice from plug-matings were analyzed and genotyped. At P0, the average litter size was considerably increased compared to P21, and genotyping identified around 25% WT, 50% heterozygous and 25% homozygous mutants, corresponding to the Mendelian ratios. Pups were weighed and observed over two days. While WT and heterozygous pups appeared healthy in the presence of their mother, all homozygous mutants died on the day of birth, starting from 8-10 h (Fig. 3.1B). Interestingly, while heterozygous mutants thrived comparable to their WT litter mates, they showed a significantly lower body weight 1-2 h after birth (Fig. 3.1C; 1.33±0.11 g and 1.28±0.10 g). This observation was even stronger for homozygous KO mice (1.25±0.11 g), which additionally showed a suckling defect, as milk spots were never observed on these animals (Fig. 3.1D). In contrast, both WT and heterozygous mutants displayed normal suckling behavior.

There is a broad range of life-threatening complications in the postnatal phase and a variety of genetic mouse models were described to cause perinatal death. It has been observed that mutations causing respiratory failure or birth trauma often lead to postnatal death within 1-2 h after birth [178]. *Cyth2*-deficient newborns survived this period and did not show any obvious difficulties in breathing during that time or any physical deformations (Fig. 3.1D). Generally, apart from the mildly reduced body size, KO animals looked similar to their WT littermates. Furthermore, dissection and gross comparison of the inner organs 6 h after birth did not reveal any macroscopic anatomic differences between WT and KO neonates (data not shown). The lifespan of *Cyth2* KO pups fell in a range comparable to genetic models causing homeostatic issues or the inability to suckle [178].

We could never observe suckling KO pups or find any milk in their stomachs after dissection, whereas both were seen for WT animals. However, motherly behavior towards the pups was comparable between all littermates irrespective of the

A

stage	litter	total	+/+	+/-	-/-
P21	16	80 (5)	28 (35.0%)	52 (65.0%)	0
P 0	35	259 (7.4)	70 (27.0%)	131 (50.6%)	58 (22.4%)

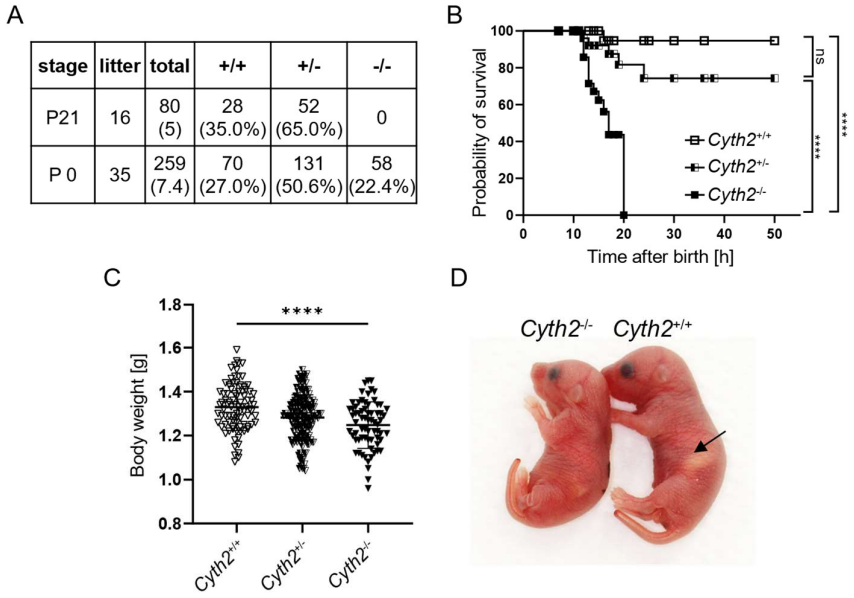

Figure 3.1: *Cyth2* is vital for perinatal survival of newborn mice
A) Genotypic counts of litters from *Cyth2*$^{+/-}$x*Cyth2*$^{+/-}$ breedings at P0 and P21. **B)** Kaplan-Meier graph showing the survival probability of *Cyth2*$^{+/+}$, *Cyth2*$^{+/-}$ and *Cyth2*$^{-/-}$ mice after birth (n≥40). **C)** Body weight of newborn (1-2 h after birth) *Cyth2*$^{+/+}$, *Cyth2*$^{+/-}$ and *Cyth2*$^{-/-}$ mice. Depicted is the average body weight ±SD, each symbol represents an individual mouse (n=87, 164, 69, respectively). **D)** Exemplary image of *Cyth2*$^{+/+}$ and *Cyth2*$^{-/-}$ pups. The black arrow indicates a milk spot clearly visible in the WT animal but lacking in the KO neonate. Statistical significance was tested by Log-rank test and one-way ANOVA (****p < 0.0001). Data are pooled observations collected during this work and by Dr. Bettina Jux before..

genotype. Movement and normal opening of the mouth did not indicate any general morphological or neuromuscular defects in *Cyth2*-deficient mice. Still, both these possibilities could not be ruled out, while additionally homeostasis might be compromised by the loss of *Cyth2*.

3.1.2 Liver-specific knockouts reveal a metabolic involvement of *Cyth2*

To narrow down the potential cause of death in *Cyth2*-deficient newborns, the expression of CYTH2 in various neonatal tissues was analyzed by Western Blot. As reported before, CYTH2 protein was ubiquitously expressed, with the highest levels found in organ lysates of the brain, kidneys and lungs (Fig. 3.2A; [179, 180]). Additionally, a series of tissue-specific KO mouse lines had been generated and their phenotypes analyzed in the laboratory. However, none of the tested conditional KOs did pheno-copy the perinatal lethality of *Cyth2* full-KOs. Based on the Cre-driver lines used, neuromuscular (*Nes*-&*Myog*-Cre; [181, 182]), liver-specific (*Alb*-Cre; [183]), myeloid-specific (*LysM*-Cre; [184]), or cardiac (*Myh6*; [185]) defects were ruled out to be the single cause of perinatal death of *Cyth2*-deficient mice (Fig. 3.2B). The conditional KO lines were vital and showed no obvious phenotype, except for the *Myh6*-dependent KO of *Cyth2* in cardiomyocytes. These mice developed cardiac hypertrophy and died prematurely (Fig. 3.2B, C), which was extensively investigated during this work and by Dr. Bettina Jux. However, throughout this work, it was published that cardiac hypertrophy and premature death is an artificial phenotype caused by the driver line used and therefore cardiac hypertrophy cannot be attributed to the *Cyth2* deficiency [186].

Moreover, based on earlier findings that *Cyth3* in the murine liver and the *Cyth2* orthologue steppke are required for full insulin receptor signaling, liver-specific *Cyth2* KO mice were analyzed by Dr. Bettina Jux [150, 151]. First,

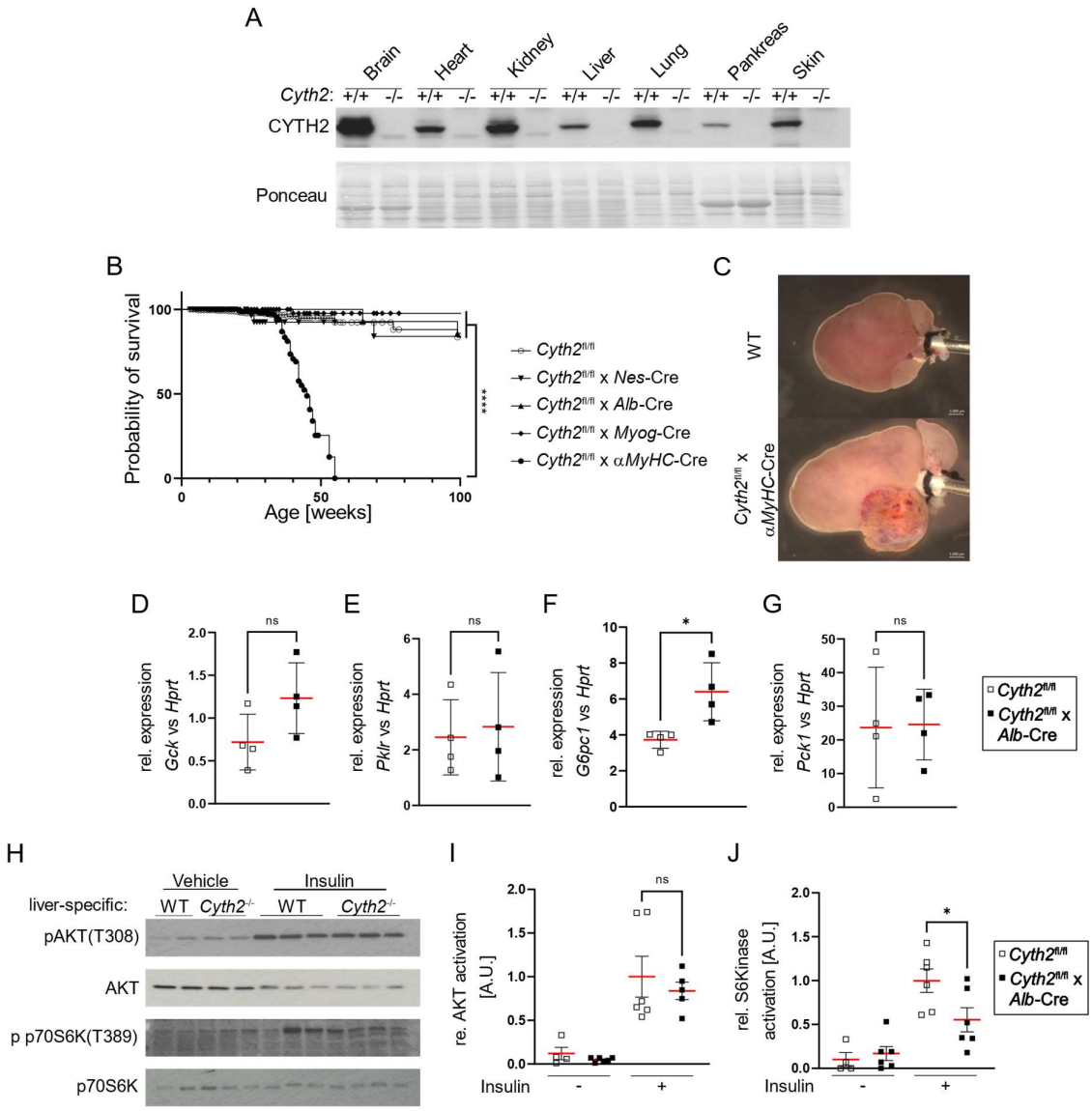

Figure 3.2: *Cyth2* is involved in hepatic insulin signaling
A) Exemplary Western Blot analysis of CYTH2 expression in neonatal organs (as indicated) of WT and knockout mice. Ponceau staining served as a loading control. **B)** Kaplan-Meier graph depicting the survival probability of organ-specific knockout mice for brain (*Nes*-Cre), liver (*Alb*-Cre), skeletal muscle (*Myog*-Cre) and heart (*Myh6*-Cre) compared to floxed allele. Each symbol represents an individual mouse (n≥14). **C)** Representative images of control and *Cyth2*-deficient hearts isolated from aged (42 weeks old) mice, fixed on a cannula inserted into the aorta (scale bars indicate 1000 µm). **D-G)** Gene expression analysis of hepatic tissue from liver-specific *Cyth2* knockout mice by semi-quantitative PCR of D) *Gck*, E) *Pklr*, F) *G6pc1* and G) *Pck1* normalized to *Hprt*. Red lines indicate relative mean expression ±SD; each symbol represents an individual animal (n=4). **H-J)** Insulin signaling in hepatic tissue from adult liver-specific *Cyth2* knockout mice analyzed by Western Blot of phosphorylated (activated) AKT and S6K. H) Representative Western Blots of phosphorylated AKT and S6K from adult WT and liver-specific knockout mice treated with or without insulin. Total AKT and S6K served as loading controls. Organs were isolated 10 min after intraperitoneal insulin injection and snap-frozen in liquid nitrogen. Semi-quantitative analysis of I) AKT and J) S6K phosphorylation. Phosphorylated signals were normalized to total protein signals. Red lines indicate relative mean intensity ±SD; each symbol represents an individual animal tested (n≥4). Statistical significance was tested by Log-rank test, Mann-Whitney test, and 2way ANOVA (*p < 0.05, ****p < 0.0001, ns = not significant). Analysis of *Alb*-Cre and *Nes*-Cre mice was performed by Dr. Bettina Jux before. G6pc1; Glucose-6-phosphatase catalytic subunit 1; Gck, Glucokinase; Pck1, Phosphoenolpyruvate carboxykinase 1; Pklr, Pyruvate kinase L/R.

mRNA expression of glycolysis and gluconeogenesis genes in the liver was assessed by qPCR (Fig. 3.2D-G). While the glycolytic enzymes glucokinase (*Gck*) and pyruvate kinase L/R (*Pklr*) were unaffected by loss of *Cyth2* in the liver of *Cyth2*$^{fl/fl}$xAlb-Cre mice (Fig. 3.2D, E), the gluconeogenic glucose-6-phosphatase (*G6pc1*) was significantly upregulated (~1.7-fold) in KO animals (Fig. 3.2F). No difference was detected between *Cyth2*-expressing or -deficient livers for phosphoenolpyruvate carboxykinase 1 (*Pck1*), another enzyme involved in gluconeogenesis (Fig. 3.2G). Further, the insulin response of *Cyth2* KO liver tissue was analyzed by Western Blot after intraperitoneal administration of insulin. Insulin injection led to an increase in AKT and p70S6K phosphorylation compared to unstimulated controls as expected (Fig. 3.2H-J; [187, 188]). However, while the levels of pAKT(T308) were comparable between WT and *Cyth2*-deficient livers, the phosphorylation of S6K further downstream was significantly reduced in *Cyth2*-deficient livers (Fig. 3.2H-J).

3.1.3 *Cyth2*-deficient newborns have elevated levels of circulating plasma amino acids

Hampered signaling upon insulin stimulation and deregulated gene expression of *G6pc1* in *Cyth2*-deficient livers indicate the involvement of *Cyth2* in metabolic processes. In the early postnatal period, glucose levels need to be maintained via gluconeogenesis, as nutrition from feeding is not available yet [189]. It has been described that mice lacking a controlling transcription factor, CEBPa (CCAAT Enhancer Binding Protein Alpha), die within 8 h after birth, most likely due to dramatically reduced blood glucose levels [189, 190].

In investigating further, blood glucose levels and the expression of gluconeogenesis genes in hepatic tissue of *Cyth2* full-KO mice were measured. The blood glucose concentration was indistinguishable between WT and KO pups (Fig. 3.3A). Interestingly though, the expression levels of *G6pc1* and *Pck1* mRNA were significantly elevated (by ~1.6-fold) in livers of *Cyth2*-deficient newborns compared to their WT litter mates (Fig. 3.3B, C), corresponding to elevated *G6pc1* expression in liver tissue of *Cyth2*-Alb-Cre mice (Fig. 3.2F).

Besides glucose, amino acids provided by autophagic degradation of proteins in various organs have been reported to serve as a nutritional supply in the postnatal period. Autophagy-deficient mice die a few hours after birth and it was proposed that these animals starved to death [191]. Accordingly, in autophagy-deficient KO animals, the levels of free amino acids were reported to be reduced compared to WT controls. However, measuring free L-amino acids in the plasma of neonates revealed significantly higher concentrations of amino acids in *Cyth2*-deficient newborns (5.9±1.2 mmol/l) compared to WT (4.2±0.6 mmol/l) littermates (Fig. 3.3D).

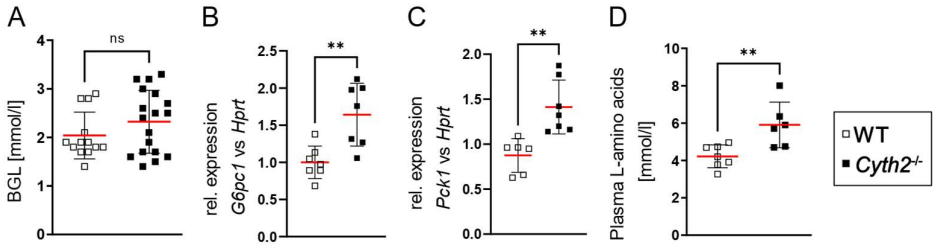

Figure 3.3: *Cyth2* controls perinatal metabolic homeostasis
A) Blood glucose levels in WT (n=13) and *Cyth2* knockout (n=18) animals six hours after birth. **B-C)** Gene expression analysis of hepatic tissue from WT (n=7) and *Cyth2* knockout (n≥6) neonates by semi-quantitative PCR of B) G6pc1 and C) Pck1 normalized to HPRT. **D)** Plasma amino acid concentrations in WT (n=7) and *Cyth2*-deficient (n=6) pups six hours after birth. Red lines indicate average ±SD; each symbol represents an individual pub. Statistical significance was tested by Mann-Whitney test or Student's unpaired t-test (*p < 0.05, **p < 0.01, ns = not significant). Real-time PCR on liver tissue was performed by Dr. Bettina Jux.

Taken together, this study describes for the first time the essential role of *Cyth2* in the postnatal period of mice. *Cyth2*-deficient newborns showed a suckling defect, elevated levels of gluconeogenesis gene expression in hepatic tissue as well as increased concentrations of plasma amino acids. Otherwise, no obvious morphological or behavioral deficits were identified based on the observation of the live neonates and their dissection after six hours. None of the conditional *Cyth2* KO mouse lines analyzed in the laboratory could pheno-copy the full-KO lethality.

3.2 Full mTOR signaling requires *Cyth2* in muscle progenitor cells

Starvation or stimulation experiments with newborn mice were not feasible due to practical and ethical reasons. As a result, a cell model for a more detailed mechanistic analysis was utilized: the C2 myoblast cell line first described in [161]. In contrast to many other cell lines used in laboratories worldwide, C2 myoblasts are not transformed by oncogenic overexpression, but are rather naturally kept in a proliferative state by suitable culture conditions. Further, it is possible to differentiate these precursor cells into functional, contracting myotubes as a model for mechanotransduction research [161]. To exploit these features at the time, *Cyth2*-deficient myoblasts were generated using the CRISPR/Cas9 system (as described in section 2.2.7). Single-cell clones were generated and validated by Western Blot for CYTH2 (Fig. 3.4A). Morphologically, WT and *Cyth2*-deficient myoblasts showed no obvious difference under standard culture conditions (data not shown). In the following, these cells were analyzed regarding changes in signaling.

3.2.1 *Cyth2*-deficient myoblasts show distorted mTOR signaling

mTOR signaling is regulated on various levels to integrate nutrient availability, DNA integrity, growth factor signaling, and energy availability [85]. Based on the metabolic abnormalities in *Cyth2* full-KO mice the steady-state impact of *Cyth2* on metabolic signaling in C2 myoblasts was assessed first. Therefore, the phosphorylation levels of mTOR target proteins in WT and *Cyth2* KO cells after two days of standard culture were analyzed by Western Blot (Fig. 3.4). Compared to WT cells, the phosphorylation of ULK1 and S6K downstream of mTORC1 was significantly reduced in *Cyth2*-deficient myoblasts, by ~50% and ~25%, respectively. In contrast, p4E-BP1(T36/47) levels were ~1.5-fold higher in KO cells and the pAKT(S473) signal downstream of mTORC2 was unaffected (Fig. 3.4B, upper row). Furthermore, pAKT(T308) levels were unaffected by the loss of *Cyth2*, indicating intact growth factor signaling upstream of mTOR in KO myoblasts. In validating whether altered protein levels of the analyzed mTOR targets could explain the altered phosphorylation levels, the expression of ULK1, S6K, and AKT was measured. No significant difference for the total amount of these proteins was

detected between WT and *Cyth2*-deficient C2 myoblasts (Fig. 3.4B, central row). AMPK is a sensor for the ATP concentration in a cell and signals low levels of energy to mTOR by phosphorylation of the kinase and up- and downstream components of the mTOR signaling cascade [100, 101, 85, 192].

The phosphorylation and the total protein amount of AMPK were both mildly but significantly reduced in *Cyth2* KO myoblasts compared to WT cells (~35% and ~20%, respectively). The levels of pRaptor(S792) downstream of AMPK were comparable between WT and KO myoblasts (Fig. 3.4B, lower row).

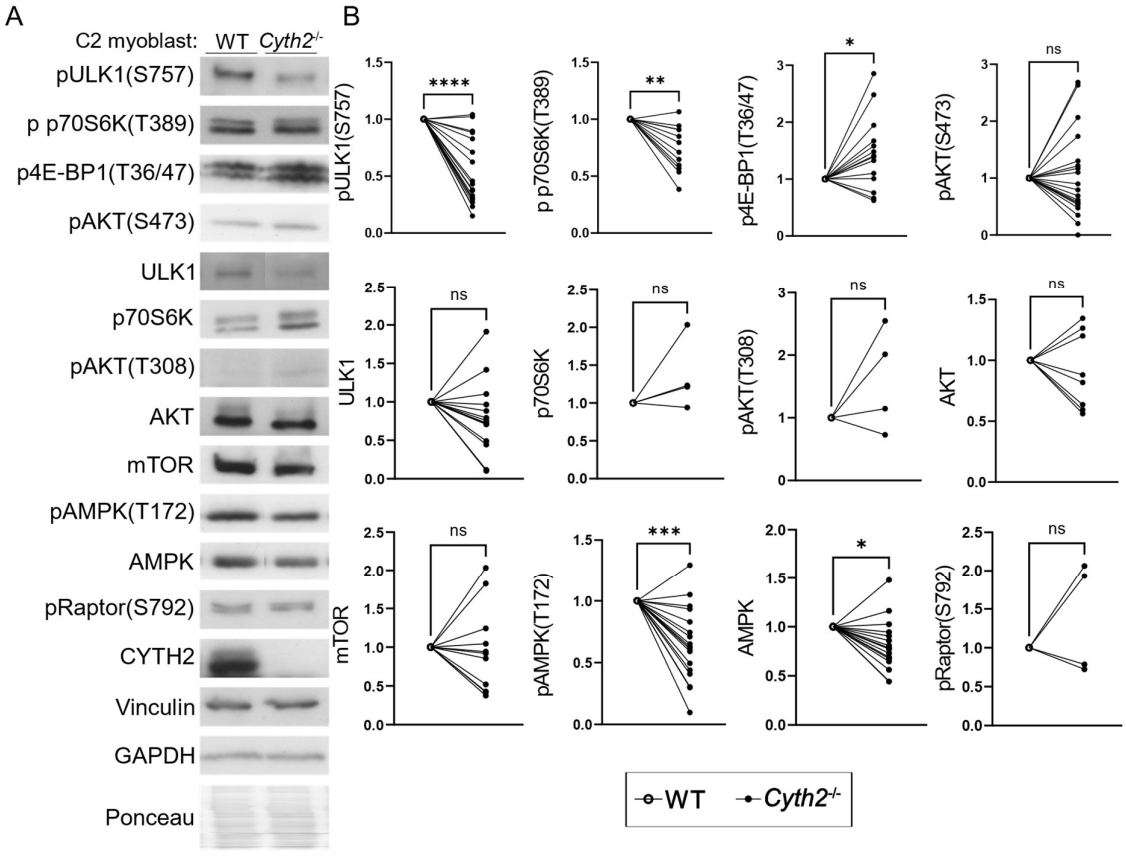

Figure 3.4: *Cyth2* balances mTOR downstream signaling in muscle precursor cells
A) Representative Western Blots of phosphorylated mTOR target proteins, total protein controls and associated signaling events in lysates from WT and *Cyth2*-deficient myoblasts after two days standard culture conditions. **B)** Semi-quantitative analysis of the Western Blot analysis shown in A), normalized to total protein loaded as determined by Ponceau staining and further normalized to the WT condition. Each dot represents an independent experiment (n≥4). Statistical significance was tested by Wilcoxon test (*p < 0.05, **p < 0.01, ***p < 0.001, ****p < 0.0001, ns = not significant).

3.2.2 Altered mTOR signaling in *Cyth2*-deficient myoblasts has only minor functional consequences

As distorted mTOR signaling is observed in a variety of diseases and often accompanied by morphological, proliferative or metabolic changes [85] the proliferation rates of WT and KO cells under standard culture conditions were assessed using a neutral red assay. Interestingly, and in contrast to the expectations based on decreased S6K phosphorylation, significantly shorter doubling times were observed for *Cyth2* KO cells (13.5±2.9 h) compared to their WT counterparts (17.7±1.8 h; Fig. 3.5A). The metabolic state was estimated with a Seahorse analyzer performing Glycolytic and Mito-Stress tests. These assays detected mildly reduced oxidative respiration in *Cyth2*-deficient myoblasts compared to WT controls (Fig. 3.5B), but no difference in glycolytic parameters between WT and KO cells (Fig. 3.5C). Additionally, the cellular volume of C2 myoblasts was measured by surface protein staining and immunofluorescence imaging. Three-dimensional reconstitution based on z-stack data showed no significant volume difference between WT and *Cyth2*-deficient cells (Fig. 3.5D). Based on the decreased phosphorylation of ULK1 (Fig. 3.4), autophagic activity was assessed in C2 myoblasts. The protein levels of p62 and LC3b, adaptor and marker proteins of autophagy, were analyzed in WT and *Cyth2* KO cells under standard culture conditions (Fig. 3.5E-F). No significant differences for p62 were detected by Western Blot but increased levels of LC3b were found, both in its steady state form (LC3b I) as well as the autophagy-induced lipidated form (LC3b II). LC3b II/I ratios were not different between WT and KO, though (data not shown). Also, the lysosomal marker LAMP1 was comparable between WT and KO myoblasts (Fig. 3.5E-F).

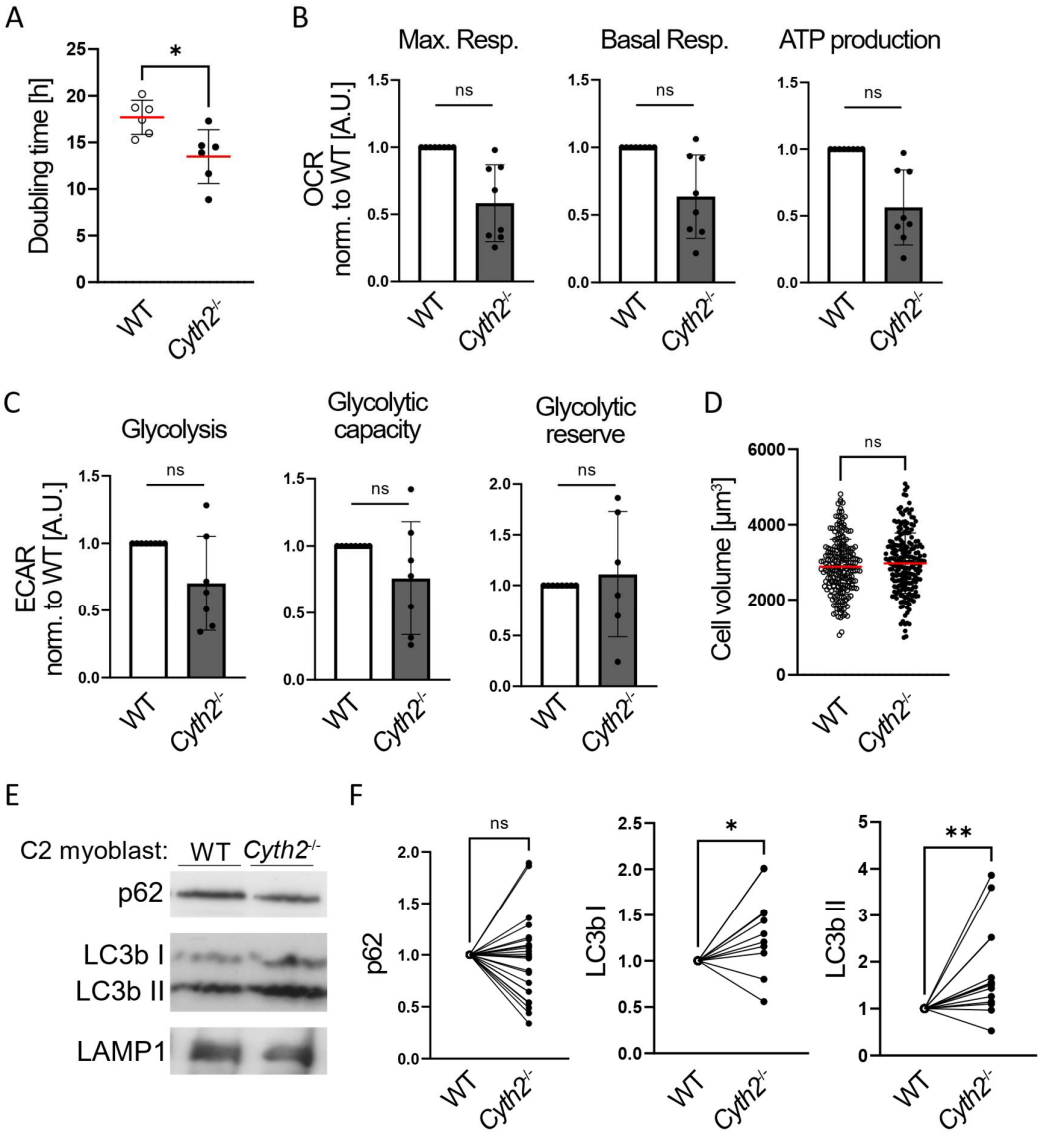

Figure 3.5: Functional consequences of *Cyth2* modulating mTOR signaling appear negligible
A) Doubling times of WT and *Cyth2*-deficient myoblasts estimated by Neutral Red staining of cells, performed as technical triplicates including two pairs of clones (n=6). **B-C)** Metabolic activity of WT and knockout cells was assessed with the B) Seahorse mito-Stress test and the C) Seahorse glycolytic stress test. Results were normalized to WT controls and show averaged OCR and ECAR ±SD for the metabolic parameters indicated. Experiments were performed with five technical replicates (n≥5). **D)** Cell volume of WT and knockout myoblasts determined by fluorescence microscopy and 3D reconstruction with Imaris 9. Data are pooled from three independent experiments including two pairs of WT and KO clones, each dot representing a cell analyzed (WT n=221, KO n=208). **E)** Representative Western Blots of p62, LC3b and LAMP1 in lysates from WT and *Cyth2*-deficient myoblasts after two days standard culture conditions (as in Fig. 4A). **F)** Semi-quantitative analysis of the Western Blot analysis shown in E), normalized to total protein loaded as determined by Ponceau staining and further normalized to the WT condition (n≥11). Each dot represents an independent experiment (except for D)), red lines and bars represent average ±SD. Statistical significance was tested by Mann-Whitney test, Wilcoxon test (*p < 0.05, **p < 0.01, ns = not significant).

3.2.3 Loss of *Cyth2* does not alter general mTOR kinetics

An imbalanced mTOR signaling with decreased phosphorylation of ULK1 and S6K, despite increased phosphorylation of 4E-BP1 was observed in *Cyth2*-deficient myoblasts. The next step was to understand the kinetic response of mTOR in cells lacking *Cyth2*. Therefore, the mTOR signaling events between WT and KO cells during full starvation were analyzed (Fig. 3.6A). Additionally, rapamycin was applied to test if *Cyth2*-deficient cells were comparably susceptible to the mTOR inhibitor as their WT controls. After 1 h starvation the phosphorylation of ULK1, S6K, and AKT downstream of mTOR was completely absent and levels of p4E-BP1 reduced, both in WT and KO cells, without any obvious difference (Fig. 3.6A). The addition of rapamycin did not have any effect on starved cells, but repressed the phosphorylation of S6K in WT and *Cyth2*-deficient myoblasts under standard culture conditions (Fig. 3.6A). Interestingly, but in line with previous reports, the phosphorylation of ULK1 and 4E-BP1 was not affected by rapamycin [193–195]. The levels of phosphorylated AKT even increased since rapamycin only blocks the mTORC1 complex, which then feeds mTOR protein into the mTORC2 complex, causing an intermediate increase of downstream phosphorylation events (pAKT at S473; Fig. 3.6A).

Next, the response of WT and KO myoblasts towards re-supplementation of nutrients after a period of starvation was tested (Fig. 3.6B, C). Cells were deprived of medium for one hour and full medium was added afterwards. Cells were harvested at different time points and the mTOR signaling cascade was evaluated via Western Blot. The phosphorylation of ULK1 showed a clear delay in *Cyth2*-deficient myoblasts. These cells reached about 50% of the signal of WT cells after two hours (Fig. 3.6B, C left). In contrast, the phosphorylation of S6K and 4E-BP1 showed a similar increase in WT and *Cyth2* KO cells over the first two hours after replenishing nutrients (Fig. 3.6B, C right).

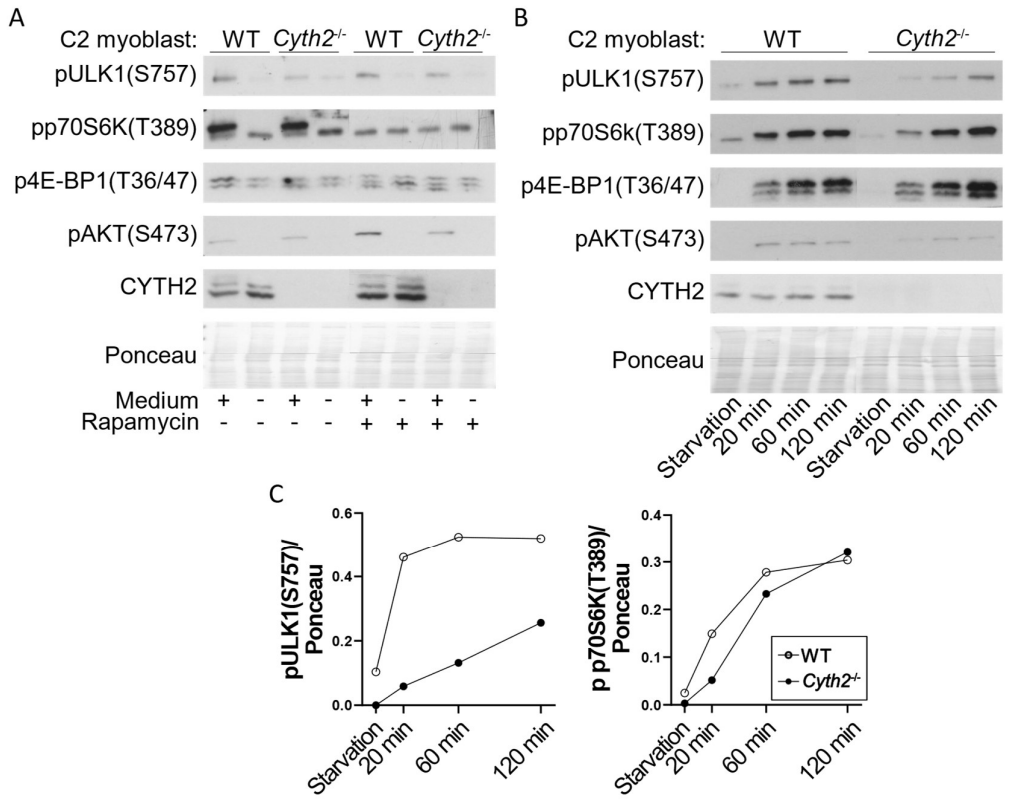

Figure 3.6: *Cyth2* specifically affects mTOR-dependent phosphorylation of ULK1
A) Representative Western Blots of phosphorylated mTOR target proteins in lysates from WT and *Cyth2*-deficient myoblasts after two days standard culture either untreated or treated with Rapamycin, in full medium or starving condition. **B)** Representative Western Blots of phosphorylated mTOR target proteins in lysates from WT and *Cyth2*-deficient myoblasts starved for one hour and subsequently re-stimulated with full medium for the indicated time points. **C)** Semi-quantitative analysis of the Western Blot analysis shown in B), normalized to total protein loaded as determined by Ponceau staining. Data are taken from one of three independent experiments, dots represent a single measurement, no statistical test was calculated.

3.2.4 ULK1 phosphorylation is decreased in *Cyth2* knockout myoblasts in response to amino acids

The re-supplementation kinetics indicated that the distorted mTOR signaling primarily affects ULK1 phosphorylation on S757, while phosphorylation of S6K and 4E-BP1 appeared to be unaffected. To investigate, whether a specific medium component triggers the difference in ULK1 phosphorylation between WT and *Cyth2* KO myoblasts, cells were starved from either glucose (and sodium pyruvate), FCS, or amino acids for two hours. Afterwards, the missing component was replenished for two hours and the cells harvested for Western Blot analysis. Of note, for these

experiments dialyzed FCS was used, which contains only residual amounts of smaller molecules (e.g., glucose or amino acids), to avoid interference of these FCS components with the starving condition.

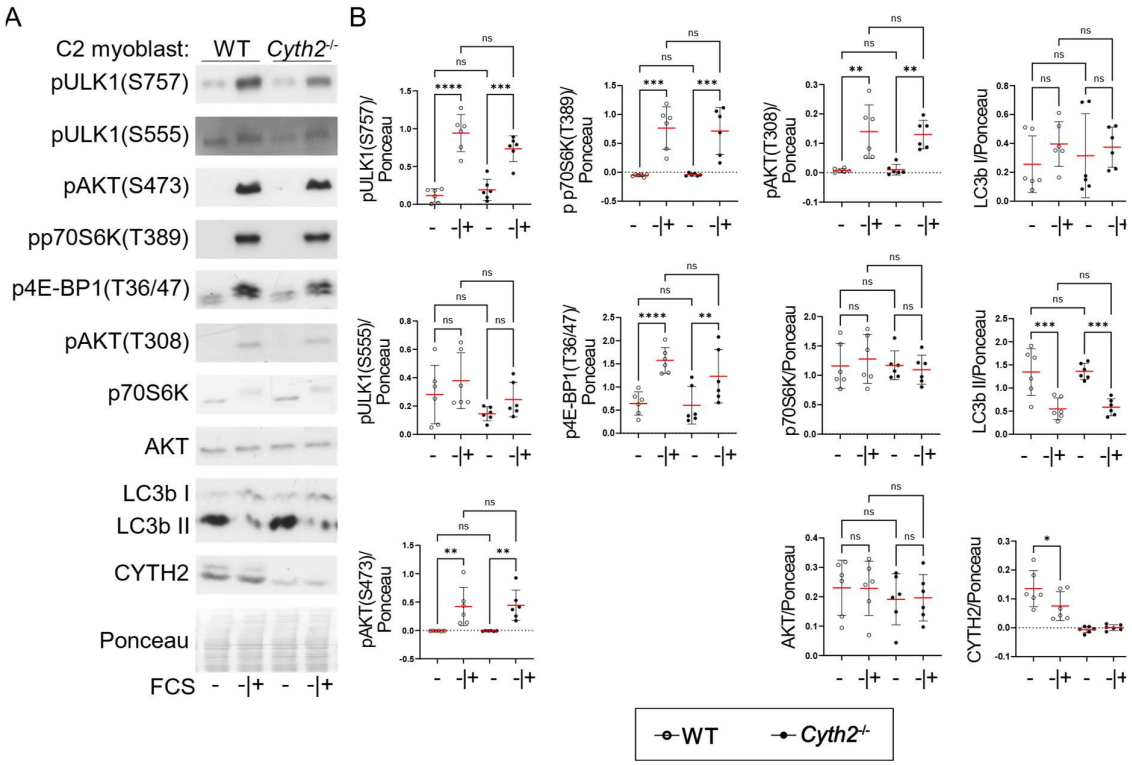

Figure 3.7: mTOR signaling remains unaffected by *Cyth2*-deficiency upon FCS stimulation
A) Representative Western Blots of phosphorylated mTOR target proteins, total protein controls and the autophagy marker LC3b in lysates from WT and *Cyth2*-deficient myoblasts after either two hours FCS starvation (-) or starvation and two hours re-stimulation (-|+). **B)** Semi-quantitative analysis of the Western Blot analysis shown in A), normalized to total protein loaded as determined by Ponceau staining. Each dot represents an independent experiment; red lines indicate average signal intensities ±SD (n=6). Statistical significance was tested by 2way-ANOVA (*p < 0.05, **p < 0.01, ***p < 0.001, ****p < 0.0001, ns = not significant).

First, the response of C2 myoblasts to FCS re-supplementation was assessed (Fig. 3.7). As expected, FCS replenishment induced the levels of pULK1(S757), pULK1(S555), pS6K(T389), p4E-BP1(T36/47), and pAKT(S473). Of note, the increase of pULK1(S555), a target site of AMPK, was only mild, while the other four target sites were significantly more phosphorylated (Fig. 3.7A, B left). However, no difference was observed between WT and KO myoblasts. AKT phosphorylation at T308 was induced upon FCS re-supplementation, but was comparable between WT and *Cyth2*-deficient cells. Similarly, there was no difference between S6K or AKT protein levels between the two genotypes (Fig. 3.7A, B third column). FCS also shut

off autophagy, as LC3b I levels increased while LC3b II levels decreased upon re-supplementation, both in WT and *Cyth2* KO cells. Notable, re-stimulation with FCS caused a significant reduction of CYTH2 protein levels by ~45% (Fig. 3.7A, B right).

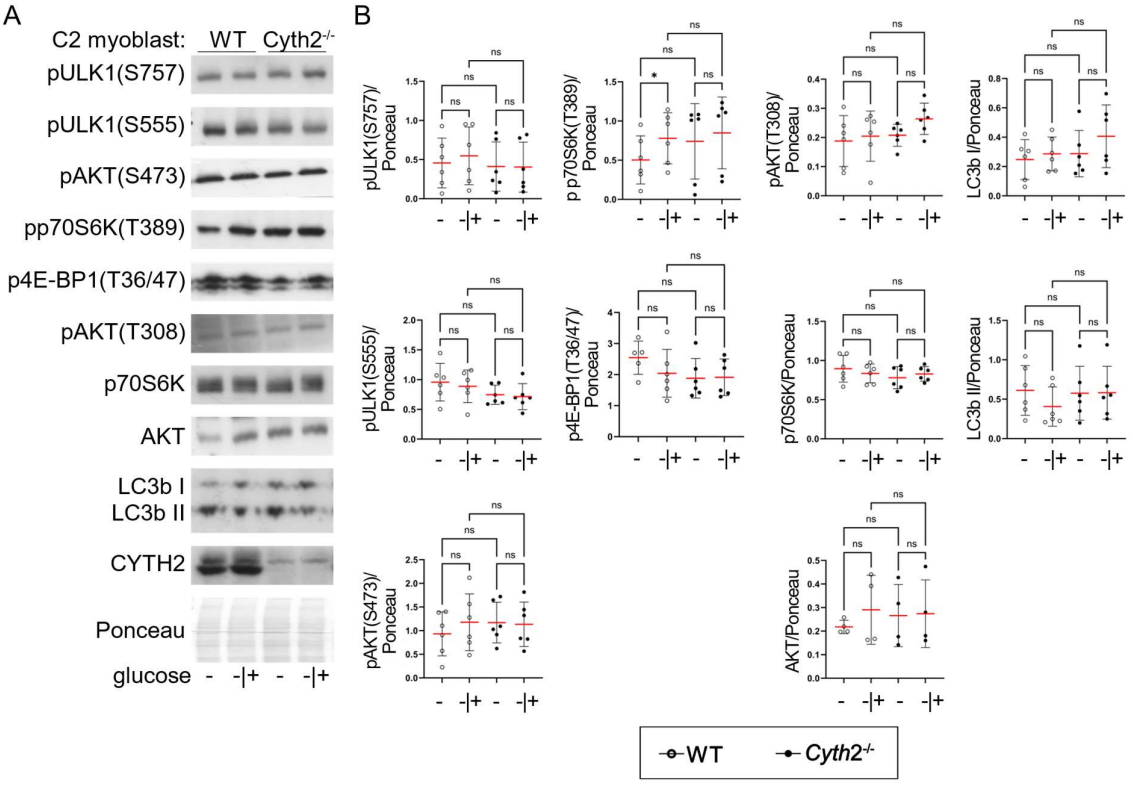

Figure 3.8: Glucose stimulation has negligible impact on mTOR signaling in C2 cells
A) Representative Western Blots of phosphorylated mTOR target proteins, total protein controls and the autophagy marker LC3b in lysates from WT and *Cyth2*-deficient myoblasts after either two hours glucose starvation (-) or starvation and two hours re-stimulation (-|+) with glucose and sodium pyruvate. **B)** Semi-quantitative analysis of the Western Blot analysis shown in A), normalized to total protein loaded as determined by Ponceau staining. Each dot represents an independent experiment; red lines indicate average signal intensities ±SD (n=6). Statistical significance was tested by 2way-ANOVA (*p < 0.05, ns = not significant).

Glucose re-stimulation had only minor effects on the phosphorylation of mTOR targets. Only pp70S6K(T389) was induced by re-supplementation of C2 myoblasts with glucose, but only in WT cells. Phosphorylation of ULK1, AKT and 4E-BP1 was unaffected by glucose or the depletion of *Cyth2* (Fig. 3.8A, B left). Additionally, the total levels of S6K and AKT were comparable in all four conditions, and no difference in the levels of LC3b I or II was detectable between starved and re-fed cells or the two genotypes (Fig. 3.8A, B right).

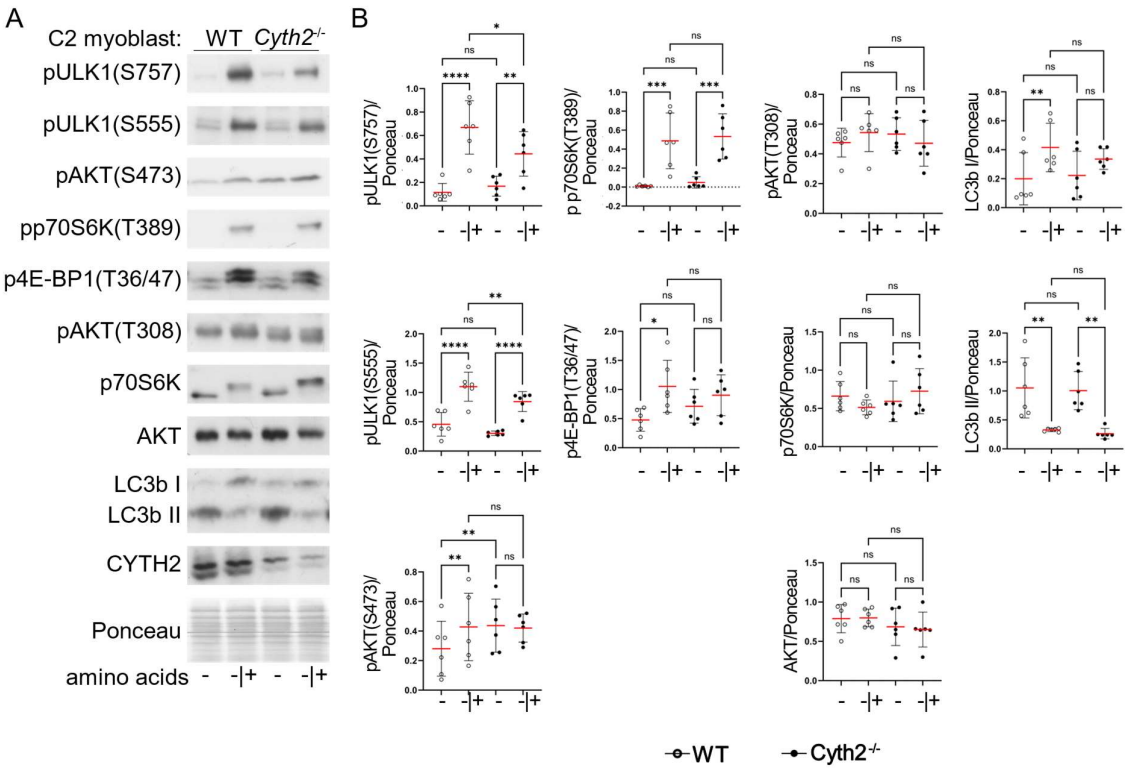

Figure 3.9: *Cyth2* fine-tunes mTOR signaling towards ULK1 phosphorylation upon amino acid stimulation
A) Representative Western Blots of phosphorylated mTOR target proteins, total protein controls and the autophagy marker LC3b in lysates from WT and *Cyth2*-deficient myoblasts after either two hours amino acid starvation (-) or starvation and two hours re-stimulation (-|+). **B)** Semi-quantitative analysis of the Western Blot analysis shown in A), normalized to total protein loaded as determined by Ponceau staining. Each dot represents an independent experiment; red lines indicate average signal intensities ±SD (n=6). Statistical significance was tested by 2way-ANOVA (*p < 0.05, **p < 0.01, ***p < 0.001, ****p < 0.0001, ns = not significant).

Finally, the re-supplementation of C2 myoblasts with amino acids was tested (Fig. 3.9). Re-feeding of amino acids strongly induced the phosphorylation of ULK1 at S757. Interestingly, the induction was weaker in *Cyth2*-deficient myoblasts, causing a significantly lower level of pULK1(S757) in KO cells (~66%) compared to WT controls (Fig. 3.9A, B left). Amino acids induced pULK1(S555) in WT and to a lower degree in *Cyth2* KO cells, but increased pAKT(S473) only in WT myoblasts, as KO cells remained high levels of pAKT(S473) under starving conditions. Phosphorylation of S6K and 4E-BP1 strongly increased upon amino acid stimulation. No difference was detectable between WT and *Cyth2*-deficient cells (Fig. 3.9A, B left). The levels of pAKT(T308), total S6K and AKT protein were comparable between all four conditions. LC3b I levels increased upon amino acid re-

supplementation while the LC3b II levels dropped significantly, without any difference between WT and KO cells (Fig. 3.9A, B right).

3.2.5 *Cyth2* deficiency does not alter the protein turn-over of ULK1

ULK1 phosphorylation was decreased in *Cyth2*-deficient myoblasts. The protein stability of ULK1 greatly depends on its phosphorylation status, which is also linked to ULK1 activity [122, 123]. For instance, activation of ULK1 induces its degradation by the proteasome, which could be a mechanism to limit autophagy induction by the kinase in a negative feedback loop [122].

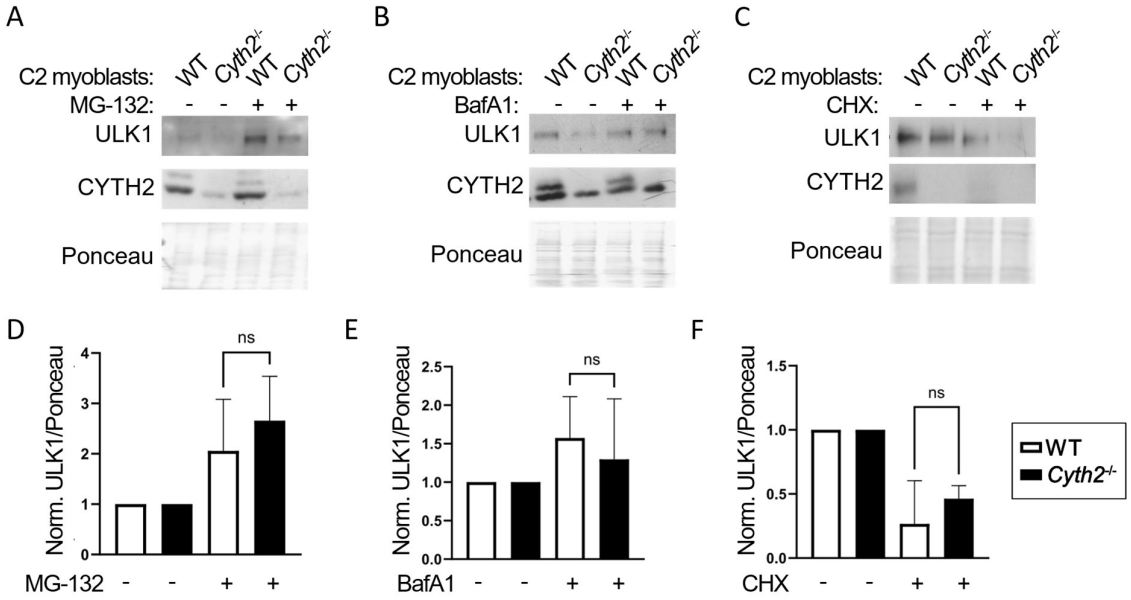

Figure 3.10: ULK1 protein turn-over is not affected by *Cyth2*
A-C) Representative Western Blots of ULK1 (and CYTH2) protein turn-over analysis by inhibition of WT and *Cyth2*-deficient myoblasts with A) 10 µM MG-132 for proteasome inhibition, B) 1 µM BafA1 to block lysosomal degradation or C) 50 µM CHX inhibiting protein synthesis compared to DMSO controls, each for 1 h. **D-F)** Semi-quantitative Western Blot analysis for ULK1 as in A-C), normalized to total protein loaded as determined by Ponceau staining, further normalized on the respective DMSO control. Bars indicate normalized mean signal intensity +SD (n=2-3). Statistical significance was tested by 2way-ANOVA (ns = not significant).

To determine if *Cyth2* deficiency changes the protein turn-over of ULK1 in C2 myoblasts, C2 myoblasts were treated with MG-132 to block the proteasome, with BafA1 to prevent the final degradation of autophagic content, and with CHX to block protein synthesis. Afterwards, ULK1 protein levels were analyzed by Western Blot (Fig. 3.10). Proteasome inhibition almost doubled the protein levels of ULK1 in WT

and *Cyth2*-deficient cells (Fig. 3.10A, D), while BafA1 only increased ULK1 signals by 1.4-1.5-fold (Fig. 3.10B, E). This indicates that the main degradation route for ULK1 is via the proteasome. However, there was no significant difference between WT and *Cyth2* KO cells, only a minor tendency of increased proteasomal degradation opposing a minor decrease in lysosomal degradation (Fig. 3.10D, E). When myoblasts were treated with the protein synthesis inhibitor CHX, ULK1 protein levels dropped by 60-70% in both WT and *Cyth2*-deficient cells without any significant difference between the two genotypes (Fig. 3.10C, F).

3.2.6 The cytohesin inhibitor SecinH3 specifically blocks ULK1 phosphorylation

Besides the genetic approach, CYTH2 activity was blocked with the pan-cytohesin inhibitor SecinH3 to test whether chemical intervention could pheno-copy the loss of *Cyth2* in C2 myoblast for the mTORC1-mediated phosphorylation of ULK1 (Fig. 3.11). SecinH3 blocks the cytohesin-dependent activation of small ARF-GTPases, without affecting ARF activation by BrefA-susceptible ARF-GEFs. For comparison BrefA was applied, which affects other ARF-GEFs than the cytohesin family [196, 149].

Focusing on ULK1 and S6K phosphorylation, BrefA treatment decreased the phosphorylation of both, ULK1 and S6K in WT and *Cyth2*-deficient cells (about 50% reduction in WT and KO cells). However, the reduction was significant only in WT myoblasts (Fig. 3.11A, C top). At the same time, total levels of ULK1 appeared to slightly increase in both genotypes upon BrefA treatment, while CYTH2 is stable and was not affected in WT cells (Fig. 3.11A, C bottom).

In contrast to BrefA, SecinH3 significantly reduced ULK1 phosphorylation in WT myoblasts (~30%) but showed no effect on this mTOR target in *Cyth2*-deficient cells (Fig. 3.11B, top). Additionally, SecinH3 had no significant effect on the phosphorylation of S6K in WT or *Cyth2*-deficient myoblasts (Fig. 3.11B, top). Further, SecinH3 did not affect the total levels of ULK1, but reduced the protein expression of CYTH2 significantly (Fig. 3.11B, D bottom).

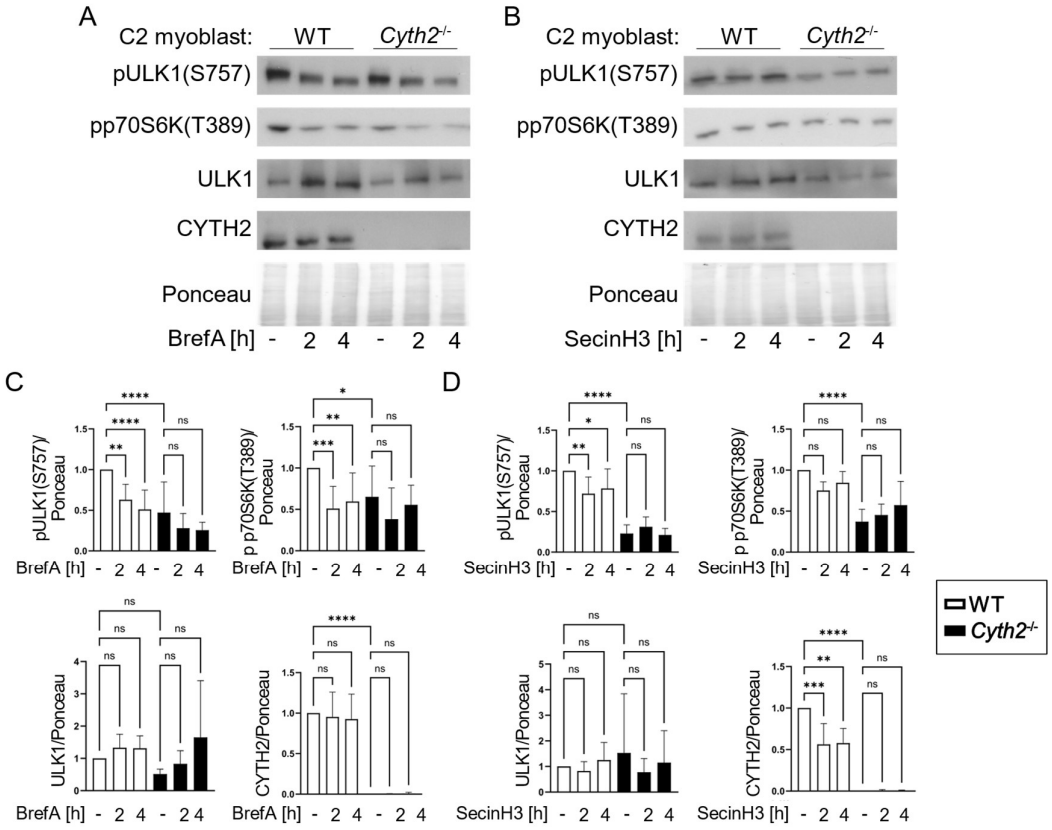

Figure 3.11: SecinH3 specifically inhibits ULK1 phosphorylation downstream of mTOR
A-B) Western Blot analysis of phosphorylated ULK1 and S6K in WT and *Cyth2*-deficient myoblasts after two and four hours of A) BrefA (5 µg/ml) and B) SecinH3 (50 µM) treatment compared to ethanol and DMSO controls, respectively. **C-D)** Semi-quantitative analysis of the Western Blot analysis shown in A-B), normalized to total protein loaded as determined by Ponceau staining, further normalized to the WT solvent control. Bars indicate average signal intensities +SD (n≥3). Statistical significance was tested by 2way ANOVA (*p < 0.05, **p < 0.01, ***p < 0.001, ****p < 0.0001, ns = not significant).

3.2.7 *Cyth2* deficiency reduces mTOR recruitment to lysosomes

One important aspect of mTOR activation is the recruitment of the kinase to the surface of lysosomes by the RAG-Ragulator-Complex, followed by the activation of mTOR by the GTPase RHEB [85]. To check, whether loss of *Cyth2* leads to defective

recruitment of mTOR to the lysosomes, WT and KO C2 myoblasts were co-stained after two days of standard culture conditions for LAMP2, a lysosomal marker, and mTOR. Analysis of z-stacks revealed a slightly but significantly decreased co-localization of LAMP2 and mTOR in *Cyth2*-deficient cells compared to WT controls. No obvious difference in staining intensities for LAMP2 or mTOR was observed (Fig. 3.12A, B).

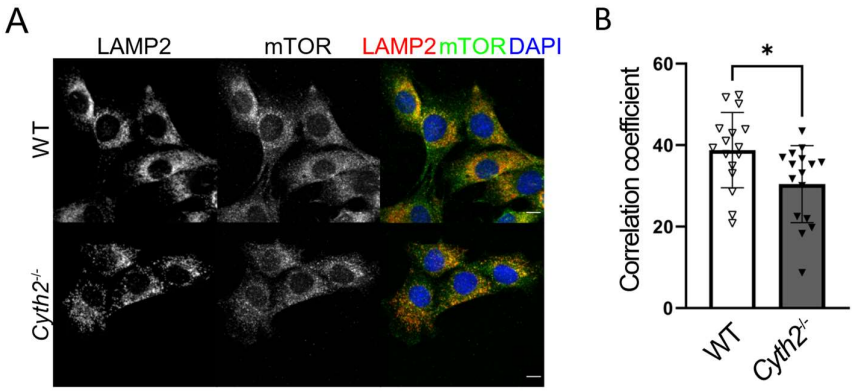

Figure 3.12: mTOR recruitment is hindered in *Cyth2*-deficient myoblasts
A) Representative immunofluorescence images of WT and *Cyth2*-deficient myoblasts stained for LAMP2 and mTOR (scale bar indicates 10 µm). **B)** Co-localization analysis of co-stainings for LAMP2 and mTOR in C2 myoblasts as in A) with Imaris 9. Bars represent mean Pearson's correlation ±SD pooled from four independent experiments including two pairs of WT and KO clones each. Each symbol represents a single z-stack analyzed (n=16). Statistical significance was tested by Student's unpaired t-test; *p < 0.05.

Taken together, imbalanced mTOR signaling was observed in *Cyth2*-deficient myoblasts compared to WT controls mainly affecting the signaling towards ULK1. Neither growth factor signaling via AKT nor energy homeostasis sensed by AMPK appeared to cause this effect. However, no major impact of the distorted mTOR signaling on cellular growth or metabolic state was detected in *Cyth2*-deficient myoblasts. Kinetic starvation and re-feeding experiments showed a comparable response of WT and KO myoblasts to the withdrawal of nutrients and growth factors. In contrast, a clear delay in the phosphorylation of ULK1 in KO cells after re-stimulation with medium was found, while the other mTOR targets were phosphorylated comparably to the WT condition. The hampered ULK1 phosphorylation was narrowed down to amino acid re-supplementation. Further, inhibition of ARF GTPases by interference with ARF GEFs hinders mTOR signaling.

Compared to BrefA treatment, cytohesin inhibition with SecinH3 showed some specificity towards mTOR-mediated ULK1 phosphorylation, in line with the observations on the genetic ablation of *Cyth2* in C2 myoblasts. Finally, a key process in the mTOR cascade, the recruitment of mTOR to the lysosomal surface, appeared to be impaired in *Cyth2*-deficient cells as the co-localization of mTOR and LAMP2 was reduced in *Cyth2* KO myoblasts.

3.3 Differential centrifugation reveals altered protein localizations in *Cyth2* knockout myoblasts

Recruitment of mTOR to lysosomes is mainly regulated by amino acid sensors, which are inactive when bound to specific amino acids and are released when amino acid levels drop [90, 91]. Subsequently, the respective sensor blocks the recruitment of mTOR to the lysosome, preventing mTOR activation and anabolism for the benefit of catabolic processes [85].

As neither FCS nor glucose re-feeding led to reduced ULK1 phosphorylation in *Cyth2*-deficient myoblasts (Fig. 3.7-9), the amino acid sensing may have triggered the observed reduction. Therefore, the localization of the mTOR signaling components and the upstream amino acid sensors was investigated, using a global approach described by Itzhak and colleagues [169], separating cellular organelles by multiple centrifugation steps with increasing rotation speed, and identifying the precipitated proteins per fraction by mass spectrometry (for more details see section 2.2.8). The protein distribution over these fractions was analyzed after two days standard culture conditions, as the decreased ULK1 phosphorylation was found exactly under these circumstances. Principal component analysis (PCA) of all samples showed a clear separation of the five cytoplasmic fractions and a separation of WT and *Cyth2* KO samples (Fig. 3.13A). A PCA of all proteins annotated with the compartment they are mainly found in [169] showed a separation of organelles, but proximity of marker proteins for a single compartment (Fig 3.13B). These results indicated that the experiment was carried out successfully and that no organelle was completely disrupted by the procedure or the loss of *Cyth2*.

3.3.1 ULK1 localization is altered in *Cyth2*-deficient myoblasts

Specifically, significant translocation of ULK1, mTOR signaling components, and amino acid sensing-associated proteins was analyzed. Although ULK1 was only detected in the first of two differential centrifugation experiments, Fig. 3.13C indicates a massive translocation of ULK1 from large protein complexes in WT myoblasts to the lysosomal compartment in *Cyth2*-deficient cells (Fig. 3.13C). Amino acid sensors, such as sestrins and the CASTOR1 complexes [90, 91], were not significantly relocated (data not shown). However, the mTOR-recruiting protein RAGC (Ras Related GTP Binding C) was found to be significantly relocated in *Cyth2*-deficient myoblasts (Fig. 3.13D). When searching for amino acid transporters, a significant translocation of SLC7A5, which was previously connected to amino acid sensing and mTOR signaling, from the plasma membrane compartment towards a large protein complex-containing compartment was observed (Fig. 3.13E; [92, 197, 198]). As SLC7A5 was identified as a marker for the plasma membrane, this latter finding may indicate general changes of the plasma membrane (Fig. 3.13E; [199]). The mean relative abundance of detected mTORC1 and mTORC2 complex components were only slightly and not significantly shifted from membranous compartments (3-, 5-, and 12-K fractions) towards large protein complexes (78-K fraction) in KO cells (Fig. 3.13F). However, both complexes remained distributed over all fractions (Fig. 3.13F).

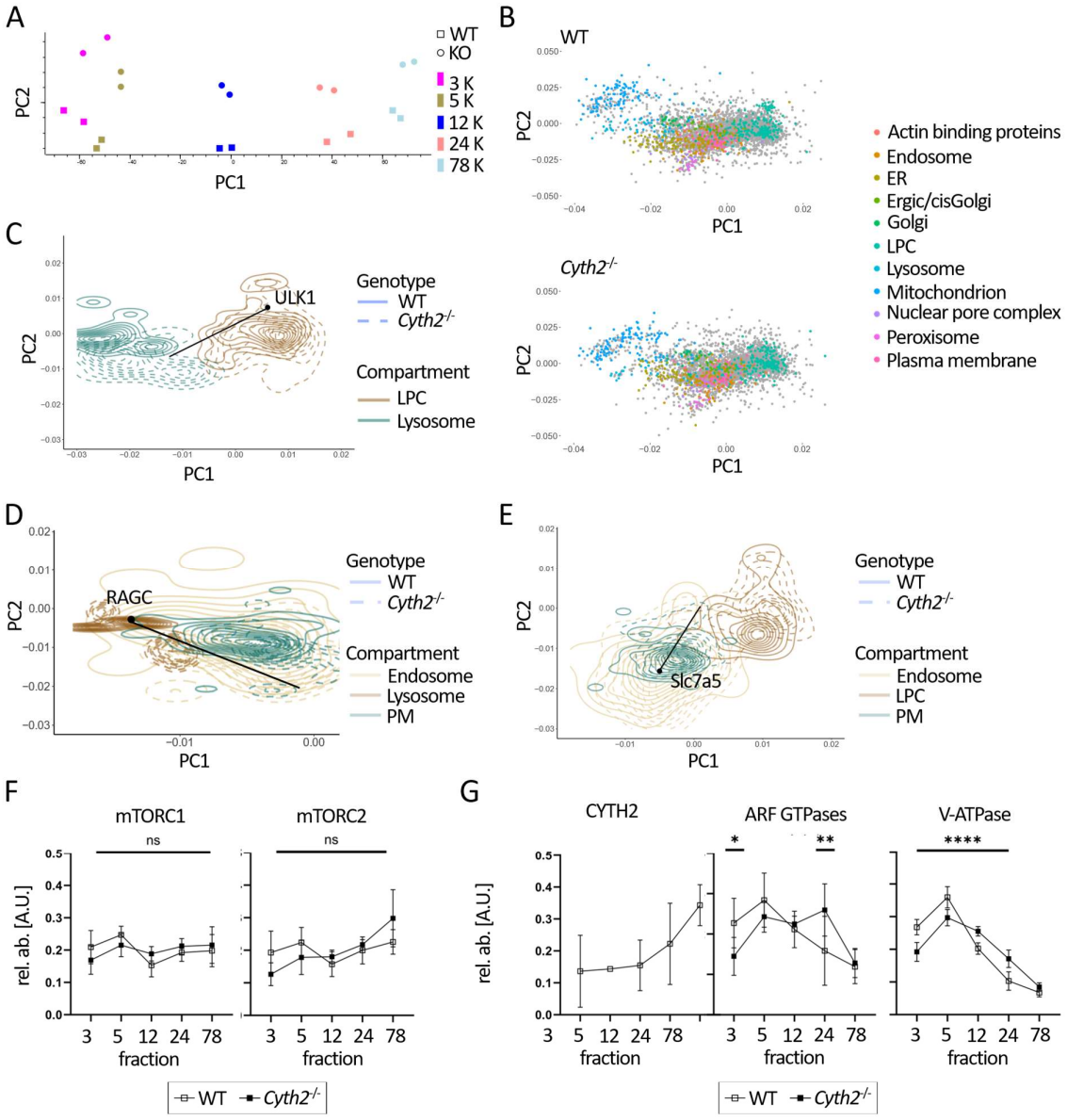

Figure 3.13: Differential centrifugation reveals protein delocalization of mTOR-associated structures and the endo-lysosomal V-ATPase

A) Principal component analysis (PCA) of samples after batch correction for the two independent experiments. **B)** Representative PCA of all proteins measured in WT (top) and *Cyth2*$^{-/-}$ (bottom) C2 myoblasts. Organellar marker proteins (according to Itzhak, 2016) are color-coded, remaining proteins are depicted as grey dots. **C-E)** PCA-based density plots of organellar markers as depicted, overlayed with PC1 and PC2 of C) ULK1, D) RAGC and E) SLC7A5. Black dots represent WT PCs, the end of the black line indicates the KO PCs. Data are taken from B). **F-G)** Mean relative abundancies of proteins comprised in F) the mTORC complexes and G) related to *Cyth2* and ARF GTPase signaling over the five cytoplasmic fractions of the differential centrifugation. Data are pooled from two experiments as listed in Table 1. Statistical significance was tested by 2way ANOVA (*$p < 0.05$, **$p < 0.01$, ns = not significant). Mass spectrometry and raw data analysis (A, B) was performed by Anushka Kudaliyanage and Dr. Sebastian Kallabis, AG Meissner

3.3.2 Analysis of the GTPase network suggests altered precipitation of endosomes

Another aim of the differential centrifugation approach was to study the localization of CYTH2 and its interaction partners. The experiments revealed the positioning of CYTH2 in all five fractions with the majority found to be in the 78-K fraction, where large, cytosolic protein complexes precipitate (Fig. 3.13G, left). In contrast, ARF GTPases in WT cells exhibited the highest abundance in fractions 3-, 5-, and 12-K, where membranous compartments like mitochondria, endosomes and lysosomes, and the Golgi apparatus precipitate (Fig. 3.13G, center). However, in *Cyth2*-deficient myoblasts, the mean relative abundance was significantly shifted towards fraction 24-K, indicating reduced recruitment of GTPases to the aforementioned compartments, or a physical change in size or density of these structures. Additionally, as CYTH2 interacts with the V-ATPase, the distribution of the V-ATPase subunits was analyzed. A minor but significant shift of these proteins from the lower g-force fractions towards the 12-K and 24-K fractions was found, pointing towards changes in the endo-lysosomal compartment (Fig. 3.13G, right).

3.3.3 Unbiased Fisher's exact test highlights Golgi enzymes

In addition to these observations, further changes in the organellar organization in C2 myoblasts after the depletion of *Cyth2* were evaluated. An unbiased approach was chosen: the data were combined from both differential centrifugation experiments, statistical analysis was performed to identify proteins, which had the highest overall change in relative abundance per fraction comparing WT and KO cells, and 177 significantly re-located proteins overlapping in both experiments were found (compare Table 2). Hierarchical clustering was performed and the proteins split up into two groups (Fig. 3.14A), which were then analyzed by Fisher's exact test for annotations overrepresented in these groups. Interestingly, the smaller cluster (Cluster 2) of 73 proteins contained many proteins associated with the GO term "vesicle" or "membrane part" (Fig. 3.14B), fitting the observations for ARF GTPases, V-ATPase, and the relocation of SLC7A5 (Fig. 3.13E, F). The bigger cluster (Cluster 1) showed the most enriched term, the Keyword "Signal-anchor" (KW-0735), counting proteins with a "single-pass transmembrane" domain, targeting

the respective protein to membranes of the ER [200]. A closer examination of Cluster 1 revealed many proteins of the glycosylation machinery of the Golgi apparatus (Table 2).

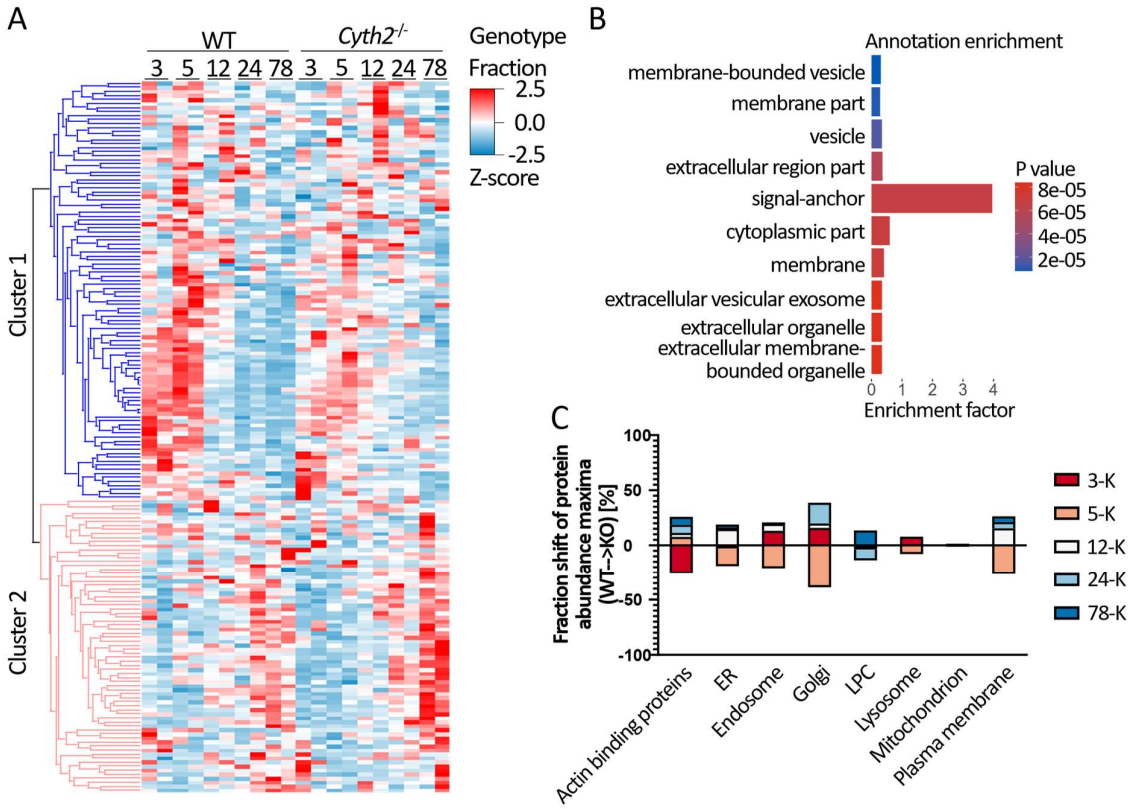

Figure 3.14: Fisher's exact test identifies Golgi structures to be changed by loss of *Cyth2*
A) Heatmap of significantly delocalized proteins overlapping in both differential centrifugation experiments, hierarchically clustered (Table 2). **B)** Gene ontology (GO) term enrichment analyzed for the proteins clustered in A) using Fisher's exact test. Enrichment was performed on biological process, cellular compartment, molecular function, Compartments and Keywords. **C)** Relative movement of organellar marker proteins (according to Itzhak 2016) from one differential centrifugation fraction to another in *Cyth2*-deficient myoblasts compared to WT cells (WT-KO). The number of marker proteins that had the highest relative abundance score in one fraction were counted per WT and KO, substracted from each other and divided by the total number of marker proteins for the respective organelle. No statistical test was performed. Mass spectrometry and raw data analysis (A) was performed by Anushka Kudaliyanage and Dr. Sebastian Kallabis, AG Meissner

Investigating further, the precipitation and main fraction of the marker proteins listed in [169] were analyzed. All mitochondrial markers had the highest relative abundance in the 3-K fraction, while lysosomal markers mainly precipitated in the 5-K fraction (data not shown). Other groups of organellar markers were not found in

a single fraction (data not shown). The difference between WT and KO cells was calculated. Fig. 3.14C shows, how markers were shifted from a specific fraction (negative values) into another (positive values) after the loss of *Cyth2* (Fig. 3.14C). This analysis revealed that the Golgi apparatus had the most marker proteins (~38%) shifting fractions between WT and KO cells compared to other compartments. Most of the Golgi marker proteins came from the 5-K fraction and switched to the 24-K fraction, even though some proteins also landed in the 3-K fraction. Additionally, other compartments were affected as well such as the endosomal (~19% of marker proteins) and plasma (~26% of marker proteins) membrane compartments. Of note, the lysosomal and mitochondrial compartments were only mildly or not at all affected (~8% and ~1% of marker proteins, respectively).

Taken together, differential centrifugation separated organelles from each other and subsequent MS analysis revealed altered precipitation behavior of specific proteins and organellar compartments in *Cyth2*-deficient cells compared to WT controls. Translocated ULK1, RAGC, and SLC7A5 might explain the decrease in pULK1(S757) levels described above (Fig. 3.4, 3.6, 3.9), while the redistribution of ARF GTPases and the V-ATPase indicate changes in the endosomal compartment. Further, unbiased analysis of significantly re-distributed proteins pointed towards the Golgi apparatus.

3.4 *Cyth2* deficiency distorts the endosomal network

Besides an altered distribution of ULK1, organellar maps indicated a change in endosomal precipitation. However, organellar maps only point towards certain proteins or organelles, but do not provide specific information about modifications of single proteins or their host organelles. Therefore, the endosomal network was studied in more detail.

3.4.1 Loss of *Cyth2* increases the number of endosomal structures and lysosomes in C2 myoblasts

To get more insight into the altered behavior of endosomes in *Cyth2*-deficient myoblasts, immunofluorescence staining for RAB5 as a marker of early endosomes was performed [12, 66]. RAB5 particles were analyzed in 3D reconstitutions of C2 myoblasts after two days of standard culture (Fig. 3.15A). Increased numbers of RAB5-positive structures were found in *Cyth2* KO cells (339±114 vesicles/cell) compared to WT controls (295±99 vesicles/cell; Fig. 3.15B). However, the particles analyzed were indistinguishable between WT and KO regarding their diameter (Fig. 3.15C) or the RAB5 maximal intensity (Fig. 3.15D).

As RAB5-positive early endosomes lose RAB5 and acquire RAB7 during conversion to late endosomes, WT and *Cyth2*-deficient C2 myoblasts were further stained for RAB7 (Fig. 3.15E; [12, 66]) to investigate, whether the increased numbers of early endosomes propagated into the late endosomal compartment. As observed for RAB5, the numbers of RAB7-positive structures were also significantly increased in *Cyth2*-deficient myoblasts (WT: 187±64 vesicles/cell, KO: 228±49 vesicles/cell; Fig. 3.15F). Comparable to RAB5, vesicle diameter and maximal fluorescent intensity of RAB7-positive structures were indistinguishable between WT and KO cells (Fig. 3.15G, H).

As cellular material from the late endosomal compartment is fed into the lysosomes for degradation, C2 cells were also stained for LAMP2 as a lysosomal marker (Fig. 3.15I). Similar to RAB5 and RAB7, an increase in LAMP2-positive particle numbers in *Cyth2*-deficient myoblasts (571±172 vesicles/cell) was observed compared to WT control cells (436±173 vesicles/cell; Fig. 3.15J). Further, there was again no difference in vesicle size or maximal fluorescence intensity between WT and KO cells detectable, as it was found before for RAB5 and RAB7 (Fig. 3.15K, L).

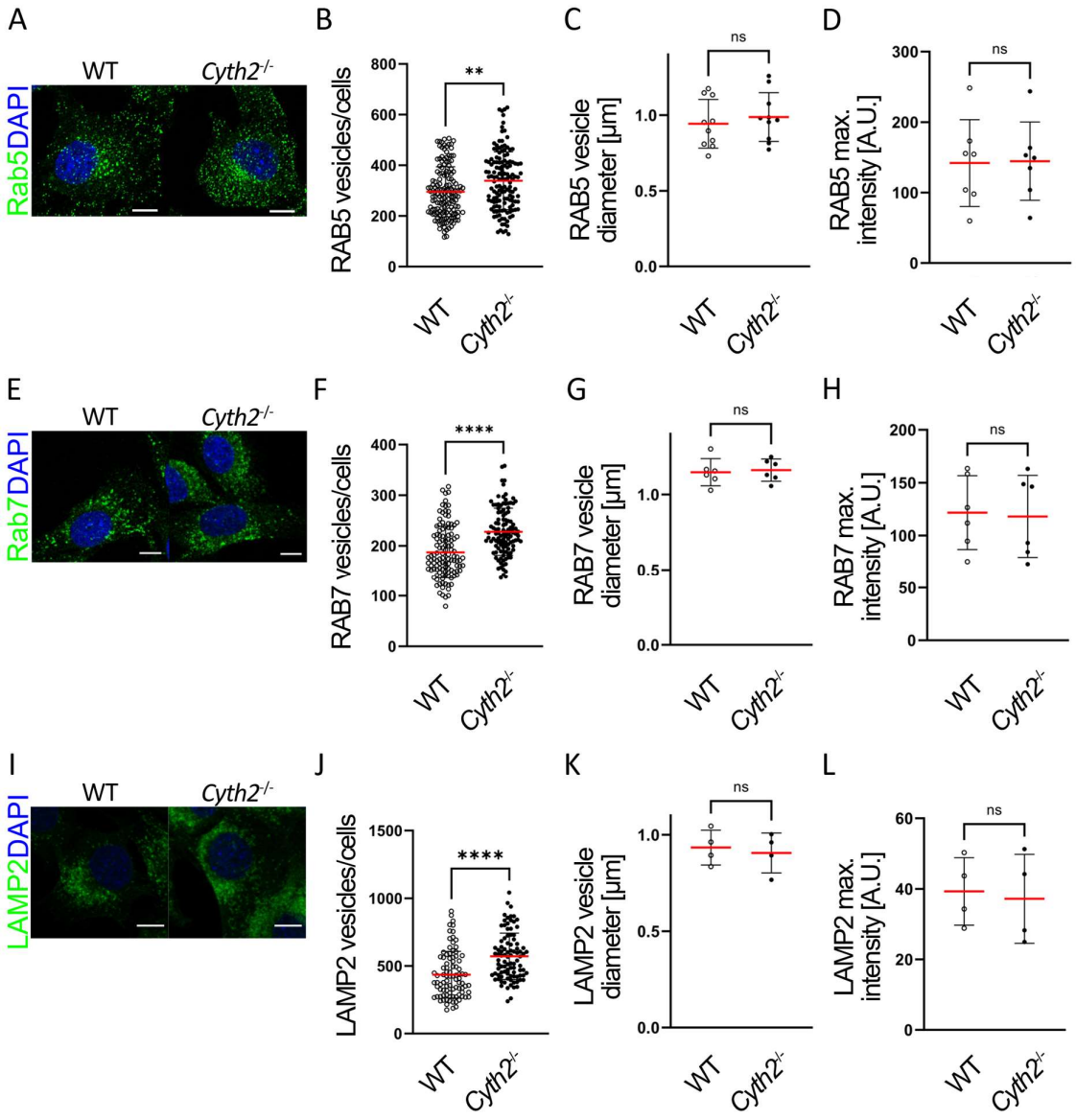

Figure 3.15: The endosomal compartment is fine-tuned by *Cyth2*
Immunofluorescence analysis of **A-D)** RAB5, **E-H)** RAB7, and **I-L)** LAMP2 in WT and *Cyth2* knockout myoblasts using Imaris 9. Data include representative images (A, E, I; scale bar indicates 10 µm), the number of RAB- or LAMP2-positive spots per cell (B, F, J), the average spot diameter (C, G, K), and the averaged maximal spot intensity (D, H, L). Data were pooled from seven (A-D), six (E-H) and four (I-L) independent experiments; each dot represents a single cell analyzed (B, F, J) or the average of a single experiment (C, D, G, H, K, L); red lines indicate means ±SD (total number of cells included in the analysis for WT and KO, were 154 and 151 for RAB5, 119 and 113 for RAB7, 91 and 94 for LAMP2). Statistical significance was tested by Mann-Whitney or paired t-test (*p < 0.05, **p < 0.01, ***p < 0.001, ****p < 0.0001, ns = not significant).

3.4.2 *Cyth2* regulating the endo-lysosomal compartment is partially conserved over species

To validate these findings in C2 myoblasts (Fig. 3.15) additional cell models were used and RAB5- and RAB7-positive structures analyzed in A7r5 (rat smooth muscle) cells, HEK293T (human embryonal kidney) cells, mouse embryonic fibroblasts (MEFs), and MuTu1940 dendritic cells (MuTu DCs; murine), covering rat and human as additional species as well as different cell types (Fig. 3.16). Using the CRISPR/Cas9 approach *Cyth2* KO cells were generated (see section 2.2.7) and depletion of *Cyth2* was validated by Western Blot (Fig. 3.16A-D). Of note, A7r5 cells were analyzed as bulk populations, but the loss of CYTH2 was substantial (detected by Western Blot, Fig. 3.16A).

Rab5-positive early endosome counts were significantly elevated in *Cyth2*-deficient A7r5 cells, MEFs, and MuTu DCs compared to WT controls, while no difference was observed in HEK293T cells (Fig. 3.16E-H). For RAB7, significantly increased numbers of late endosomal structures were found in A7r5 and HEK293T KO cells, but no significant difference was observed between WT and *Cyth2*-deficient MEFs (Fig. 3.16I-K). *Cyth2*-deficient MuTu DCs even showed a significant reduction in late endosomes (Fig. 3.16L). To exclude alterations in cell size as the reason for changed numbers of early and late endosomes, cell spreading area and cellular volume were measured by immunofluorescence as well. No significant change in cell size was observed for A7r5 cells, MEFs and MuTu DCs. However, the *Cyth2*-deficient HEK293T cells were slightly but significantly larger than WT control cells (Fig. 3.16M-P). However, the calculated ratio of RAB7 vesicles per cell volume was still significantly increased in HEK293T *Cyth2* KO cells compared to WT controls, indicating that cell size alone could not explain this phenotype (data not shown).

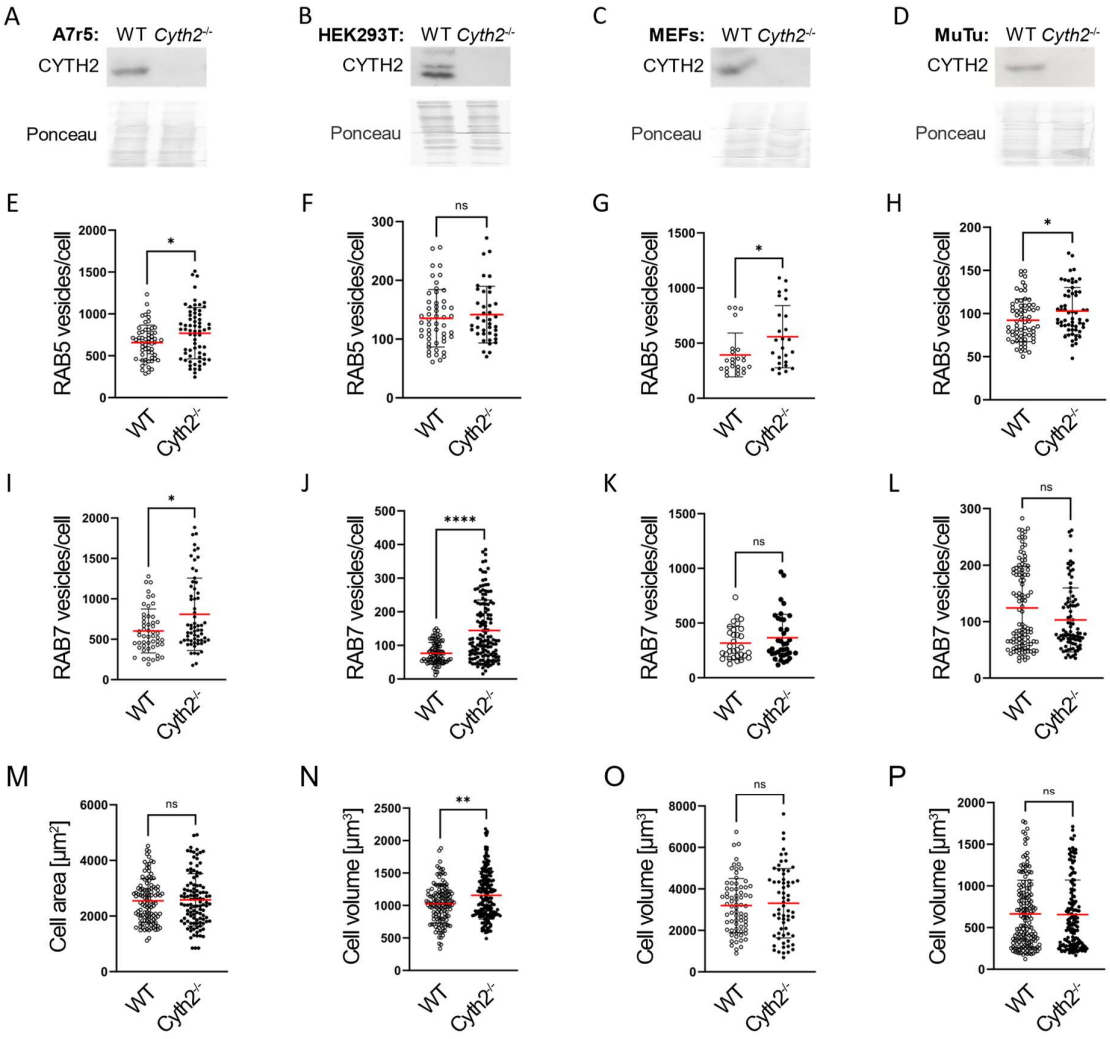

Figure 3.16: *Cyth2* control over the endosomal compartment seems partially conserved over cell types and species.
A-D) Representative Western Blots of CYTH2 in WT and *Cyth2* knockout A) A7r5 (rat smooth muscle) cells, B) HEK293T (human embryonic kidney) cells, C) murine embryonic fibroblasts (MEFs), and D) MuTu (murine dendritic) cells including Ponceau staining as a loading control. **E-P)** Immunofluorescence analysis of the endosomal compartment in WT and *Cyth2*-deficient cells as in A-D) using Imaris 9. E-H) number of RAB5-positive spots per cell, I-L) number of RAB7-positive spots per cell, and M-P) cell area or volume as a measurement of cell size in A7r5 cells (E, I, M), HEK293T cells (F, J, N), MEFs (G, K, O), and MuTu cells (H, L, P). Data were pooled from independent experiments ($n \geq 3$) including two images per condition each (cells analyzed: $n \geq 24$); each dot represents a single cell analyzed; red lines indicate means ±SD. Statistical significance was tested by Mann-Whitney or paired t-test (*$p < 0.05$, **$p < 0.01$, ***$p < 0.001$, ****$p < 0.0001$, ns = not significant).

3.4.3 Overexpression of a single *Cyth2* isoform does not rescue the endosome multiplication

As explained before (see section 1.6.1), *Cyth2* is expressed in two isoforms, which differ in a single glycine residue in the PH domain (2G and 3G) and thereby in the binding affinity to PtdInsPs. The next aim was, to investigate which of the two isoforms of *Cyth2* is involved in the regulation of RAB5- and RAB7-positive endosomal structures. To do so, Sanger sequencing on cDNA samples from C2 myoblasts, HEK293T cells, and A7r5 cells was performed followed by tide-analysis to estimate the proportion of the *Cyth2*-2G and -3G isoform expressed in these cells (Fig. 3.17A). All three cell lines expressed *Cyth2* with 30-40% in the 2G-isoform and 60-70% in the 3G-isoform. This result could not clarify, which of the two isoforms would be regulating RAB5 and RAB7.

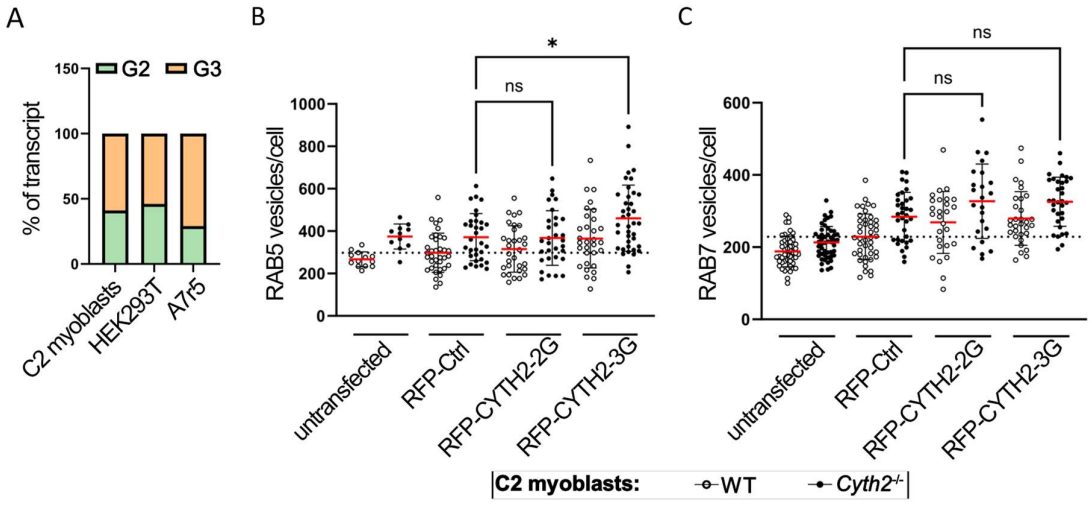

Figure 3.17: *Cyth2* overexpression does not rescue increased endosomal counts in *Cyth2*-depleted myoblasts.
A) Tide analysis of *Cyth2* isoform expression in WT C2 myoblasts, HEK293T and A7r5 cells performed on Sanger-sequenced cDNA samples. Bars represent 100% *Cyth2* expression (n=1). **B-C)** Immunofluorescence analysis of B) RAB5- and C) RAB7-positive spot counts per cell in WT and *Cyth2*-deficient myoblasts transfected with CYTH2-RFP constructs and respective controls analyzed by Imaris 9 as before. Red lines represent average values ±SD pooled from independent experiments (n≥3); each dot indicates a single cell analyzed (n≥11). Statistical significance was tested by 2way-ANOVA (*p < 0.05, ns = not significant).

Knowing that both isoforms are expressed in C2, HEK293T and A7r5 cells, it remains elusive which of the two *Cyth2*-isoforms would regulate RAB5 and RAB7. Therefore, it is necessary to rescue the observed RAB5 and RAB7 vesicle increase with both WT-*Cyth2* isoforms. WT and *Cyth2* KO C2 myoblasts were transfected with

expression vectors for CYTH2-RFP fusion proteins and stained either for RAB5 or RAB7. Immunofluorescence analysis was performed in cells with moderate RFP expression (evaluated ad hoc, not systematically). Untransfected and RFP-only-transfected cells served as controls.

Both controls showed amounts of RAB5 endosomes as observed before, with increased numbers in *Cyth2*-deficient myoblasts (RFP-Ctrl; WT: 298±92.31 vesicles/cell, KO: 371.4±111.1 vesicles/cell; 24.6% increase; Fig. 3.17B). Interestingly, overexpression of *Cyth2*-2G did not affect the numbers of RAB5-positive vesicles compared to the respective control cells. The elevated RAB5 spot counts in KO cells remained compared to WT cells overexpressing *Cyth2*-2G. In contrast, both WT and KO cells transfected with *Cyth2*-3G showed increased RAB5 endosome counts compared to untransfected cells and RFP controls. However, the difference between WT and KO myoblasts remained, the *Cyth2*-deficient cells still had higher numbers of RAB5-positive structures compared to WT cells transfected with the 3G-isoform (WT: 364.8±139.0 vesicles/cell, KO: 460.7±156.0 vesicles/cell; 26.3% increase; Fig. 3.17B).

Analyzing RAB7 in *Cyth2*-overexpressing myoblasts revealed a similar but even more difficult picture: While untransfected control cells showed late endosome counts comparable to the experiments before with higher numbers of RAB7-positive structures in CYTH2-deficient myoblasts (Fig. 3.17C), transfection of the RFP control vector and both CYTH2-RFP expression vectors increased the numbers of late endosomes in both WT and KO. Nevertheless, in all three conditions higher numbers of RAB7 endosomes were found in KO cells compared to the respective WT control cells. Due to the increased numbers of RAB7 endosomes in cells overexpressing RFP alone, these results need to be interpreted with caution (Fig. 3.17C).

3.4.4 *Cyth2* blockage with SecinH3 partially pheno-copies the knockout of the gene in the endosomal compartment

SecinH3 was utilized for chemical interference with the endosomal system as another means of CYTH2 inhibition besides the genetic approach. To this end, WT and *Cyth2* KO myoblasts were treated with SecinH3 or BrefA to inhibit ARF

activation, stained for RAB5 or RAB7, and endosomal structures were examined via immunofluorescence analysis (Fig. 3.18). The RAB5 vesicle count was significantly increased in WT myoblasts treated with SecinH3 (DMSO: 283.5±65.08 vesicles/cell, SecinH3: 375.3±115.4 vesicles/cell), but only a minor increase was observed in *Cyth2*-deficient cells (Fig. 3.18A). By contrast, BrefA caused a reduction of early endosome counts in both WT (245.1±76.09 vesicles/cell; not significant) and KO myoblasts (249.6±98.68 vesicles/cell). Treatment of WT cells with SecinH3 caused a minor, non-significant increase in RAB7 spot numbers compared to DMSO controls, while in *Cyth2*-deficient cells SecinH3 lead to a significant loss of RAB7-positive structures (DMSO: 257.2±67,87 vesicles/cell, SecinH3: 224.2±34.65 vesicles/cell). RAB7 vesicle numbers were unaffected by BrefA in WT and KO cells (Fig. 3.18B). Furthermore, the possibility that treatment of C2 cells with

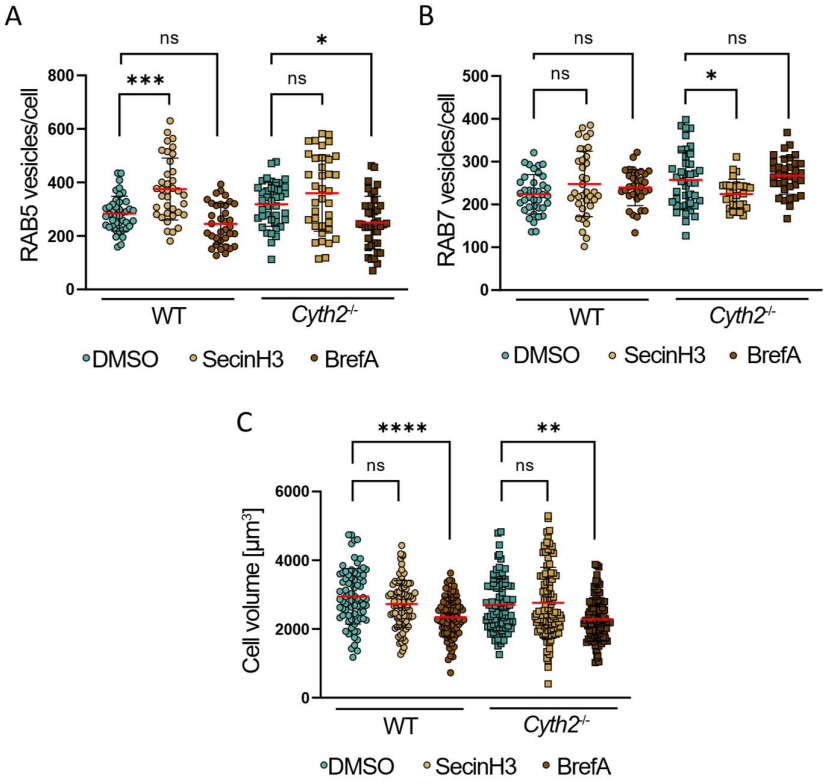

Figure 3.18: SecinH3 inhibition pheno-copies increased early endosome numbers in C2 cells A-C) Immunofluorescence analysis of A) RAB5- and B) RAB7-positive spots, and C) cell volume in WT and *Cyth2*-deficient myoblasts treated with SecinH3 (50 mM) or BrefA (5 µg/ml) for four hours with Imaris 9 as before (DMSO served as a control). Red lines represent means ±SD from independent experiments (n≥3); each symbol represents one cell analyzed (n=n≥29). Statistical significance was tested by one-way ANOVA per genotype (*p < 0.05, **p < 0.01, ***p < 0.001, ****p < 0.0001, ns = not significant).

SecinH3 or BrefA could alter cell size the cellular volume was evaluated. WT and *Cyth2*-deficient myoblasts had comparable cell volumes and did not change in size upon treatment with SecinH3 (Fig. 3.18C). BrefA, however, caused a significant volume reduction in both WT and KO cells, which might explain the minor reduction in RAB5-positive early endosomes upon BrefA treatment (Fig. 3.18A, C).

In summary, loss of *Cyth2* caused increased numbers of early and/or late endosomes in a variety of cell types and conserved over three species (mouse, human, rat). However, *Cyth2* appeared to affect the early and late endosomal compartments to a variable extent in different cell types. Overexpression of a single isoform of *Cyth2* could not reverse this effect, indicating that neither the 2G nor the 3G-isoform alone could rescue the observed phenotype. While SecinH3 phenocopied the loss of *Cyth2* regarding the numbers of early endosomes, BrefA reduced the number of RAB5-positive endosomes. RAB7-positive late endosomes were not significantly affected by SecinH3 or BrefA.

3.5 *Cyth2* is involved in structural and functional regulation of the Golgi apparatus

Besides the findings about ULK1 and the endosomal compartment, unbiased analysis of the organellar maps revealed changed precipitation within the Golgi compartment (Fig. 3.14E). Thus, the impact of *Cyth2* on Golgi structure and function was analyzed.

3.5.1 *Cyth2* deficiency reduces the volume of the Golgi compartment

Immunofluorescence analysis of the Golgi apparatus in C2 myoblasts was performed after two days of standard culture conditions. As a marker protein, golgin-97 (also Golga1) was chosen, which was reported to be located in the medial and trans-Golgi (Fig. 3.19). The size of the Golgi apparatus was smaller in *Cyth2*-deficient myoblasts, reflected by a significantly decreased Golgi volume (Fig. 3.19A, B). Similar results were obtained from two pairs of independent WT and KO clones (WT1: 28.06±7.6 μm^3, WT2: 27.38±8.6 μm^3, KO1: 17.19±6.2 μm^3, KO2:

21.12±10.3 µm^3), and the reduced volume was also reflected by a significantly smaller Golgi surface area in *Cyth2* KO cells compared to the WT controls (Fig. 3.19C). Interestingly, the maximal fluorescence intensity of Golgi structures in both *Cyth2*-deficient clones was significantly lower compared to WT cells (Fig. 3.19D). A more detailed look on Golgi morphology revealed a minor increase in separated objects per Golgi apparatus in KO myoblasts, indicating changes such as an increased number of stacks or transport vesicles not connected to each other (Fig. 3.19E). Additionally, despite a comparable sphericity of Golgis in WT and KO myoblasts, Golgi structures in KO cells had significantly higher prolate ellipticity opposing decreased oblate ellipticity (Fig. 3.19F-H; for more details see 2.2.4.2). These parameters basically describe the KO Golgi structure as slightly more elongated and less disk-shaped compared to WT Golgis, while the surface-to-volume ratio remains similar.

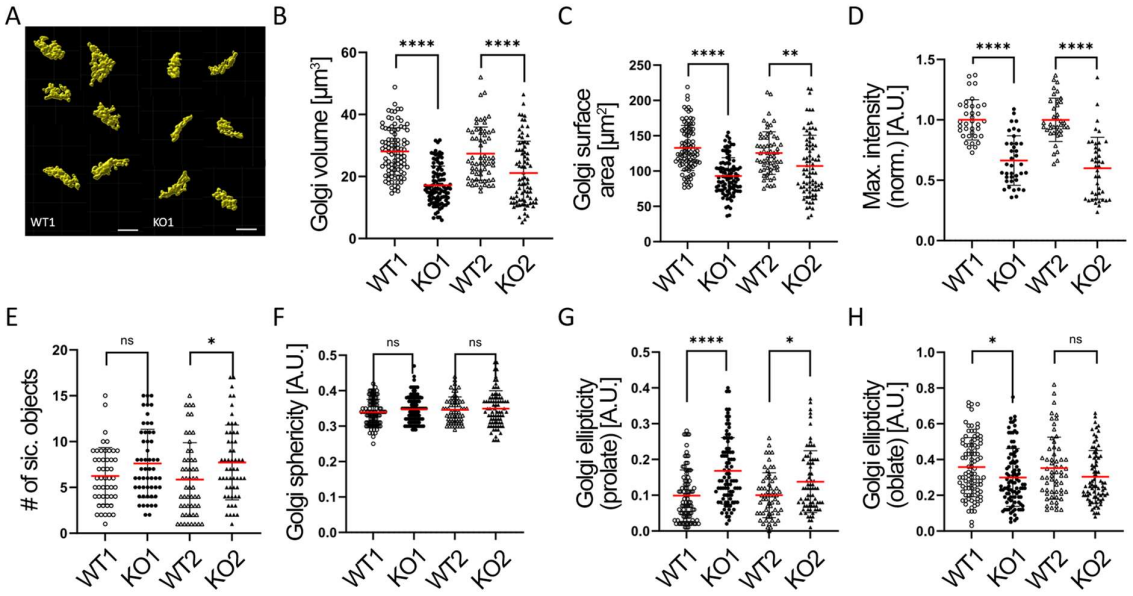

Figure 3.19: *Cyth2* controls Golgi size in muscle precursor cells
A-H) Immunofluorescence analysis of the Golgi structure in WT and *Cyth2* KO C2 myoblasts with Imaris 9. Two pairs of myoblasts clones were stained for golgin-97 and z-stack images acquired, used for 3D re-construction of the Golgi apparatus (scale bar represents 7 µm). A) Representative 3D models of Golgi structures in WT and KO myoblasts. B-H) Analysis of B) Golgi volume and C) surface area, D) golgin-97 maximal intensity, E) number of disconnected objects, F) Golgi sphericity, and G) prolate and H) oblate ellipticity. Data were pooled from independent experiments (n≥5); red lines indicate means ±SD; each dot represents one Golgi apparatus analyzed (n≥36). Statistical significance was tested by Mann-Whitney test per pair of clones (*p < 0.05, **p < 0.01, ***p < 0.001, ****p < 0.0001, ns = not significant).

3.5.2 Golgi volume control by *Cyth2* appears cell type-specific but conserved over mammalian species

As before for RAB5 and RAB7, the Golgi observations in C2 myoblasts upon loss of *Cyth2* were validated in other cell systems. Rat A7r5 cells, human HEK293T cells, murine MEFs, and MuTu DCs were stained for golgin-97 and immunofluorescence analysis was performed. The focus of the following analysis was on Golgi size and golgin-97 fluorescence intensity (Fig. 3.20).

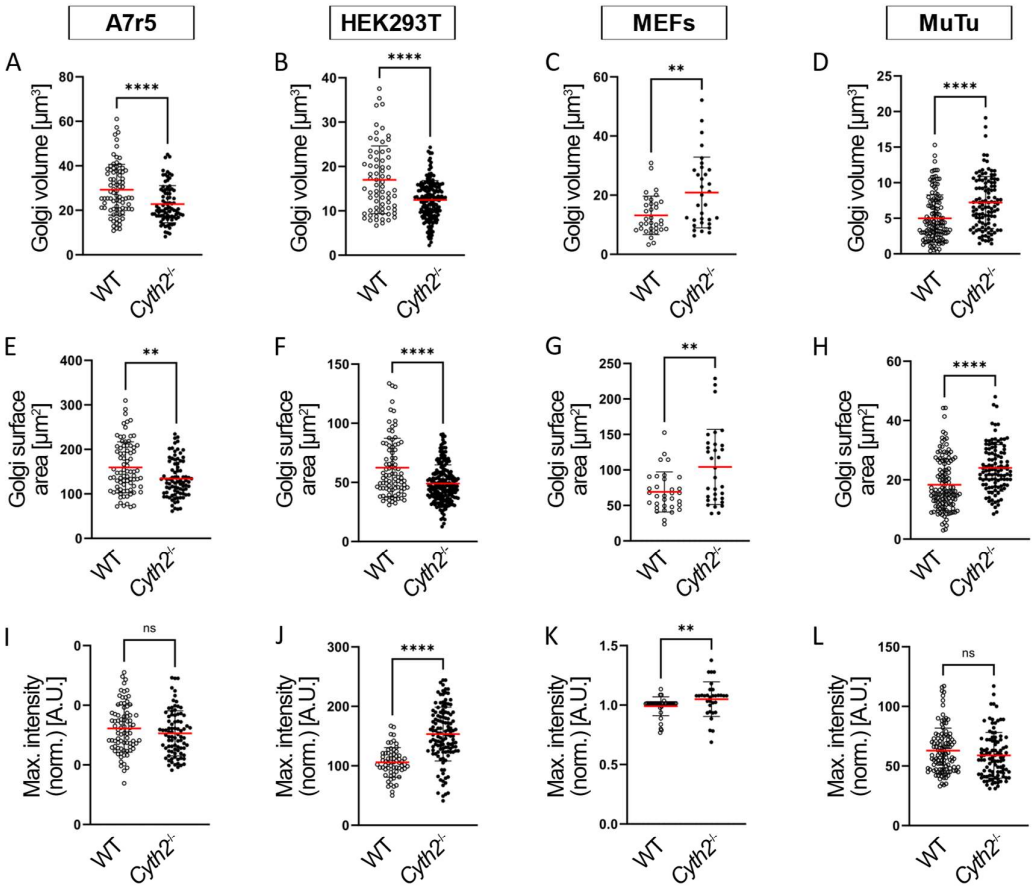

Figure 3.20: *Cyth2* balancing Golgi size is conserved over mammalian species
A-L) Immunofluorescence analysis of the Golgi structure in WT and *Cyth2* KO A7r5 cells (A, E, I), HEK293T cells (B, F, J), MEFs (C, G, K), and MuTu cells (D, H, L) with Imaris 9 based on Golgin-97 stainings as before. Analysis of A-D) Golgi volume, E-H) Golgi surface area, and I-L) Golgin-97 maximal intensity. Data were pooled from independent experiments (n≥3); red lines indicate average ±SD; each dot represents one Golgi apparatus analyzed (n≥32); max. intensity data for MEFs were normalized to WT cells). Statistical significance was tested by Mann-Whitney test per pair of clones (*p < 0.05, **p < 0.01, ***p < 0.001, ****p < 0.0001, ns = not significant).

In A7r5 and HEK293T cells, depletion of *Cyth2* caused a significant reduction in Golgi volume, comparable to the reduction in C2 myoblasts (Fig. 3.20A, B). However, in MEFs and MuTu DCs a significantly increased Golgi volume was observed in *Cyth2*-depleted cells compared to the WT control (Fig. 3.20C, D). Accordingly, KO of *Cyth2* lead to a smaller Golgi surface area in A7r5 and HEK293T cells, while it was enlarged in MEFs and MuTu DCs (Fig. 3.20E-H). Based on the C2 myoblasts results showing decreased Golgi volume and golgin-97 signal, one could assume a technical correlation between measured Golgi size and maximal fluorescence intensity. This assumption is negligible as both A7r5 and MuTu DCs showed no difference in golgin-97 maximal fluorescence intensity despite the *Cyth2*-dependent differences in size (Fig. 3.20I, L). In HEK293T cells, while Golgi size was reduced in the KO condition, the fluorescence intensity was significantly increased (Fig. 3.20J). Only in MEFs and C2 cells, Golgi volume and surface area were correlated with fluorescence intensity of golgin-97 (Fig. 3.20C, G, K; Fig. 3.19B-D).

3.5.3 *Cyth2*-3G rescues the Golgi diminution in an ARF-independent manner

Overexpression experiments were performed, to identify the *Cyth2* isoform responsible for Golgi size regulation (Fig. 3.21). CYTH2-RFP fusion proteins were overexpressed in WT and *Cyth2* KO myoblasts, the cells stained for golgin-97 and immunofluorescence analysis was performed. RFP-only cells served as controls. Additionally, *Cyth2* mutants were included in these experiments: one GEF-inactive mutant (E|K) to test the requirement for ARF activation for *Cyth2* to affect Golgi size, and one coiled-coil-deleted mutant (Δcc) to investigate the involvement of additional protein-protein interactions.

RFP-expressing controls showed the same Golgi size reduction of *Cyth2* KO cells as observed before (Fig. 3.21A, B). Overexpression of neither WT *Cyth2*-2G nor its GEF mutant *Cyth2*-2G-E|K altered the volume of the Golgi apparatus significantly and the Golgi volume remained reduced in *Cyth2* KO myoblasts compared to the respective WT controls (Fig. 3.21A). Surprisingly, the coiled-coil mutant *Cyth2*-2G-Δcc significantly reduced the Golgi volume in WT cells compared

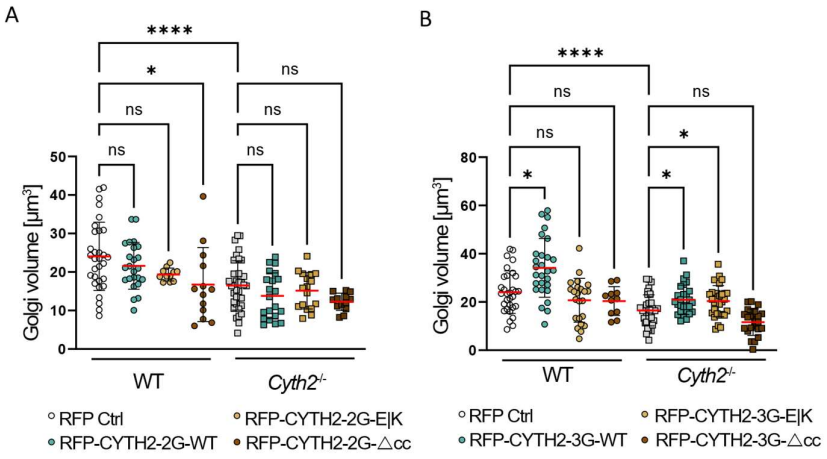

Figure 3.21: *Cyth2* overexpression rescues decreased Golgi volume in an isoform-specific manner
A-B) Immunofluorescence analysis of the Golgi structure in WT and *Cyth2* KO myoblasts overexpressing *Cyth2* with Imaris 9 based on Golgin-97 stainings as before. WT and KO myoblasts were transfected with RFP-coupled WT, GEF-mutant (E|K) and coiled-coil mutant (Δcc) *Cyth2* in the A) 2G-isoform and B) 3G-isoform and compared to RFP-expressing cells. Red lines indicate average Golgi volumes ±SD pooled from independent experiments (n≥3); each symbol represents a Golgi apparatus analyzed (n≥11). Statistical significance was tested by 2way-ANOVA (*p < 0.05, ****p < 0.0001, ns = not significant).

to the RFP control, and there was a similar tendency in *Cyth2*-deficient myoblasts (Fig. 3.21A).

In contrast, both WT and KO cells expressing WT *Cyth2*-3G showed an increased Golgi volume (Fig. 3.21B). In KO myoblasts the size of the Golgi was rescued (RFP Ctrl: 16.52±6.4 µm^3, *Cyth2*-3G: 20.89±6.1 µm^3), almost reaching the volume of WT controls. Moreover, in WT cells the expression of WT *Cyth2*-3G (34.13±12.2 µm^3) significantly increased the Golgi volume compared to RFP-expressing cells (24.06±8.9 µm^3). While in WT cells Golgi volumes were comparable between RFP control and *Cyth2*-3G-E|K mutant-expressing cells, in *Cyth2* KO myoblasts the GEF-inactive mutant also rescued Golgi size and restored the organelle's volume comparable to the GEF-active WT form (20.33±6.4 µm^3). In both WT and KO cells overexpression of the coiled-coil mutant of *Cyth2*-3G had no significant effect on Golgi size (Fig. 3.21B).

3.5.4 SecinH3 treatment supports the hypothesis of *Cyth2* regulating Golgi size independent from ARF GTPases

The next aim was to verify these findings using the cytohesin inhibitor SecinH3 (Fig. 3.22). BrefA served as a positive control, as it is a potent Golgi inhibitor and was reported to disrupt Golgi structure and function [196, 201]. Cells were treated with the inhibitors, fixed, and stained for golgin-97, followed immunofluorescence analysis. Indeed, BrefA-treated cells contained almost no golgin-97-positive structure, neither WT nor KO cells. The signal was rather weak and dispersed in the cells, proving BrefA to be effective as described (Fig. 3.22A).

In contrast, treatment of C2 myoblasts with SecinH3 did not affect the Golgi volume compared to DMSO controls. Instead, there was even a small but significant increase in Golgi size in *Cyth2*-deficient cells compared to the respective DMSO control (Fig. 3.22A). Of note, comparing WT and *Cyth2* KO DMSO controls showed no significant volume difference for the Golgi apparatus as described before (Fig. 3.19). So, interpretation of these results might be challenging due to the effect of DMSO as a solvent of SecinH3.

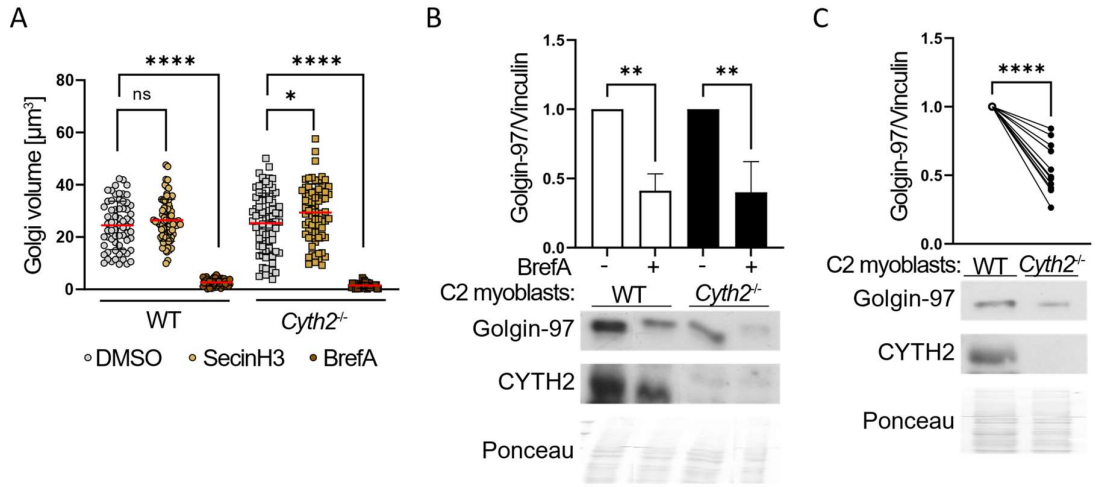

Figure 3.22: SecinH3 does not decrease Golgi volume in C2 myobasts
A) Immunofluorescence analysis of Golgi volume of WT and KO cells treated with DMSO, SecinH3 (50 mM) or BrefA (5 µg/ml) for four hours with Imaris 9 as before. Data were pooled from five independent experiments; red lines indicate average Golgi volume ±SD, each symbol represents an individual Golgi stack analyzed (n≥29). **B)** Western Blot analysis of Golgin-97 in WT and *Cyth2*-deficient myoblasts treated with BrefA (5 µg/ml) for four hours. Data were normalized to total protein as determined by Ponceau staining and further normalized to the respective DMSO control. Bars represent mean normalized intensities +SD (n=3). **C)** Western Blot analysis of Golgin-97 in WT and *Cyth2* knockout myoblasts after two days standard culture conditions. Data were normalized to total protein as determined by Ponceau staining and further normalized to the WT condition (n=13). Statistical significance was tested by one-way ANOVA per genotype, 2way-ANOVA and paired t-test (*p < 0.05, **p < 0.01, ****p < 0.0001, ns = not significant).

Golgi structure was correlated with the expression of Golgi structural components before [42, 46]. The disruption of Golgi structure by BrefA was accompanied by a significant loss of golgin-97 protein in C2 myoblasts, both in WT and *Cyth2*-deficient cells (Fig. 3.22B). Compared to the DMSO control, cells of both genotypes lost about 60% of the protein. Interestingly, looking at the DMSO controls, there was also a reduction of golgin-97 in *Cyth2* KO myoblasts compared to the respective WT control (Fig. 3.22B). This finding was validated by Western Blot analysis of C2 myoblasts after two days of standard culture conditions. A significant reduction of golgin-97 protein was observed in *Cyth2* KO cells compared to their WT counterparts (Fig. 3.22C).

3.5.5 *Cyth2* deficiency-dependent reduced Golgi size affects protein glycosylation and the secretory apparatus

In C2 myoblasts, A7r5, and HEK293T cells the volume of the Golgi apparatus was found to be reduced after the genetic depletion of *Cyth2*. Thus, the functional consequences of these morphological changes were investigated. Therefore, the glycosylation of surface proteins on WT and KO C2 myoblasts was analyzed, staining cells with fluorophore-coupled lectins followed by flow cytometry (Fig. 3.23A). An array of lectins was tested to cover a broad range of glycosylation patterns. However, some of the tested lectins were almost undetectable on C2 myoblasts, hence only Concanavalin A (ConA), peanut agglutinin (PNA) and wheat germ agglutinin (WGA) are depicted here. While ConA and WGA intensities were indistinguishable between WT and *Cyth2*-deficient cells, ~30% lower PNA staining intensity revealed significantly lower levels of N-acetylgalactosamine (GalNAc)-type O-glycosylation on KO cells compared to WT controls (Fig. 3.23A). BrefA served as a positive control and reduced the binding of all three lectins in WT cells, interestingly to a similar degree (~25%) as the depletion of *Cyth2* did for PNA. Based on the literature, the N-Acetylgalactosamine (GalNAc) O-glycosylation core is the product of the terminal reaction of C1GALT1 (Core 1 Synthase, Glycoprotein-N-Acetylgalactosamine 3-Beta-Galactosyltransferase 1) and its essential chaperone C1GALT1C1 (C1GALT1 Specific Chaperone 1; Fig. 3.23B; [202, 203]). The results from the differential centrifugation experiments were therefore consulted once more

and both proteins and an additional interaction partner, MGAT1 (Alpha-1,3-Mannosyl-Glycoprotein 2-Beta-N-Acetylglucosaminyltransferase), were significantly translocated in both experiments (Fig. 3.23C). However, the three proteins remain within the Golgi compartment, as the density plot for Golgi marker proteins showed a clear shift of the complete organelle along the movement of the C1GALT1, C1GALT1C1, and MGAT1 axis (Fig. 3.23C).

As many glycosylated proteins are not only transported to the surface of cells but also secreted to the extracellular space, plasma samples of WT and *Cyth2*-deficient neonatal mice were analyzed by mass spectrometry. Among all 3154 measured proteins, 1D-enrichment analysis of GO terms highlighted the terms “Secreted” (KW-0964) and “Glycoprotein” (KW-0325), confirmed by Fisher’s exact test for down-regulated proteins (Fig. 3.23D). And indeed, while statistical analysis found only a small number of proteins significantly up- or downregulated (2 and 2, respectively) in plasma of *Cyth2*-deficient animals, the majority of proteins identified as “Secreted” (85.1% of 562 proteins) were downregulated compared to WT litter mates (Fig. 3.23E).

The small number of significant hits might be explained by the limited sample size used for the mass spectrometry experiment (n=5). However, in the list of the secreted proteins downregulated in *Cyth2*-deficient neonate plasma, one of the strongest reductions was identified for WFDC2 (WAP Four-Disulfide Core Domain 2), a protein originally found to be secreted in testes [204]. Wfdc2 is additionally expressed in other tissues, lungs for instance, where it plays a role in surfactant homeostasis [205]. A more detailed look showed that WFDC2 was found in four of five WT samples, while it was detected only in one of five KO samples (data not shown). This indicates that it was below the detection minimum in the KO samples suggesting a strong downregulation upon *Cyth2* depletion. To verify the reduction of WFDC2, Western Blot analysis was performed on other plasma samples from WT (including heterozygous) and *Cyth2*-deficient neonates (Fig. 3.23F). A significant reduction of WFDC2 was found in plasma samples from KO animals compared to their control litter mates, supporting the mass spectrometry results. In contrast, the expression of WFDC2 in the brain was comparable between WT and

KO mice, indicating that loss of *Cyth2* does not cause a reduction in protein expression, but specifically affects its secretion (Fig. 3.23F).

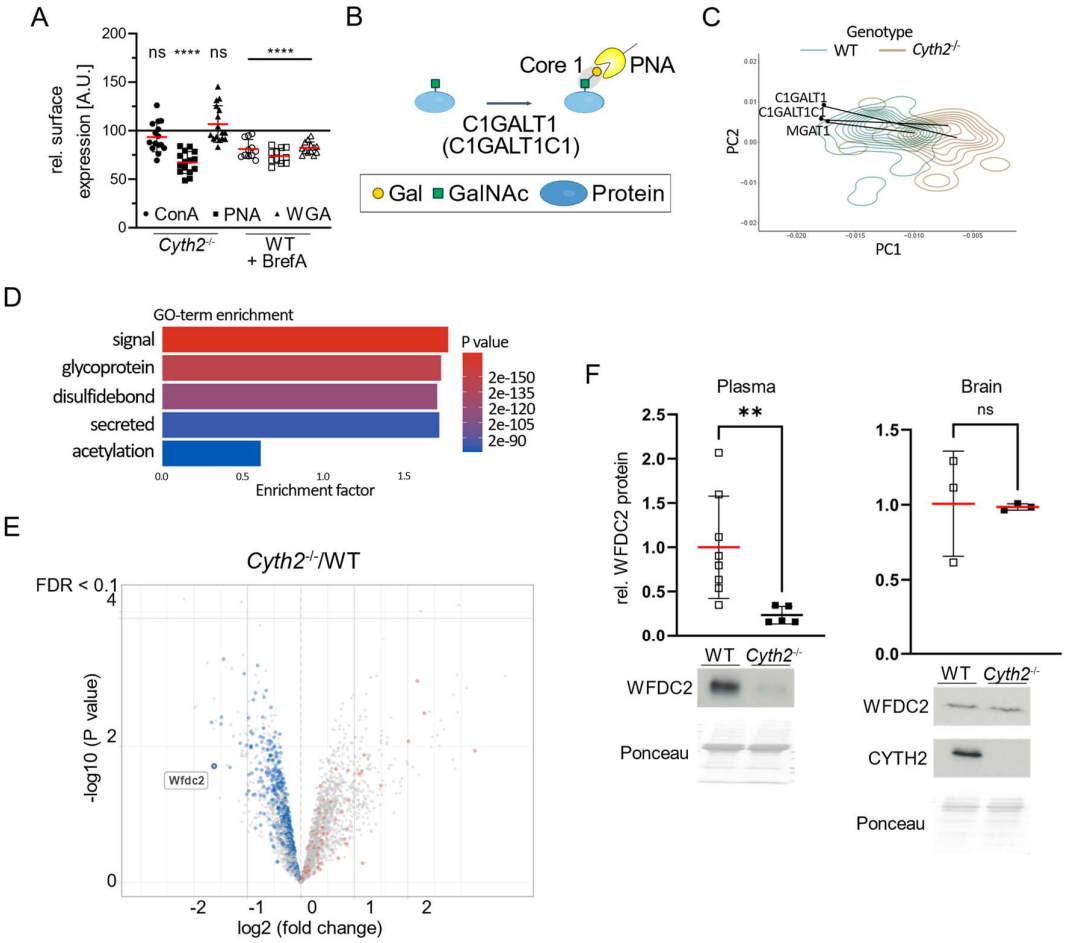

Figure 3.23: *Cyth2*-deficient cells have reduced GalNAc glycosylation and secretion is impaired in *Cyth2* knockout neonates
A) Flow cytometric analysis of lectin stainings (ConA, PNA, WGA) of *Cyth2*-deficient myoblasts or WT myoblasts treated with BrefA compared to untreated WT cells (100% reference line, data represent relative MFIs). Each dot represents one independent experiment (n≥11), red lines represent means ±SD. **B)** Scheme of C1GALT1-mediated Core 1 O-glycosylation initiation on proteins and binding by PNA. C1GALT1, Core 1 Synthase, Glycoprotein-N-Acetylgalactosamine 3-Beta-Galactosyltrasnferase 1; C1GALT1C1, C1GALT1 Specific Chaperone 1; Gal, galactose; GalNAc, N-acetylgalactosamine; PNA, peanut agglutinin. Modified from (Herzog et al. 2014; Stanley 2024). **C)** PCA-based density plot of the Golgi compartment (extracted from Fig. 13B) overlayed with PC1 and PC2 of C1GALT1, C1GALT1C1 and MGAT1 in WT (black dot) and *Cyth2* knockout myoblasts (end of black line). **D)** GO-term enrichment analysis (Fisher's exact for down-regulated proteins) of proteins measured in plasma from neonatal WT and *Cyth2*-deficient mice by mass spectrometry. **E)** Volcano plot of the mass spectrometry data analyzed in C), comparing KO/WT. Secreted proteins (GO: KW0964) are highlighted in blue (down) or red (up), all other proteins are represented as grey dots. **F)** Western Blot analysis of WFDC2 in neonatal plasma (left) or brain (right) of WT and *Cyth2*-deficient mice. Top: Average signal intensity (red line; ±SD; n≥ 3) normalized to total protein loaded as determined by Ponceau staining. Bottom: representative immunoblots. Statistical significance was tested by Mann-Whitney test (*p < 0.05; **p < 0.01; ***p < 0.001; ns = not significant). Lectin analysis by flow cytometry and WFDC2 Western Blots were performed by Dr. Bettina Jux. Mass spectrometry plasma was performed by Dr. Marc Sylvester, data were analysed by Dr. Farhad Shakeri and Andreas Buness (D).

Taken together, Golgi volume and surface area were found to be decreased in *Cyth2*-deficient myoblasts. This effect was also observed in A7r5 and HEK293T cells, indicating a conserved mechanism responsible for Golgi size control. The Golgi volume reduction in *Cyth2*-deficient myoblasts was rescued specifically by overexpression of *Cyth2* in its 3G-isoform. Further, the rescue was independent of the CYTH2 GEF function, as a GEF-inactive mutant rescued Golgi size comparable to WT CYTH2-3G. Functionally, specific reactions of the glycosylation pathway were shown to be hampered in the absence of *Cyth2*. Furthermore, secretion of proteins was decreased in *Cyth2*-deficient mice, as many “Secreted” plasma proteins were less abundant in KO plasma compared to WT controls.

.

4 Discussion

Cytohesins were identified almost 30 years ago as small, cytosolic ARF GEFs. They were attributed to a variety of cellular functions, and an even broader spectrum of physiological processes in organisms [32]. However, *in vivo* data about the cytohesin family are sparse, especially for *Cyth2*. In the present study, a conventional KO of *Cyth2* in mice is described for the first time. Mechanistic studies conducted in C2 myoblasts and other cell lines identified novel and essential functions of *Cyth2 in vitro*, which shed light on the mouse phenotype observed.

4.1 Organellar fractioning as an unbiased approach to analyze morphological changes of cellular compartments

ARF GTPases and their GEFs have always been associated with transport processes [129, 32]. To elucidate the impact of *Cyth2* on cellular transport mechanisms, in the present study a global and unbiased approach was chosen for the analysis of protein localization. Based on their sedimentation properties, organelles of WT and *Cyth2*-deficient C2 myoblasts were separated by differential centrifugation (Fig. 2.2, 3.13, 3.14). These experiment suggested the majority of CYTH2 to be bound in protein complexes, which could be mediated by the coiled-coil domain of CYTH2 and is supported by an observed potential for dimerization (Fig. 3.13G; [124, 206, 207]). Furthermore, the results of organellar fractioning revealed the plethora of processes affected by *Cyth2,* leading the presented research to the investigation of endosomal and Golgi-associated transportation.

4.2 *Cyth2* is essential for postnatal survival

Homozygous deletion of *Cyth2* caused neonatal lethality within 20 h after birth, falling into a time range, that is associated with homeostasis defects or impaired feeding (Fig. 3.1; [178]). Indeed, milk spots were never found in *Cyth2*-deficient pups. However, impaired feeding is mostly attributed to neuromuscular defects or

maternal behavior. Both were excluded by analysis of tissue-specific KO mice (central nervous system and skeletal muscle), that showed a normal life span, and extensive observation of maternal behavior (Fig. 3.2B, data not shown).

In 2022, a publication described a Cre-loxP-generated *Cyth2* KO mouse line as viable and fertile [158]. Here, conventional *Cyth2* KO mice died within 20 h postnatally and evidence was given for a ubiquitous depletion of *Cyth2* by qPCR or immunoblotting in various organs (Fig. 3.2A). Although the germ line-specific Cre-driver was not stated specifically by London and colleagues, the present data suggest that their observations could derive from partial gene targeting due to leakiness of the Cre-loxP system [158, 208].That study raises a difficulty for further investigation of *Cyth2 in vivo*: Depending on the Cre-driver line used, the leakiness of the Cre-loxP system might be an issue for further experiments [208]. For instance, when *Cyth2* is analyzed in inducible KO systems to avoid perinatal lethality of full-KO animals or compensatory processes of the conventional KO model. In this regard, successful targeting of *Cyth2* in tissue-specific KO animals was proven by Western Blot and qPCR in the laboratory (data not shown). However, residual amounts of CYTH2 were often detected and cannot be discriminated as the result of cell contaminations from non-targeted tissue, or as insufficient Cre activity in targeted cells. Additionally, further analysis of tissue-specific KO systems would be a time-consuming and cost-intensive work, as only a few organs such as the heart or liver can be targeted to a huge extent knocking out *Cyth2* in a single cell type using cardiomyocytes or hepatocytes, respectively.

4.3 *Cyth2* modulates mTOR signaling

The comparative analysis of tissue-specific *Cyth2* KO mice should benefit the interpretation of the lethal full-KO phenotype. Previous experiments in liver-specific *Cyth2* KO mice pointed towards a metabolic impact of *Cyth2*, and analysis of metabolic parameters in newborn mice revealed increased amino acid levels in the plasma of *Cyth2*-deficient neonates (Fig. 3.2, 3.3). In autophagy-impaired mice amino acid levels were decreased compared to WT littermates, while treatment with rapamycin increased the amount of free plasma amino acids in mice with excessive

mTOR activity [209, 191, 210]. To understand the cause of increased amino acids in plasma of *Cyth2*-deficient neonates, the mTOR cascade was investigated in the C2 myoblast model system.

Analyzing mTOR signaling in *Cyth2* KO myoblasts revealed an imbalance in downstream target phosphorylation in steady state (Fig. 3.4, 4.1). Downstream of mTORC1, phosphorylation of ULK1 and p70S6K was decreased, while phosphorylation of 4E-BP1 was increased. Furthermore, AMPK and phospho-AMPK

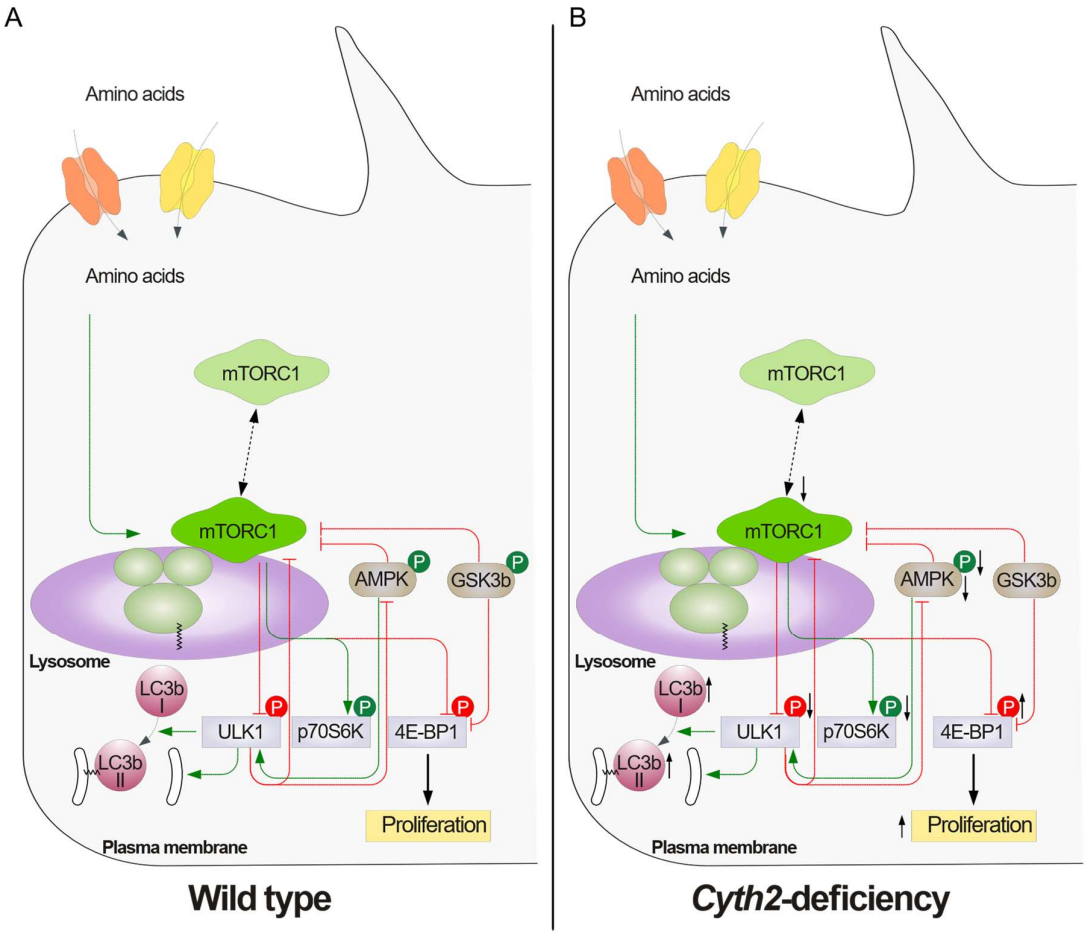

Figure 4.1: Imbalanced mTORC1 signaling in *Cyth2*-deficient C2 myoblasts
A) Modified mTORC1 signaling pathway based on Fig. 1.3. Activated ULK1 not only induces autophagy inducing phagophore formation, but also signals back to mTORC1 and AMPK to prevent further autophagy induction as negative feedback. Additionally, mTORC1 signaling can be modulated by other signaling pathway via the glycogen synthase kinase (GSK3b), which is able to block mTORC1 and to phosphorylate and thereby inhibit 4E-BP1 similar to mTORC1. **B)** In Cyth2 KO myoblasts the recruitment of mTOR to the lysosome is impaired and phosphorylations of ULK1, p70S6K and AMPK are decreased, while phosphorylation of 4E-BP1 is increased. Additionally, protein levels of AMPK are decreased, while LC3b I and II expression is elevated. The small black arrows next to proteins or phosphorylations indicate the observed changes in steady state of Cyth2-deficient myoblasts (compare Fig. 3.4-5). Modified from (Condon and Sabatini 2019).

levels were both reduced, and the phosphorylation of AKT at S473 and T308 was unaffected by the depletion of *Cyth2* (Fig. 3.4). Re-feeding and kinetic assays pin-pointed the distorted mTORC1 activity towards ULK1 to be mainly affected by the loss of *Cyth2* (Fig. 3.6, 3.9), supported by the observation that inhibition of C2 myoblasts with SecinH3 mainly blocked ULK1 phosphorylation but did not or only mildly affect the phosphorylation status of p70S6K (Fig. 3.11B, D). Co-localization analysis of LAMP2 and mTOR by immunofluorescence revealed a minor but significant decrease in mTOR recruitment to the lysosomal surface, which is a central step in mTOR activation (Fig. 3.12).

Assuming mTORC1-mediated ULK1 phosphorylation is initially affected by *Cyth2* depletion, ULK1 could be hyperactive in *Cyth2*-deficient cells due to increased interaction with AMPK [211, 212]. Consequently, in a negative feedback loop, ULK1 could deactivate AMPK and Raptor to block further autophagy induction as well as anabolic activity of the mTORC1 complex (Fig. 3.4; [213–215]). This would explain the decreased levels of phosphorylated p70S6K and AMPK (Fig. 3.4). AKT phosphorylation at S473 being unaffected by the loss of Cyth2 suggests that Cyth2 modulates only mTORC1 signaling, as pAKT(S473) is a downstream target of the mTORC2 complex [216]. Importantly, phosphorylation levels of AKT at T308, which lies downstream of insulin receptor signaling, were comparable in liver tissue of insulin-treated liver-specific *Cyth2* KO mice and in *Cyth2*-deficient myoblasts, (Fig. 3.4, 3.7-9). This highlights a distinct function of *Cyth2* compared to the Drosophila homolog steppke and the mammalian *Cyth3*, which were both shown to be involved in proximal insulin receptor signaling [150, 151].

4.3.1 *Cyth2* deficiency appears to mildly induce ULK1 activity and autophagy

Differential centrifugation experiments revealed a shift of ULK1 from lower-g fractions (membrane-associated) to higher-g fractions in *Cyth2*-deficient myoblasts (protein complexes; Fig. 3.13C). Recently, it was published that upon starvation ULK1 forms multimeric complexes before the initiation of the phagophore membrane, supporting the hypothesis of increased ULK1 activity [217]. By tendency, proteasomal degradation of ULK1 was increased in *Cyth2*-deficient cells, again

corresponding to ULK1 hyperactivity (Fig. 3.10, section 4.3). Functionally, hyperactive ULK1 is in line with the increased levels of LC3b (Fig. 3.5). However, increased LC3b could also indicate blocked autophagy, which is why kinetic studies and the use of autophagy inhibitors such as BafA1 would be required for a final conclusion [218]. To validate the re-location of ULK1, immunofluorescence analysis of the kinase would be of great interest. The lack of suitable antibodies imposes the necessity for protein labeling, though. As ULK1 overexpression with a classical vector system is difficult due to the protein size, GFP-coupling of a known and specific interactor of ULK1 (such as ATG101) or the genome-edited expression of ULK1 fusion proteins are potential approaches for future studies [217, 219]. Additionally, as amino acid re-feeding appears to trigger the hampered ULK1 phosphorylation (Fig. 3.9), differential centrifugation experiments with starved and re-fed cells could reveal, how CYTH2 affects the metabolic switch upon amino acid stimulation. Together, the observations on ULK1 and LC3b suggest a mild increase in autophagy activity in *Cyth2*-deficient C2 myoblasts.

4.3.2 GSK3b activity might explain elevated 4E-BP1 phosphorylation despite decreased ULK1 and p70S6K phosphorylation

The remaining question is, why levels of phosphorylated 4E-BP1 were increased, while phospho-p70S6K was decreased (Fig. 3.4). Even though 4E-BP1 is one of the main targets of the mTORC1 complex and its phosphorylation status is a useful marker for mTOR activity, GSK3b acts as an additional kinase for 4E-BP1 (Qin et al. 2016; Shah et al. 2000). Additionally, in an Alzheimer's disease model hyperactive GSK3a/b was found to correlate with lower mTOR signaling [220]. This might explain the increased levels of phosphorylated 4E-BP1 in *Cyth2*-deficient myoblasts, despite the decrease in pS6K(T389) (Fig. 3.5). Further, increased levels of 4E-BP1 phosphorylation are correlated with the growth of several human cancer entities [221–223]. Correspondingly, besides the increased levels of phosphorylated 4E-BP1, *Cyth2*-deficient myoblasts showed elevated proliferation rates compared to WT controls (Fig. 3.4-5).

Of note, *Cyth2* was identified as a prognostic marker for hepatocellular carcinoma and SecinH3-treated lung cancer xenografts showed reduced EGFR signaling and proliferation, which is why SecinH3 was proposed to be used in cancer therapy [224, 225]. The present thesis would strongly argue against the therapeutic potential of cytohesin inhibition, as *Cyth2*-deficient cells were observed to be hyperproliferative (Fig. 3.5A). Besides many unforeseen side effects of SecinH3, these contradicting results need clarification and evaluation, whether SecinH3 could work only in a subset of cells as a therapeutic, or if the pan-inhibitory effect of SecinH3 is beneficial in contrast to the single loss of *Cyth2* in the present study.

To fully understand the alterations in mTORC1 signaling in *Cyth2*-depleted cells, a more detailed analysis of activation markers is required. First and foremost, assessment of the mTOR kinase activity would verify, whether the decreased lysosomal co-localization of mTOR and LAMP2 observed in *Cyth2*-deficient myoblasts has consequences for mTOR activity or not (Fig. 3.12). The phosphorylation of mTOR on Ser2481 would be a potential target to test this possibility [226]. Alternatively, the use of a bio-sensor for mTOR activity such as TORCAR would elucidate, whether a specific subset of mTOR remains inactive, a pool potentially specific to phosphorylate ULK1 [227]. Such investigations would allow the differentiation between mTORC1 and mTORC2 and would further shed light on the potential interference by GSK3b signaling [226, 227]. The fact that *Cyth2*-deficient myoblasts did not show significant alterations in oxygen consumption or extracellular acidification (Fig. 3.5) indicates that they have no necessity to switch metabolism based on an imbalanced ULK1 signaling.

4.3.3 Imbalanced mTORC1 signaling in *Cyth2*-deficient neonates is unlikely to cause postnatal lethality

Taken together, *Cyth2* appears to be a fine-tuning modulator for ULK1 activity and its loss leads via feedback loops to an imbalance in mTOR signaling with mild consequences on cell growth and autophagy. Whether *Cyth2* affects mTOR signaling proximally or controls distal mechanisms, remains elusive. Transferring the mTOR signaling imbalance from C2 myoblasts to the murine organism, distorted

mTOR signaling and mildly increased ULK1-dependent autophagy as found in the cell system (Fig. 3.4-5) could explain the observed increase in amino acid levels in *Cyth2*-deficient newborns (Fig. 3.3). However, metabolic diseases such as phenylketonuria or homocystinurea are the only conditions stating detrimental effects of elevated amino acid levels in the plasma of newborns. Furthermore, defective amino acid metabolism is usually associated with developmental retardation, not early postnatal lethality [228–230]. Therefore, metabolic alterations in *Cyth2*-deficient newborns probably do not explain neonatal lethality.

4.4 *Cyth2* regulates the number of endosomes

Changes in the number and volume of endosomes are usually associated with alterations in endocytic activity, endosomal recycling, or degradative processing, and several pathologies have been described to affect the endosomal cargo flux [231–233]. However, these reports rarely quantitatively addressed endosomal counts [234]. In the present study, differential centrifugation indicated changes in the precipitation of endosomes by marker protein de-localization of ARF-GTPases and V-ATPase (Fig. 3.13G). In investigating further, higher numbers of early and late endosomes were observed in C2 myoblasts and smooth muscle cells after depletion of *Cyth2*. These results were partially reproduced in HEK293T cells, MEFs, and the dendritic MuTu cell line (Fig. 3.15-16). In C2 myoblasts and A7r5 cells, the accumulation of RAB5-positive endosomes was propagated to the late endosomal compartment (RAB7-positive structures) and in C2 cells even further to the lysosomes (Fig. 3.15-16). Such propagation through the degradative pathway of an initial accumulation of early endosomes is supported by a previous report, in which the knockdown of RAB5 reduced the amount of early and late endosomes as well as lysosomes [73]. Thus, a regulatory function of CYTH2 at one stage of the endocytic pathway could still affect the entire cascade.

4.4.1 Where and how does *Cyth2* regulate the endocytic pathway?

Blockage of ARF6 at the plasma membrane hampers endocytosis, imposing a role for CYTH2 as an activator of ARF GTPases in that process [235, 146, 236–238]. However, those reports focused on the endocytic uptake of receptors or receptor-bound cargo and did not measure endosomal numbers. Studies about the interplay between ARF and RAB GTPases are rare and a comprehensive overview of endocytotic targets, trafficking routes, and shared or specific membrane-enclosed compartments is missing. Future experiments would need to assess cargo transport, GTPase activity, and GTPase location in parallel and dynamically, to elucidate the interactions between the ARF and RAB network and the exact position of CYTH2 in the endocytic pathway. Assuming a role for CYTH2 in endocytosis, the proposed analysis would clarify, whether the increased number of RAB5-positive vesicles found in this study (Fig. 3.15-16) is a compensatory adaptation to ensure sufficient cargo internalization when the ARF system is defective. Including a broader spectrum of endosomal markers would further improve the identification of the structures analyzed in the present study.

Treatment of WT C2 myoblasts with the cytohesin inhibitor SecinH3 increased the early endosomal counts similar to the depletion of *Cyth2*, indicating an ARF-dependent mechanism (Fig. 3.18). At the same time, RAB7-positive structures were not significantly increased in WT myoblasts upon SecinH3 treatment, as if cargo flow from early to late endosomes was disrupted. As an alternative to early endocytic events, CYTH2 and ARF6 might be involved in endosomal transformation along the proteolytic pathway by interaction with the V-ATPase [146, 239]. The absence of *Cyth2* would hamper the early-to-late endosomal transition: ARF6, bound to the pH-sensing V-ATPase, would no longer be activated by the small ARF GEF to coordinate transportation from the early to late endosomes [146, 240]. This interpretation corresponds to a recent report about reduced influenza infection of cells lacking *Cyth2*, which stated a decreased co-localization of virus particles with RAB7 but not with RAB5 [147]. Those results are not directly comparable with the present study, because Yi and colleagues did not state anything about endosomal numbers, only the overlay of virus and late endosomes [147]. Nevertheless, that study suggests a role of *Cyth2* in endosomal transition instead of early endocytosis.

The data presented here also suggest a primary effect of cytohesin inhibition on RAB5-positive early endosomes, subsequently propagated to the late endosomes and lysosomes.

4.4.2 Endosomal regulation by CYTH2 might involve another cytohesin protein

Inhibitor assay showed a significant reduction of late endosome numbers in KO cells treated with SecinH3, that indicates the involvement of another SecinH3-susceptible counterpart for CYTH2 (Fig. 3.18). However, if that entity is responsible for the accumulation of late endosomes in *Cyth2*-deficient cells, this would suggest an antagonistic effect between the two cytohesins. Previous work in the laboratory (unpublished data) hypothesized an antagonistic mechanism between Cyth1 and Cyth3 during the T cell response against bacterial and viral infections. Despite their homology, that study reported diverging upstream regulatory events for the two cytohesins [241]. Additionally, an opposing effect of CYTH2 and CYTH3 on β1-integrin recycling was observed [242]. A potential regulatory mechanism including phosphorylation of CYTH2, that could differ for other cytohesins, was reported in the literature and implied by the present study on protein level: CYTH2 expression was reduced both by FCS treatment (Fig. 3.7) and by treatment of cells with SecinH3 [142, 243]. In C2 myoblasts, CYTH2 appears to reduce the number of endosomes, while another cytohesin may increase the number of endosomes. Future experiments should analyze the expression of other cytohesins in C2 myoblasts and clarify their role in endosomal regulation.

The complexity of endosomal regulation by CYTH2 was emphasized, when overexpression of a single *Cyth2* isoform (2G or 3G; see section 1.6.1) was not able to rescue the accumulation of early or late endosomes (Fig. 3.17). Follow-up experiments with co-expression of both isoforms might clarify whether both isoforms are needed to act concerted in the control of the endosomal compartment, or if other regulatory components are involved and masked the effect of over-expressed *Cyth2*. CYTH2 overexpression levels were only assessed in preliminary experiments by Western Blot (data not shown) and not matched with the immunofluorescence

analysis in rescue experiments. If CYTH2 is a fine-tuning regulator of the endosomal system, protein expression levels of CYTH2 could have been inadequate in the overexpression experiments and a potential reason for the missing rescue effect (Fig. 3.17).

Besides the aforementioned antagonism, the partial congruence of the data obtained with the different cell systems suggests additional regulators in the endosomal compartment (Fig. 3.16), as A7r5 cells showed the same phenotype as C2 myoblasts, namely increased numbers of early and late endosomes, while HEK293T cells, MEFs and MuTu DCs pheno-copied only early or late endosomal counts after loss of *Cyth2*. Because the increase of endosomes was not visible in all analyzed cells, CYTH2 appears to calibrate the endosomal system but is not indispensable for the endocytic pathway.

4.4.3 The endosomal misregulation might add to neonatal lethality in *Cyth2*-deficient mice

The endosomal compartment was found to have accumulated numbers of early and late endosomes in cells lacking *Cyth2* (Fig. 3.15, 3.16). In the literature, the early endosomal marker RAB5a was correlated with a severe inflammatory outcome in lung tissue upon infectious stimulation. Treatment of human pulmonary microvasculature endothelial cells with LPS showed increased total RAB5 expression as well as RAB5 activity, similar to lung tissue of LPS-treated animals [244]. LPS stimulated the internalization of cadherin molecules, causing the disintegration of the endothelial barrier in the lung. Knockdown of RAB5 hampered the internalization and increased the survival of LPS-treated mice [244]. Thus, elevated rates of endocytosis internalizing cell-cell adhesion molecules could have detrimental effects such as impairment of the barrier integrity in the lung and could lead to life-threatening conditions in mice. However, in the present study, mice were not challenged with LPS or other inflammatory stimuli. Also, there was no macroscopic or histological phenotype observed in the lung (data not shown).

On the other hand, decelerated endosomal trafficking, including enlarged early endosomes and a hampered transition to late endosomes, was associated with

neurodegenerative diseases. In Alzheimer's disease, the enlarged early endosomes process higher amounts of Aβ protein, and in Niemann Pick disease type C the endosomal compartment already accumulates cholesterol as part of the lysosomal storage disease [232]. Niemann Pick disease type C was recently found to include respiratory distress, due to changes in cholesterol concentrations in surfactant. A KO mouse model for NPC1 showed postnatal lethality with lipid droplets and accumulation of abnormal surfactant in the lungs [245, 246]. As ARF activity is usually thought to promote endocytosis and internalization at the plasma membrane, one could argue when the depletion of *Arf1* and *Arf6* leads to embryonic lethality that the loss of one of its regulators (*Cyth2*) might cause a phenotype less severe but still fatal [247, 248]. Severe breathing defects were excluded before, as this commonly leads to death within 1-2 hours after birth and the *Cyth2*-deficient mice presented here survived 6-20 h [178]. However, surfactant instability varies in severity and could impair breathing later than 1-2 hours postnatally [249]. Assuming CYTH2-ARF6-dependent endocytosis in the lung, as suggested by SecinH3 assays (Fig. 3.18) and a relatively high expression of CYTH2 in murine lung tissue (Fig. 3.2), the loss of *Cyth2* could impair endocytosis in the lung, causing an imbalance of surfactant composition due to ineffective removal of cholesterol from the extracellular space. A role for ARF6-regulated endocytosis and endocytic recycling in Niemann Pick disease type C was described earlier independent from the lung, affecting cholesterol homeostasis of cellular model systems [250, 251, 252]. In recent years, a mechanism was proposed by Loh and colleagues, showing that intracellular cholesterol levels rise upon uptake or synthesis of cholesterol, which in turn increases Golgi size and protein secretion [253]. This mechanism would support the aforementioned hypothetical imbalance of cholesterol in the surfactant of *Cyth2*-deficient neonates, as Golgi morphology and function were also affected in *Cyth2*-deficient mice (Fig. 3.23).

In summary, *Cyth2* regulates endosomal trafficking and regulates the number of early and late endosomes in a conserved manner (Fig. 3.15-16). The regulation appears to be ARF-dependent, as shown by inhibitor experiments with the cytohesin inhibitor SecinH3 (Fig. 3.18). Based on the literature, defective endosomal transport could affect surfactant composition and lead to breathing deficits, which could

explain neonatal lethality of *Cyth2*-deficient mice. Further *in vivo* experiments would be needed to verify this hypothesis proofing endocytic trafficking defects *in vivo* and analyzing surfactant composition.

4.5 *Cyth2* is a modulator of Golgi structure and function

Golgi morphology is tightly linked to Golgi function, as changes in Golgi volume are often caused by fluctuations in the influx or efflux of proteins passing the secretory pathway [4]. Using differential centrifugation, alterations of the Golgi compartment in *Cyth2*-depleted C2 myoblasts were found and confirmed by immunofluorescence analysis (Fig. 3.14, 3.19, 3.20). Minor changes in Golgi shape, but a significant decrease in Golgi volume and surface area were observed in C2 myoblasts, HEK293T cells, and A7r5 smooth muscle cells deficient for *Cyth2* (Fig. 3.19-20). The Golgi volume of C2 myoblasts reported here (Fig. 3.19; ~30 μm^3) falls into a range observed in retinal pigment epithelial cells (RPE1) and HeLa cells, identified by GFP labeling of the Golgi and the cis-Golgi marker GM130, respectively [254, 255]. However, Golgi size varies between cell states and cell types and a much smaller Golgi volume was observed in rat thyroid cells (also tested with GM130), which corresponds better to the Golgi size observed in HEK293T cells, MEFs, and MuTu cells (Fig. 3.20; [256, 4]). Therefore, the range of detected Golgi volumina should not compromise the interpretation of the presented result, but should be considered comparing the used cells regarding their size and function.

Finding altered Golgi volumina in *Cyth2*-deficient cells was unexpected, as the cytohesin proteins were mostly reported to act close to the plasma membrane [32]. A single publication had reported before that the N-terminal region of CYTH1, -2, and -3, which also comprises the coiled-coil domain, was necessary but also sufficient for the recruitment of these proteins to the Golgi apparatus or a “Golgi-like” structure [132]. In this context, overexpression of *Cyth2* and *Cyth3* was observed to cause Golgi dispersal and impairment of the secretory pathway. In the present study, fragmentation of the Golgi apparatus was not observed in cells overexpressing any isoform or mutant of *Cyth2*, neither in WT nor in *Cyth2* KO cells. This discrepancy between the two studies might be explained by the different model systems used,

but also by the choice of cells to be analyzed in the specific experiments. Here, C2 myoblasts expressing high amounts of the RFP fusion proteins were usually not considered for analysis in the present study, as they often were misshaped and did not appear to be vital anymore. Thus, one cannot fully exclude the detrimental effect of very high expression levels of CYTH2 for the Golgi structure.

To analyze the Golgi structure, a trans-Golgi marker was utilized in this thesis (golgin-97) and showed smaller Golgi volumes in Cyth2-deficient cells (Fig. 3.19-20). The trans-Golgi has been reported to interact with the endosomal compartment, and decreased retrograde transport can cause a reduction in Golgi size [257, 258]. Thus, it would be of great interest to analyze cis- and medial Golgi markers as well, to elucidate the impact of *Cyth2* on the whole Golgi structure and clarify, whether *Cyth2* plays a role in cargo import, export, or intra-Golgi transport processes. Additional methods, such as electron microscopy, could be used to validate the decreased Golgi size observed by immunofluorescence analysis.

Another factor correlating with Golgi size is the expression level of Golgi constituents, including both intra-luminal enzymes as well as structural transmembrane proteins [37, 39]. Golgin-97 intensities measured by immunofluorescence were reduced in *Cyth2*-deficient myoblasts and protein levels were decreased as confirmed by Western Blot. The data corresponded to results from inhibitor assays, in which BrefA caused Golgi disruption and presumably degradation of the Golgi protein golgin-97 (Fig. 3.19, 3.22; [259, 260]). However, the correlation between golgin-97 expression and Golgi volume was not apparent in HEK293T cells, which showed a decreased volume of golgin-97-positive structure but increased maximal fluorescence intensities (Fig. 3.20). Therefore, the turn-over of Golgi components as observed in C2 myoblasts is either a secondary process not found in HEK293T cells, but in both cell types transportation is affected by CYTH2, or the Cyth2-dependent regulation of Golgi morphology differs completely between the two cell types, relying on protein turn-over in myoblasts and on cargo flux in HEK293T cells.

4.5.1 CYTH2 as a regulator of Golgi morphology depends on a yet unidentified interaction partner

The failed rescue of the Golgi volume in *Cyth2*-deficient C2 myoblasts overexpressing coiled-coil-depleted CYTH2 hints towards a protein-protein interaction-dependent function of CYTH2 (Fig. 3.21). Golgi volume was additionally assessed in *Cyth2*-depleted MEFs and MuTu dendritic cells (Fig. 3.20). In both these cells the Golgi volume was increased after KO of *Cyth2* compared to WT controls. The congruent decline of Golgi volume in murine C2 myoblasts, rat A7r5 and human HEK293T cells implies some evolutionary conservation of *Cyth2* regulating the Golgi, while the opposing increase of Golgi size in MEFs and MuTu dendritic cells suggests dependency on the cell type. The proposed interaction-dependent regulation of the Golgi by CYTH2 could explain the opposing effect of *Cyth2* on Golgi volume in different cell types, as MEFs and MuTus might express other interactors and effectors associated with the Golgi apparatus than C2, A7r5, and HEK293T cells.

The interaction of cytohesin proteins is not only predicted for the coiled-coil domain but interactions of cytohesins with ARF-like proteins have been shown to depend on the PH domain, which is also necessary for membrane binding [137, 134, 138]. Cytohesins are expressed in two isoforms, which differ in their affinity to PtdInsPs depending on a 2G or 3G motif. These isoforms were never tested for their affinity to different proteins though. In the present study, it was observed that *Cyth2* overexpression rescued the Golgi phenotype of *Cyth2* KO myoblasts only in the 3G-isoform and restored Golgi volume almost to WT levels (Fig. 3.21). This indicates that CYTH2 for Golgi regulation is not recruited to the plasma membrane upon receptor stimulation, because the three-glycine variant has lower preference for binding PtdIns(3,4,5)P_3, but rather binds to PtdIns(4,5)P_2 [136, 135]. The broad functions of different PtdInsPs have been under intensive investigation for a couple of years now, as reviewed by Posor and others [261]. Follow-up experiments analyzing the function of *Cyth2* on Golgi structure would need to clarify, whether *Cyth2* acts directly at the Golgi apparatus or from a distal position, and whether the protein is recruited by other protein interaction partners or an adjusted lipid composition of the target membrane.

4.5.2 CYTH2-dependent regulation of the Golgi apparatus appears ARF-independent

The rescue experiments of the present study included a GEF-silent mutant, *Cyth2*-E|K. Surprisingly, expressed in the 3G-variant, this mutant was still able to rescue the smaller Golgi volume comparable to the 3G-WT construct. This observation implies an ARF-independent function of CYTH2, which was so far only described for CYTH1 in the context of β2-integrin-mediated adhesion of immune cells to ICAM1 [262]. Such a mechanism was never described in the context of Golgi control or endosomal trafficking, though. An ARF-independent effect of CYTH2 on Golgi volume is supported by the observation that inhibition of C2 myoblasts with SecinH3 did not affect Golgi volume, because SecinH3 specifically inhibits the ARF GEF activity of cytohesin proteins (Fig. 3.22). Of note, DMSO controls of WT and *Cyth2*-deficient myoblasts showed comparable Golgi size, indicating some effect of DMSO on Golgi volume. Thus, the solvent of SecinH3 could mask any effect, the inhibitor itself exerts on the structure of the Golgi apparatus. Repetition of these experiments using a different solvent (e.g., ethanol) would elucidate, whether SecinH3 does affect Golgi morphology. In contrast to SecinH3, BrefA efficiently disrupted Golgi integrity as indicated by a dispersed golgin-97 signal, serving as a positive control in these assays (Fig. 3.22).

4.5.3 Functional consequences of *Cyth2* deficiency-dependent Golgi volume decrease

Regarding Golgi functionality, this study assessed glycosylation and secretion in *Cyth2*-deficient models. *Cyth2* KO myoblasts were stained for several glycosylation patterns with fluorescently labeled lectins after the differential centrifugation data were re-analyzed for glycosyltransferases. C1GALT1, C1GALT1C1 and MGAT1 had been shifted in the absence of *Cyth2* (Fig. 3.23) and staining with PNA revealed a robust and reproducible reduction in core 1 O-glycosylation on the KO cells. A reduction of PNA-staining had been reported for interference with Golgi-to-ER retrograde transport by knockdown of TMEM115 [263]. Additionally, BrefA as a

positive control for impaired Golgi function led to a similar decline in PNA-fluorescence on WT C2 myoblasts. Thus, Cyth2 could be involved in transport processes in the Golgi and thereby facilitating the correct positioning and function of glycosyltransferases such as C1GALT1. These *in vitro* results were transferred to the murine model system. In *Cyth2*-deficient newborn mice, MS analysis of plasma revealed decreased amounts of “Secreted” proteins (Fig. 3.23). Thus, Cyth2 is not only involved in proper glycosylation of proteins, but affects the functional integrity of the secretory pathway.

4.5.4 Malfunction of the Golgi apparatus potentially causes neonatal lethality of *Cyth2* knockout mice shortly after birth

The defective secretion in *Cyth2*-deficient neonates revealed by plasma MS analysis links the mouse phenotype to the *in vitro* observations of smaller Golgis and impaired glycosylation of proteins (Fig. 3.19, 3.23). The reduced Golgi size found in *Cyth2*-depleted C2 myoblasts, A7r5, and HEK293T cells appears to have functional consequences on the cellular level (core 1 O-glycosylation; delocated SLC7A5) as well as the organism level (secretion). However, as “secreted” plasma proteins could not be attributed to a specific organ or tissue (no enrichment for such terms), a multi-systemic phenotype might cause the neonatal lethality of *Cyth2* KO mice.

Similar to *Arf1* and *Arf6* KOs, the depletion of several enzymes involved in glycosylation results in early developmental lethality. KO of *Cyth2* could cause a milder phenotype compared to these when none of the respective pathways and enzymatic cascades are completely impaired, but a broader spectrum of glycosylations is mildly affected by Golgi misfunction in *Cyth2*-deficient organsims (compare section 4.4.3; [247, 2, 248]). Homozygous loss of *C1galt1* and *C1galt1c1* was reported to be embryonically lethal, as was the KO of *Mgat1* [264–267]. All three enzymes were significantly mis-localized in *Cyth2*-deficient myoblasts (Fig. 3.23) and the functional consequence of that was proven by decreased PNA-staining, indicating defective core 1 O-glycosylation. *C1galt1* and its chaperone *C1galt1c1* have been associated with blood homeostasis and vascular integrity [268–271]. However, hemorrhage or aberrant clotting was neither assessed nor observed by

chance during the dissection of *Cyth2*-deficient neonates. Early studies about *Mgat1* ascribed a role to this enzyme in the development of bronchial epithelium [272].

Lung physiology and anatomy were not analyzed in detail in the present study. Thus, one cannot exclude that lung homeostasis could be compromised in *Cyth2*-deficient neonates due to insufficient secretion or glycosylation of surfactant proteins. Plasma MS analysis identified WFDC2 to be one of the strongest downregulated protein in KO samples, a protein secreted for instance in testes but also lung tissue (Fig. 3.23; [204, 205]). In the present study, brain tissue samples were used to show that WFDC2 expression was not altered, despite a strong reduction of its secretion to the plasma, underlining a role of *Cyth2* in transport and secretion, not gene regulation (Fig. 3.23). Loss of *Wfdc2* was reported to cause neonatal lethality due to an imbalance in surfactant composition and consequent impairment of gas exchange in the lung [205, 273]. Additionally, the life span of *Cyth2*- and Wfdc2-deficient mice was similar, supporting the essential role of *Wfdc2* in the *Cyth2*-KO phenotype. Yet, in *Wfdc2* KO neonates partial pulmonary embolism was observed, which was never seen in *Cyth2*-deficient animals. Future experiments would need to assess this observation in more detail and also detect WFDC2 in lung tissue and surfactant after lavage, to verify a reduction of the protein in the bronchial space. A follow-up study could create a tissue-specific KO of *Cyth2* under the control of the Wfdc2 promotor to validate its hypothetical role in the neonatal lethality of *Cyth2* full-KO mice.

Taken together, differential centrifugation revealed alterations in Golgi morphology in *Cyth2*-deficient C2 myoblasts, validated as decreased Golgi volumes in myoblasts, rat A7r5 smooth muscle cells and HEK293T cells (Fig. 3.14, 3.19, 3.20). Golgi volume reduction was not mimicked by cytohesin inhibition with SecinH3 and the smaller Golgi size was rescued by WT and GEF-mutant CYTH2 in its 3G-isoform, implying an ARF-independent but isoform-specific regulation of the Golgi by Cyth2. Functionally, reduced Golgi volume was reflected in defective surface glycosylation of Cyth2-deficient myoblasts and lower levels of secreted proteins in neonatal plasma of Cyth2-KO mice (Fig. 3.23). WFDC2 was identified to play a potential role in the murine KO phenotype, as it stabilizes the

surfactant and maintains breathing in mice. A multi-systemic cause of neonatal lethality in Cyth2-deficient mice is not excluded.

4.6 Concluding remarks

This study is the first report of a conventional KO mouse model of *Cyth2* and found the small ARF-GEF to be essential for postnatal survival (Fig. 3.1). As an unbiased approach to analyze protein localization depending on the activity of *Cyth2*, organelles were separated by differential centrifugation and the distribution of proteins over these organelles analyzed by MS (Fig. 2.2, 3.13-14). This approach suggested changes in the endosomal compartment, the Golgi apparatus, and the mTORC1 signaling cascade - the last discovery corresponding to imbalanced mTORC1 downstream signaling in *Cyth2*-deficient myoblasts (Fig. 3.4). Additionally, differential centrifugation revealed changes in other organelles as well, which were not analyzed in this study due to time restraint. However, the plethora of compartments affected by the loss of *Cyth2* in C2 myoblasts highlights the important role of the ARF-GEF, explaining the broad spectrum of cellular and physiological contexts *Cyth2* was described in so far.

Future experiments should consider the range of processes affected by *Cyth2*, investigating the role of *Cyth2* in all the different compartments that were observed to be changed in *Cyth2*-deficient cells by differential centrifugation. The interconnection of these compartments and their *Cyth2*-dependent regulation needs to be analyzed, as the present study does not distinguish between primary and secondary effects of the *Cyth2* depletion. Potential communication between the processes analyzed here was implied by inhibitor assays using SecinH3: Treatment with SecinH3 increased the numbers of RAB5-positive early endosomes and decreased the phosphorylation of ULK1, comparable to the effect of *Cyth2* depletion (Fig. 3.4&3.11, 3.15&3.17). Together, these observations suggest ARF-dependent processes, which might be connected to each other. Such a connection is supported by previous reports, that found mTOR activity to depend on ARF1 and RAB5 [80, 79].

In contrast, as SecinH3 did not affect the Golgi apparatus despite Golgi volume reduction upon *Cyth2* depletion (Fig. 3.19&3.22), the *Cyth2*-dependent regulation of this compartment is probably not connected to the regulation of endosomes and the mTORC1 signaling pathway. Additionally, Golgi resistance to SecinH3 treatment suggests an ARF-independent function of *Cyth2*, which was supported by effective rescue-experiments with GEF-inactive *Cyth2* constructs (Fig. 3.22). Therefore, the present study not only highlights a role for *Cyth2* at the Golgi apparatus, which was not investigated so far since its first observation, but also proposed for the first time an ARF-independent role of a GEF in Golgi-associated transportation. The functional importance of *Cyth2*-dependent regulation of the Golgi apparatus was evident analyzing surface glycosylation on *Cyth2*-deficient cells and by decreased plasma protein secretion in *Cyth2*-deficient newborns.

Whether *Cyth2* is essential for postnatal survival regulating mTORC1 signaling, the endosomal compartment or Golgi morphology and function remains elusive. This study argues for an important regulatory function of *Cyth2* as a maintenance factor for the surfactant composition in the lung facilitating physiological gas exchange. However, a systemic role of *Cyth2* is not excluded and follow-up experiments are needed to clarify the role of *Cyth2* in lung functionality or to identify other organs, in which *Cyth2* plays a crucial role and affects postnatal survival.

Summary

The protein family of cytohesins, comprising cytohesin-1 to -4, was identified between 1996 and 2000 as small guanine nucleotide exchange factors for ADP ribosylation factor (ARF) GTPases. Since then, the function of cytohesins was mainly investigated in cell systems. Cytohesin-2 (*Cyth2*) was found to activate both ARF6 and ARF1 and to act mainly at the plasma membrane. It was implicated in cortical actin rearrangements, endocytic cargo uptake and cargo flow, and was connected to the regulation of autophagy. Additionally, an association to the Golgi and an involvement in growth factor receptor signaling was proposed. However, the *in vivo* role of *Cyth2* was only analyzed in a few studies so far, assigning *Cyth2* to myelination, eosinophilic inflammation, and virus particle transport. How these *in vitro* observations are linked to the *in vivo* phenotypes is not understood yet.

Therefore, the present study analyzed a conventional *Cyth2* knockout (KO) mouse model comparatively to tissue-specific KOs of *Cyth2*. Full-KO mice exhibited postnatal lethality and observations in liver-specific KO animals suggested a metabolic imbalance in *Cyth2*-deficient mice, which was further analyzed in a CRISPR/Cas9-edited (Clustered regularly interspaced palindromic repeats/CRISPR-associated protein) KO cell line. *In vitro* feeding assays and Western Blot-based analysis of the mTOR (mammalian target of rapamycin) pathway revealed a deregulation of mTORC1 signaling, mainly affecting the autophagy kinase ULK1 (unc-51 Like Autophagy Activating Kinase 1).

To identify the cellular location of CYTH2 regulating ULK1, and the transport processes which might be involved, an unbiased differential centrifugation/mass spectrometry approach was chosen. This method indicated morphological changes of the endosomal compartment and the Golgi apparatus, which were validated by immunofluorescence analysis in various cell types: Elevated numbers of endosomes and alterations of Golgi volume were found in *Cyth2*-deficient cells. Decreased cell surface glycosylation *in vitro* and impaired secretion of proteins to the plasma of *Cyth2* KO mice emphasized a role for *Cyth2* in Golgi function. Mechanistically, inhibitor studies with SecinH3 and rescue experiments in KO myoblasts using *Cyth2* mutants indicated an ARF-dependent regulation of the endosomal network, while

the regulation of the Golgi apparatus appeared ARF-independent, yet requiring the coiled-coil domain for protein interactions.

All in all, the present study provides the first description of a conventional *Cyth2* KO mouse and the essential role of *Cyth2* in the early postnatal period. Mechanistic investigations in cell models revealed a novel function of *Cyth2* in Golgi morphology and function, which was found to be ARF-independent. Additionally, functional consequences of the impaired Golgi activity provide a plausible explanation for the fatal, neonatal phenotype of *Cyth2* KO mice, prompting follow-up experiments.

References

[1] Casey, J.R., Grinstein, S. and Orlowski, J. (2010) Sensors and regulators of intracellular pH. Nature reviews. Molecular cell biology 11, 50–61.

[2] Stanley, P. (2024) Genetics of glycosylation in mammalian development and disease. Nature reviews. Genetics.

[3] Zhen, Y. and Stenmark, H. (2015) Cellular functions of Rab GTPases at a glance. Journal of cell science 128, 3171–3176.

[4] Sengupta, D. and Linstedt, A.D. (2011) Control of organelle size: the Golgi complex. Annual review of cell and developmental biology 27, 57–77.

[5] Wang, X., Qiao, X., Chen, H., Wang, L., Liu, X. and Huang, X. (2023) Synthetic-Cell-Based Multi-Compartmentalized Hierarchical Systems. Small methods 7, e2201712.

[6] Agrawal, A., Scott, Z.C. and Koslover, E.F. (2022) Morphology and Transport in Eukaryotic Cells. Annual review of biophysics 51, 247–266.

[7] Hirokawa, N., Noda, Y., Tanaka, Y. and Niwa, S. (2009) Kinesin superfamily motor proteins and intracellular transport. Nature reviews. Molecular cell biology 10, 682–696.

[8] Béthune, J. and Wieland, F.T. (2018) Assembly of COPI and COPII Vesicular Coat Proteins on Membranes. Annual review of biophysics 47, 63–83.

[9] Mizuno-Yamasaki, E., Rivera-Molina, F. and Novick, P. (2012) GTPase networks in membrane traffic. Annual review of biochemistry 81, 637–659.

[10] Schwartz, S.L., Cao, C., Pylypenko, O., Rak, A. and Wandinger-Ness, A. (2007) Rab GTPases at a glance. Journal of cell science 120, 3905–3910.

[11] Stenmark, H. (2009) Rab GTPases as coordinators of vesicle traffic. Nature reviews. Molecular cell biology 10, 513–525.

[12] Pfeffer, S.R. (2013) Rab GTPase regulation of membrane identity. Current opinion in cell biology 25, 414–419.

[13] Liu, J., Huang, Y., Li, T., Jiang, Z., Zeng, L. and Hu, Z. (2021) The role of the Golgi apparatus in disease (Review). International journal of molecular medicine 47.

[14] Ladinsky, M.S., Mastronarde, D.N., McIntosh, J.R., Howell, K.E. and Staehelin, L.A. (1999) Golgi structure in three dimensions: functional insights from the normal rat kidney cell. The Journal of cell biology 144, 1135–1149.

[15] Rambourg, A. and Clermont, Y. (1990) Three-dimensional electron microscopy: structure of the Golgi apparatus. European journal of cell biology 51, 189–200.

[16] Griffiths, G., Fuller, S.D., Back, R., Hollinshead, M., Pfeiffer, S. and Simons, K. (1989) The dynamic nature of the Golgi complex. The Journal of cell biology 108, 277–297.

[17] Mellman, I. and Simons, K. (1992) The Golgi complex: in vitro veritas? Cell 68, 829–840.

[18] Short, B., Haas, A. and Barr, F.A. (2005) Golgins and GTPases, giving identity and structure to the Golgi apparatus. Biochimica et biophysica acta 1744, 383–395.

[19] Short, B., Preisinger, C., Körner, R., Kopajtich, R., Byron, O. and Barr, F.A. (2001) A GRASP55-rab2 effector complex linking Golgi structure to membrane traffic. The Journal of cell biology 155, 877–883.

[20] Wong, M., Gillingham, A.K. and Munro, S. (2017) The golgin coiled-coil proteins capture different types of transport carriers via distinct N-terminal motifs. BMC biology 15, 3.

[21] Huang, C. and Chang, A. (2011) pH-dependent cargo sorting from the Golgi. The Journal of biological chemistry 286, 10058–10065.

[22] Gauthier, N.C., Rossier, O.M., Mathur, A., Hone, J.C. and Sheetz, M.P. (2009) Plasma membrane area increases with spread area by exocytosis of a GPI-anchored protein compartment. Molecular biology of the cell 20, 3261–3272.

[23] Saini, D.K., Chisari, M. and Gautam, N. (2009) Shuttling and translocation of heterotrimeric G proteins and Ras. Trends in pharmacological sciences 30, 278–286.

[24] Baeuerle, P.A. and Huttner, W.B. (1987) Tyrosine sulfation is a trans-Golgi-specific protein modification. The Journal of cell biology 105, 2655–2664.

[25] Moremen, K.W., Tiemeyer, M. and Nairn, A.V. (2012) Vertebrate protein glycosylation: diversity, synthesis and function. Nature reviews. Molecular cell biology 13, 448–462.

[26] Seidah, N.G., Sadr, M.S., Chrétien, M. and Mbikay, M. (2013) The multifaceted proprotein convertases: their unique, redundant, complementary, and opposite functions. The Journal of biological chemistry 288, 21473–21481.

[27] Joshi, H.J., Narimatsu, Y., Schjoldager, K.T., Tytgat, H.L.P., Aebi, M., Clausen, H. and Halim, A. (2018) SnapShot: O-Glycosylation Pathways across Kingdoms. Cell 172, 632-632.e2.

[28] Schjoldager, K.T., Narimatsu, Y., Joshi, H.J. and Clausen, H. (2020) Global view of human protein glycosylation pathways and functions. Nature reviews. Molecular cell biology 21, 729–749.

[29] Vliegenthart, J.F. and Casset, F. (1998) Novel forms of protein glycosylation. Current opinion in structural biology 8, 565–571.

[30] Welch, L.G. and Munro, S. (2019) A tale of short tails, through thick and thin: investigating the sorting mechanisms of Golgi enzymes. FEBS letters 593, 2452–2465.

[31] Goud, B., Liu, S. and Storrie, B. (2018) Rab proteins as major determinants of the Golgi complex structure. Small GTPases 9, 66–75.

[32] Sztul, E. et al. (2019) ARF GTPases and their GEFs and GAPs: concepts and challenges. Molecular biology of the cell 30, 1249–1271.

[33] Clermont, Y., Rambourg, A. and Hermo, L. (1995) Trans-Golgi network (TGN) of different cell types: three-dimensional structural characteristics and variability. The Anatomical record 242, 289–301.

[34] Kondylis, V., van Nispen tot Pannerden, Hezder E., Herpers, B., Friggi-Grelin, F. and Rabouille, C. (2007) The golgi comprises a paired stack that is separated at G2 by modulation of the actin cytoskeleton through Abi and Scar/WAVE. Developmental cell 12, 901–915.

[35] Shima, D.T., Haldar, K., Pepperkok, R., Watson, R. and Warren, G. (1997) Partitioning of the Golgi apparatus during mitosis in living HeLa cells. The Journal of cell biology 137, 1211–1228.

[36] Shorter, J., Beard, M.B., Seemann, J., Dirac-Svejstrup, A.B. and Warren, G. (2002) Sequential tethering of Golgins and catalysis of SNAREpin assembly by the vesicle-tethering protein p115. The Journal of cell biology 157, 45–62.

[37] Guo, Y. and Linstedt, A.D. (2006) COPII-Golgi protein interactions regulate COPII coat assembly and Golgi size. The Journal of cell biology 174, 53–63.

[38] Burman, J.L., Hamlin, J.N.R. and McPherson, P.S. (2010) Scyl1 regulates Golgi morphology. PloS one 5, e9537.

[39] Travers, K.J., Patil, C.K., Wodicka, L., Lockhart, D.J., Weissman, J.S. and Walter, P. (2000) Functional and genomic analyses reveal an essential coordination between the unfolded protein response and ER-associated degradation. Cell 101, 249–258.

[40] Hickey, K.L., Swarup, S., Smith, I.R., Paoli, J.C., Miguel Whelan, E., Paulo, J.A. and Harper, J.W. (2023) Proteome census upon nutrient stress reveals Golgiphagy membrane receptors. Nature 623, 167–174.

[41] Miyata, S., Mizuno, T., Koyama, Y., Katayama, T. and Tohyama, M. (2013) The endoplasmic reticulum-resident chaperone heat shock protein 47 protects the Golgi apparatus from the effects of O-glycosylation inhibition. PloS one 8, e69732.

[42] Nthiga, T.M., Shrestha, B.K., Bruun, J.-A., Larsen, K.B., Lamark, T. and Johansen, T. (2021) Regulation of Golgi turnover by CALCOCO1-mediated selective autophagy. The Journal of cell biology 220.

[43] Rahman, A. et al. (2022) GMAP is an Atg8a-interacting protein that regulates Golgi turnover in Drosophila. Cell reports 39, 110903.

[44] Dippold, H.C. et al. (2009) GOLPH3 bridges phosphatidylinositol-4- phosphate and actomyosin to stretch and shape the Golgi to promote budding. Cell 139, 337–351.

[45] Noske, A.B., Costin, A.J., Morgan, G.P. and Marsh, B.J. (2008) Expedited approaches to whole cell electron tomography and organelle mark-up in situ in high-pressure frozen pancreatic islets. Journal of structural biology 161, 298–313.

[46] Sin, A.T.-W. and Harrison, R.E. (2016) Growth of the Mammalian Golgi Apparatus during Interphase. Molecular and cellular biology 36, 2344–2359.

[47] Aistleitner, K., Clark, T., Dooley, C. and Hackstadt, T. (2020) Selective fragmentation of the trans-Golgi apparatus by Rickettsia rickettsii. PLoS pathogens 16, e1008582.

[48] Mousnier, A. et al. (2014) Human rhinovirus 16 causes Golgi apparatus fragmentation without blocking protein secretion. Journal of virology 88, 11671–11685.

[49] Rohde, J., Emschermann, F., Knittler, M.R. and Rziha, H.-J. (2012) Orf virus interferes with MHC class I surface expression by targeting vesicular transport and Golgi. BMC veterinary research 8, 114.

[50] Zhu, H. et al. (2014) Persistent and acute chlamydial infections induce different structural changes in the Golgi apparatus. International journal of medical microbiology : IJMM 304, 577–585.

[51] Petrosyan, A., Holzapfel, M.S., Muirhead, D.E. and Cheng, P.-W. (2014) Restoration of compact Golgi morphology in advanced prostate cancer enhances susceptibility to galectin-1-induced apoptosis by modifying mucin O-glycan synthesis. Molecular cancer research : MCR 12, 1704–1716.

[52] Tokuda, E. et al. (2014) Phosphatidylinositol 4-phosphate in the Golgi apparatus regulates cell-cell adhesion and invasive cell migration in human breast cancer. Cancer research 74, 3054–3066.

[53] Zhao, Y. et al. (2006) Deletion of core fucosylation on alpha3beta1 integrin down-regulates its functions. The Journal of biological chemistry 281, 38343–38350.

[54] Zhao, J., Yang, C., Guo, S. and Wu, Y. (2015) GM130 regulates epithelial-to-mesenchymal transition and invasion of gastric cancer cells via snail. International Journal of Clinical and Experimental Pathology 8, 10784–10791.

[55] Covarrubias-Pinto, A. et al. (2021) Impaired intracellular trafficking of sodium-dependent vitamin C transporter 2 contributes to the redox imbalance in Huntington's disease. Journal of neuroscience research 99, 223–235.

[56] Joshi, G. and Wang, Y. (2015) Golgi defects enhance APP amyloidogenic processing in Alzheimer's disease. BioEssays : news and reviews in molecular, cellular and developmental biology 37, 240–247.

[57] Rendón, W.O., Martínez-Alonso, E., Tomás, M., Martínez-Martínez, N. and Martínez-Menárguez, J.A. (2013) Golgi fragmentation is Rab and SNARE dependent in cellular models of Parkinson's disease. Histochemistry and cell biology 139, 671–684.

[58] Naslavsky, N. and Caplan, S. (2018) The enigmatic endosome - sorting the ins and outs of endocytic trafficking. Journal of cell science 131.

[59] Scott, C.C., Vacca, F. and Gruenberg, J. (2014) Endosome maturation, transport and functions. Seminars in cell & developmental biology 31, 2–10.

[60] Seaman, M.N.J. (2008) Endosome protein sorting: motifs and machinery. Cellular and molecular life sciences : CMLS 65, 2842–2858.

[61] Deborde, S., Perret, E., Gravotta, D., Deora, A., Salvarezza, S., Schreiner, R. and Rodriguez-Boulan, E. (2008) Clathrin is a key regulator of basolateral polarity. Nature 452, 719–723.

[62] Goss, J.W. and Toomre, D.K. (2008) Both daughter cells traffic and exocytose membrane at the cleavage furrow during mammalian cytokinesis. The Journal of cell biology 181, 1047–1054.

[63] Gould, G.W. and Lippincott-Schwartz, J. (2009) New roles for endosomes: from vesicular carriers to multi-purpose platforms. Nature reviews. Molecular cell biology 10, 287–292.

[64] Palamidessi, A. et al. (2008) Endocytic trafficking of Rac is required for the spatial restriction of signaling in cell migration. Cell 134, 135–147.

[65] Murphy, R.F., Powers, S. and Cantor, C.R. (1984) Endosome pH measured in single cells by dual fluorescence flow cytometry: rapid acidification of insulin to pH 6. The Journal of cell biology 98, 1757–1762.

[66] Poteryaev, D., Datta, S., Ackema, K., Zerial, M. and Spang, A. (2010) Identification of the switch in early-to-late endosome transition. Cell 141, 497–508.

[67] Rink, J., Ghigo, E., Kalaidzidis, Y. and Zerial, M. (2005) Rab conversion as a mechanism of progression from early to late endosomes. Cell 122, 735–749.

[68] Dong, B., Kakihara, K., Otani, T., Wada, H. and Hayashi, S. (2013) Rab9 and retromer regulate retrograde trafficking of luminal protein required for epithelial tube length control. Nature communications 4, 1358.

[69] Del Nery, E., Miserey-Lenkei, S., Falguières, T., Nizak, C., Johannes, L., Perez, F. and Goud, B. (2006) Rab6A and Rab6A' GTPases play non-overlapping roles in membrane trafficking. Traffic (Copenhagen, Denmark) 7, 394–407.

[70] Mallard, F. et al. (2002) Early/recycling endosomes-to-TGN transport involves two SNARE complexes and a Rab6 isoform. The Journal of cell biology 156, 653–664.

[71] Xie, S., Bahl, K., Reinecke, J.B., Hammond, G.R.V., Naslavsky, N. and Caplan, S. (2016) The endocytic recycling compartment maintains cargo segregation acquired upon exit from the sorting endosome. Molecular biology of the cell 27, 108–126.

[72] Parton, R.G., Schrotz, P., Bucci, C. and Gruenberg, J. (1992) Plasticity of early endosomes. Journal of cell science 103 (Pt 2), 335–348.

[73] Zeigerer, A. et al. (2012) Rab5 is necessary for the biogenesis of the endolysosomal system in vivo. Nature 485, 465–470.

[74] Villaseñor, R., Nonaka, H., Del Conte-Zerial, P., Kalaidzidis, Y. and Zerial, M. (2015) Regulation of EGFR signal transduction by analogue-to-digital conversion in endosomes. eLife 4.

[75] Fielding, A.B. et al. (2005) Rab11-FIP3 and FIP4 interact with Arf6 and the exocyst to control membrane traffic in cytokinesis. The EMBO journal 24, 3389–3399.

[76] Naslavsky, N., Weigert, R. and Donaldson, J.G. (2003) Convergence of non-clathrin- and clathrin-derived endosomes involves Arf6 inactivation and changes in phosphoinositides. Molecular biology of the cell 14, 417–431.

[77] Palacios, F., Price, L., Schweitzer, J., Collard, J.G. and D'Souza-Schorey, C. (2001) An essential role for ARF6-regulated membrane traffic in adherens junction turnover and epithelial cell migration. The EMBO journal 20, 4973–4986.

[78] van Ijzendoorn, Sven C. D. (2006) Recycling endosomes. Journal of cell science 119, 1679–1681.

[79] Schenck, A. et al. (2008) The endosomal protein Appl1 mediates Akt substrate specificity and cell survival in vertebrate development. Cell 133, 486–497.

[80] Li, L. et al. (2010) Regulation of mTORC1 by the Rab and Arf GTPases. The Journal of biological chemistry 285, 19705–19709.

[81] Meng, D., Yang, Q., Wang, H., Melick, C.H., Navlani, R., Frank, A.R. and Jewell, J.L. (2020) Glutamine and asparagine activate mTORC1 independently of Rag GTPases. The Journal of biological chemistry 295, 2890–2899.

[82] Condon, K.J. and Sabatini, D.M. (2019) Nutrient regulation of mTORC1 at a glance. Journal of cell science 132.

[83] Goberdhan, D.C.I., Wilson, C. and Harris, A.L. (2016) Amino Acid Sensing by mTORC1: Intracellular Transporters Mark the Spot. Cell metabolism 23, 580–589.

[84] Kim, J. and Guan, K.-L. (2011) Amino acid signaling in TOR activation. Annual review of biochemistry 80, 1001–1032.

[85] Saxton, R.A. and Sabatini, D.M. (2017) mTOR Signaling in Growth, Metabolism, and Disease. Cell 168, 960–976.

[86] Bar-Peled, L., Schweitzer, L.D., Zoncu, R. and Sabatini, D.M. (2012) Ragulator is a GEF for the rag GTPases that signal amino acid levels to mTORC1. Cell 150, 1196–1208.

[87] Kim, E., Goraksha-Hicks, P., Li, L., Neufeld, T.P. and Guan, K.-L. (2008) Regulation of TORC1 by Rag GTPases in nutrient response. Nature cell biology 10, 935–945.

[88] Sancak, Y., Peterson, T.R., Shaul, Y.D., Lindquist, R.A., Thoreen, C.C., Bar-Peled, L. and Sabatini, D.M. (2008) The Rag GTPases bind raptor and mediate amino acid signaling to mTORC1. Science (New York, N.Y.) 320, 1496–1501.

[89] Sancak, Y., Bar-Peled, L., Zoncu, R., Markhard, A.L., Nada, S. and Sabatini, D.M. (2010) Ragulator-Rag complex targets mTORC1 to the lysosomal surface and is necessary for its activation by amino acids. Cell 141, 290–303.

[90] Saxton, R.A., Chantranupong, L., Knockenhauer, K.E., Schwartz, T.U. and Sabatini, D.M. (2016) Mechanism of arginine sensing by CASTOR1 upstream of mTORC1. Nature 536, 229–233.

[91] Saxton, R.A. et al. (2016) Structural basis for leucine sensing by the Sestrin2-mTORC1 pathway. Science (New York, N.Y.) 351, 53–58.

[92] Nicklin, P. et al. (2009) Bidirectional transport of amino acids regulates mTOR and autophagy. Cell 136, 521–534.

[93] Long, X., Lin, Y., Ortiz-Vega, S., Yonezawa, K. and Avruch, J. (2005) Rheb binds and regulates the mTOR kinase. Current biology : CB 15, 702–713.

[94] Inoki, K., Li, Y., Xu, T. and Guan, K.-L. (2003) Rheb GTPase is a direct target of TSC2 GAP activity and regulates mTOR signaling. Genes & development 17, 1829–1834.

[95] Tee, A.R., Manning, B.D., Roux, P.P., Cantley, L.C. and Blenis, J. (2003) Tuberous sclerosis complex gene products, Tuberin and Hamartin, control mTOR signaling by acting as a GTPase-activating protein complex toward Rheb. Current biology : CB 13, 1259–1268.

[96] Inoki, K., Li, Y., Zhu, T., Wu, J. and Guan, K.-L. (2002) TSC2 is phosphorylated and inhibited by Akt and suppresses mTOR signalling. Nature cell biology 4, 648–657.

[97] Manning, B.D., Tee, A.R., Logsdon, M.N., Blenis, J. and Cantley, L.C. (2002) Identification of the tuberous sclerosis complex-2 tumor suppressor gene product tuberin as a target of the phosphoinositide 3-kinase/akt pathway. Molecular cell 10, 151–162.

[98] Brugarolas, J. et al. (2004) Regulation of mTOR function in response to hypoxia by REDD1 and the TSC1/TSC2 tumor suppressor complex. Genes & development 18, 2893–2904.

[99] Feng, Z., Hu, W., Stanchina, E., Teresky, A.K., Jin, S., Lowe, S. and Levine, A.J. (2007) The regulation of AMPK beta1, TSC2, and PTEN expression by p53: stress, cell and tissue specificity, and the role of these gene products in modulating the IGF-1-AKT-mTOR pathways. Cancer research 67, 3043–3053.

[100] Gwinn, D.M. et al. (2008) AMPK phosphorylation of raptor mediates a metabolic checkpoint. Molecular cell 30, 214–226.

[101] Inoki, K., Zhu, T. and Guan, K.-L. (2003) TSC2 mediates cellular energy response to control cell growth and survival. Cell 115, 577–590.

[102] Makhoul, C., Houghton, F.J., Hinde, E. and Gleeson, P.A. (2023) Arf5-mediated regulation of mTORC1 at the plasma membrane. Molecular biology of the cell 34, ar23.

[103] Liu, G.Y. and Sabatini, D.M. (2020) mTOR at the nexus of nutrition, growth, ageing and disease. Nature reviews. Molecular cell biology 21, 183–203.

[104] Huang, S.-L. et al. (2023) Coronarin A modulated hepatic glycogen synthesis and gluconeogenesis via inhibiting mTORC1/S6K1 signaling and ameliorated glucose homeostasis of diabetic mice. Acta pharmacologica Sinica 44, 596–609.

[105] Islam, M.T. et al. (2024) Endothelial cell-specific reduction in mTOR ameliorates age-related arterial and metabolic dysfunction. Aging cell 23, e14040.

[106] Houde, V.P., Brûlé, S., Festuccia, W.T., Blanchard, P.-G., Bellmann, K., Deshaies, Y. and Marette, A. (2010) Chronic rapamycin treatment causes glucose intolerance and hyperlipidemia by upregulating hepatic gluconeogenesis and impairing lipid deposition in adipose tissue. Diabetes 59, 1338–1348.

[107] Yuan, Q. et al. (2022) Sirt1 Mediates Vitamin D Deficiency-Driven Gluconeogenesis in the Liver via mTorc2/Akt Signaling. Journal of diabetes research 2022, 1755563.

[108] Mestyán, J., Soltész, G., Schultz, K. and Horváth, M. (1975) Hyperaminoacidemia due to the accumulation of gluconeogenic amino acid precursors in hypoglycemic small-for-gestational age infants. The Journal of pediatrics 87, 409–414.

[109] Arrieta-Cruz, I., Su, Y. and Gutiérrez-Juárez, R. (2016) Suppression of Endogenous Glucose Production by Isoleucine and Valine and Impact of Diet Composition. Nutrients 8, 79.

[110] Kadota, Y., Kazama, S., Bajotto, G., Kitaura, Y. and Shimomura, Y. (2012) Clofibrate-induced reduction of plasma branched-chain amino acid concentrations impairs glucose tolerance in rats. JPEN. Journal of parenteral and enteral nutrition 36, 337–343.

[111] Lanza, I.R., Zhang, S., Ward, L.E., Karakelides, H., Raftery, D. and Nair, K.S. (2010) Quantitative metabolomics by H-NMR and LC-MS/MS confirms altered metabolic pathways in diabetes. PloS one 5, e10538.

[112] Zhang, J. et al. (2022) Preoperative administration of branched-chain amino acids reduces postoperative insulin resistance in rats by reducing liver gluconeogenesis. Nutrition & metabolism 19, 78.

[113] Riggi, M., Kusmider, B. and Loewith, R. (2020) The flipside of the TOR coin - TORC2 and plasma membrane homeostasis at a glance. Journal of cell science 133.

[114] Alers, S., Löffler, A.S., Wesselborg, S. and Stork, B. (2012) Role of AMPK-mTOR-Ulk1/2 in the regulation of autophagy: cross talk, shortcuts, and feedbacks. Molecular and cellular biology 32, 2–11.

[115] Pareek, G. and Kundu, M. (2024) Physiological functions of ULK1/2. Journal of molecular biology, 168472.

[116] Rong, Z., Zheng, K., Chen, J. and Jin, X. (2022) Function and regulation of ULK1: From physiology to pathology. Gene 840, 146772.

[117] Ciechomska, I.A., Gabrusiewicz, K., Szczepankiewicz, A.A. and Kaminska, B. (2013) Endoplasmic reticulum stress triggers autophagy in malignant glioma cells undergoing cyclosporine a-induced cell death. Oncogene 32, 1518–1529.

[118] Nie, T. et al. (2016) Regulation of ER stress-induced autophagy by GSK3β-TIP60-ULK1 pathway. Cell death & disease 7, e2563.

[119] Song, L., Sarno, P. and Jope, R.S. (2002) Central role of glycogen synthase kinase-3beta in endoplasmic reticulum stress-induced caspase-3 activation. The Journal of biological chemistry 277, 44701–44708.

[120] Joo, J.H. et al. (2011) Hsp90-Cdc37 chaperone complex regulates Ulk1- and Atg13-mediated mitophagy. Molecular cell 43, 572–585.

[121] Torii, S., Yoshida, T., Arakawa, S., Honda, S., Nakanishi, A. and Shimizu, S. (2016) Identification of PPM1D as an essential Ulk1 phosphatase for genotoxic stress-induced autophagy. EMBO reports 17, 1552–1564.

[122] Allavena, G., Boyd, C., Oo, K.S., Maellaro, E., Zhivotovsky, B. and Kaminskyy, V.O. (2016) Suppressed translation and ULK1 degradation as potential mechanisms of autophagy limitation under prolonged starvation. Autophagy 12, 2085–2097.

[123] Deng, R. et al. (2021) MAPK1/3 kinase-dependent ULK1 degradation attenuates mitophagy and promotes breast cancer bone metastasis. Autophagy 17, 3011–3029.

[124] Chardin, P., Paris, S., Antonny, B., Robineau, S., Béraud-Dufour, S., Jackson, C.L. and Chabre, M. (1996) A human exchange factor for ARF contains Sec7- and pleckstrin-homology domains. Nature 384, 481–484.

[125] Klarlund, J.K., Guilherme, A., Holik, J.J., Virbasius, J.V., Chawla, A. and Czech, M.P. (1997) Signaling by phosphoinositide-3,4,5-trisphosphate through proteins containing pleckstrin and Sec7 homology domains. Science (New York, N.Y.) 275, 1927–1930.

[126] Kolanus, W., Nagel, W., Schiller, B., Zeitlmann, L., Godar, S., Stockinger, H. and Seed, B. (1996) Alpha L beta 2 integrin/LFA-1 binding to ICAM-1 induced by cytohesin-1, a cytoplasmic regulatory molecule. Cell 86, 233–242.

[127] Ogasawara, M. et al. (2000) Similarities in function and gene structure of cytohesin-4 and cytohesin-1, guanine nucleotide-exchange proteins for ADP-ribosylation factors. The Journal of biological chemistry 275, 3221–3230.

[128] Moss, J. and Vaughan, M. (1998) Molecules in the ARF orbit. The Journal of biological chemistry 273, 21431–21434.

[129] Kolanus, W. (2007) Guanine nucleotide exchange factors of the cytohesin family and their roles in signal transduction. Immunological reviews 218, 102–113.

[130] Hiester, K.G. and Santy, L.C. (2013) The cytohesin coiled-coil domain interacts with threonine 276 to control membrane association. PloS one 8, e82084.

[131] Klarlund, J.K., Holik, J., Chawla, A., Park, J.G., Buxton, J. and Czech, M.P. (2001) Signaling complexes of the FERM domain-containing protein GRSP1 bound to ARF exchange factor GRP1. The Journal of biological chemistry 276, 40065–40070.

[132] Lee, S.Y. and Pohajdak, B. (2000) N-terminal targeting of guanine nucleotide exchange factors (GEF) for ADP ribosylation factors (ARF) to the Golgi. Journal of cell science 113 (Pt 11), 1883–1889.

[133] Mansour, M., Lee, S.Y. and Pohajdak, B. (2002) The N-terminal coiled coil domain of the cytohesin/ARNO family of guanine nucleotide exchange factors interacts with the scaffolding protein CASP. The Journal of biological chemistry 277, 32302–32309.

[134] Nagel, W., Zeitlmann, L., Schilcher, P., Geiger, C., Kolanus, J. and Kolanus, W. (1998) Phosphoinositide 3-OH kinase activates the beta2 integrin adhesion pathway and induces membrane recruitment of cytohesin-1. The Journal of biological chemistry 273, 14853–14861.

[135] Klarlund, J.K., Tsiaras, W., Holik, J.J., Chawla, A. and Czech, M.P. (2000) Distinct polyphosphoinositide binding selectivities for pleckstrin homology domains of GRP1-like proteins based on diglycine versus triglycine motifs. The Journal of biological chemistry 275, 32816–32821.

[136] Cronin, T.C., DiNitto, J.P., Czech, M.P. and Lambright, D.G. (2004) Structural determinants of phosphoinositide selectivity in splice variants of Grp1 family PH domains. The EMBO journal 23, 3711–3720.

[137] Hofmann, I., Thompson, A., Sanderson, C.M. and Munro, S. (2007) The Arl4 family of small G proteins can recruit the cytohesin Arf6 exchange factors to the plasma membrane. Current biology : CB 17, 711–716.

[138] Stalder, D., Barelli, H., Gautier, R., Macia, E., Jackson, C.L. and Antonny, B. (2011) Kinetic studies of the Arf activator Arno on model membranes in the presence of Arf effectors suggest control by a positive feedback loop. The Journal of biological chemistry 286, 3873–3883.

[139] Cohen, L.A., Honda, A., Varnai, P., Brown, F.D., Balla, T. and Donaldson, J.G. (2007) Active Arf6 recruits ARNO/cytohesin GEFs to the PM by binding their PH domains. Molecular biology of the cell 18, 2244–2253.

[140] Langille, S.E. et al. (1999) ADP-ribosylation factor 6 as a target of guanine nucleotide exchange factor GRP1. The Journal of biological chemistry 274, 27099–27104.

[141] Macia, E., Chabre, M. and Franco, M. (2001) Specificities for the small G proteins ARF1 and ARF6 of the guanine nucleotide exchange factors ARNO and EFA6. The Journal of biological chemistry 276, 24925–24930.

[142] DiNitto, J.P. et al. (2007) Structural basis and mechanism of autoregulation in 3-phosphoinositide-dependent Grp1 family Arf GTPase exchange factors. Molecular cell 28, 569–583.

[143] Santy, L.C., Ravichandran, K.S. and Casanova, J.E. (2005) The DOCK180/Elmo complex couples ARNO-mediated Arf6 activation to the downstream activation of Rac1. Current biology : CB 15, 1749–1754.

[144] Santy, L.C. and Casanova, J.E. (2001) Activation of ARF6 by ARNO stimulates epithelial cell migration through downstream activation of both Rac1 and phospholipase D. The Journal of cell biology 154, 599–610.

[145] Humphreys, D., Davidson, A., Hume, P.J. and Koronakis, V. (2012) Salmonella virulence effector SopE and Host GEF ARNO cooperate to recruit and activate WAVE to trigger bacterial invasion. Cell host & microbe 11, 129–139.

[146] Hurtado-Lorenzo, A. et al. (2006) V-ATPase interacts with ARNO and Arf6 in early endosomes and regulates the protein degradative pathway. Nature cell biology 8, 124–136.

[147] Yi, C. et al. (2022) Genome-wide CRISPR-Cas9 screening identifies the CYTH2 host gene as a potential therapeutic target of influenza viral infection. Cell reports 38, 110559.

[148] Moreau, K., Ravikumar, B., Puri, C. and Rubinsztein, D.C. (2012) Arf6 promotes autophagosome formation via effects on phosphatidylinositol 4,5-bisphosphate and phospholipase D. The Journal of cell biology 196, 483–496.

[149] Hafner, M. et al. (2006) Inhibition of cytohesins by SecinH3 leads to hepatic insulin resistance. Nature 444, 941–944.

[150] Fuss, B., Becker, T., Zinke, I. and Hoch, M. (2006) The cytohesin Steppke is essential for insulin signalling in Drosophila. Nature 444, 945–948.

[151] Jux, B. et al. (2019) Cytohesin-3 is required for full insulin receptor signaling and controls body weight via lipid excretion. Scientific reports 9, 3442.

[152] Franco, M., Boretto, J., Robineau, S., Monier, S., Goud, B., Chardin, P. and Chavrier, P. (1998) ARNO3, a Sec7-domain guanine nucleotide exchange factor for ADP ribosylation factor 1, is involved in the control of Golgi structure and function. Proceedings of the National Academy of Sciences of the United States of America 95, 9926–9931.

[153] Monier, S., Chardin, P., Robineau, S. and Goud, B. (1998) Overexpression of the ARF1 exchange factor ARNO inhibits the early secretory pathway and causes the disassembly of the Golgi complex. Journal of cell science 111 (Pt 22), 3427–3436.

[154] Torii, T. et al. (2015) Arf6 guanine-nucleotide exchange factor cytohesin-2 regulates myelination in nerves. Biochemical and biophysical research communications 460, 819–825.

[155] Yamauchi, J. et al. (2012) Phosphorylation of cytohesin-1 by Fyn is required for initiation of myelination and the extent of myelination during development. Science signaling 5, ra69.

[156] Ito, A., Fukaya, M., Sugawara, T., Hara, Y., Okamoto, H., Yamauchi, J. and Sakagami, H. (2021) Cytohesin-2 mediates group I metabotropic glutamate receptor-dependent mechanical allodynia through the activation of ADP ribosylation factor 6 in the spinal cord. Neurobiology of disease 159, 105466.

[157] Lolignier, S., Eijkelkamp, N. and Wood, J.N. (2015) Mechanical allodynia. Pflugers Archiv : European journal of physiology 467, 133–139.

[158] London, N.R. et al. (2022) Deletion of Arno Reduces Eosinophilic Inflammation and Interleukin-5 Expression in a Murine Model of Rhinitis. Ear, nose, & throat journal 101, 1S-7S.

[159] Rodríguez, C.I. et al. (2000) High-efficiency deleter mice show that FLPe is an alternative to Cre-loxP. Nature genetics 25, 139–140.

[160] Itzhak 2016.

[161] Yaffe, D. and Saxel, O. (1977) Serial passaging and differentiation of myogenic cells isolated from dystrophic mouse muscle. Nature 270, 725–727.

[162] Kimes, B.W. and Brandt, B.L. (1976) Characterization of two putative smooth muscle cell lines from rat thoracic aorta. Experimental cell research 98, 349–366.

[163] Fuertes Marraco, S.A. et al. (2012) Novel murine dendritic cell lines: a powerful auxiliary tool for dendritic cell research. Frontiers in immunology 3, 331.

[164] Conner, D.A. (2001) Mouse embryo fibroblast (MEF) feeder cell preparation. Current protocols in molecular biology Chapter 23, Unit 23.2.

[165] Livak, K.J. and Schmittgen, T.D. (2001) Analysis of relative gene expression data using real-time quantitative PCR and the 2(-Delta Delta C(T)) Method. Methods (San Diego, Calif.) 25, 402–408.

[166] Joung, J. et al. (2017) Genome-scale CRISPR-Cas9 knockout and transcriptional activation screening. Nature protocols 12, 828–863.

[167] Doench, J.G. et al. (2016) Optimized sgRNA design to maximize activity and minimize off-target effects of CRISPR-Cas9. Nature biotechnology 34, 184–191.

[168] Mosmann, T. (1983) Rapid colorimetric assay for cellular growth and survival: application to proliferation and cytotoxicity assays. Journal of immunological methods 65, 55–63.

[169] Itzhak, D.N., Tyanova, S., Cox, J. and Borner, G.H. (2016) Global, quantitative and dynamic mapping of protein subcellular localization. eLife 5.

[170] Rappsilber, J., Mann, M. and Ishihama, Y. (2007) Protocol for micro-purification, enrichment, pre-fractionation and storage of peptides for proteomics using StageTips. Nature protocols 2, 1896–1906.

[171] Demichev, V., Messner, C.B., Vernardis, S.I., Lilley, K.S. and Ralser, M. (2020) DIA-NN: neural networks and interference correction enable deep proteome coverage in high throughput. Nature methods 17, 41–44.

[172] Cox, J., Hein, M.Y., Luber, C.A., Paron, I., Nagaraj, N. and Mann, M. (2014) Accurate proteome-wide label-free quantification by delayed normalization and

maximal peptide ratio extraction, termed MaxLFQ. Molecular & cellular proteomics : MCP 13, 2513–2526.

[173] Tyanova, S. et al. (2016) The Perseus computational platform for comprehensive analysis of (prote)omics data. Nature methods 13, 731–740.

[174] R Core Team (2021) R: A language and environment for statistical computing. Vienna, Austria.

[175] Huber, W., Heydebreck, A., Sültmann, H., Poustka, A. and Vingron, M. (2002) Variance stabilization applied to microarray data calibration and to the quantification of differential expression. Bioinformatics (Oxford, England) 18 Suppl 1, S96-104.

[176] Hediyeh-Zadeh, S., Webb, A.I. and Davis, M.J. (2023) MsImpute: Estimation of Missing Peptide Intensity Data in Label-Free Quantitative Mass Spectrometry. Molecular & cellular proteomics : MCP 22, 100558.

[177] Ritchie, M.E., Phipson, B., Di Wu, Hu, Y., Law, C.W., Shi, W. and Smyth, G.K. (2015) limma powers differential expression analyses for RNA-sequencing and microarray studies. Nucleic acids research 43, e47.

[178] Turgeon, B. and Meloche, S. (2009) Interpreting neonatal lethal phenotypes in mouse mutants: insights into gene function and human diseases. Physiological reviews 89, 1–26.

[179] Uhlen, M. (2023) Human Protein Atlas. Human Protein Atlas proteinatlas.org.

[180] Bult, C.J. (2022) Mouse Genome Informatics. http://www.informatics.jax.org.

[181] Tronche, F. et al. (1999) Disruption of the glucocorticoid receptor gene in the nervous system results in reduced anxiety. Nature genetics 23, 99–103.

[182] Li, S. et al. (2005) Requirement for serum response factor for skeletal muscle growth and maturation revealed by tissue-specific gene deletion in mice. Proceedings of the National Academy of Sciences of the United States of America 102, 1082–1087.

[183] Kellendonk, C., Opherk, C., Anlag, K., Schtz, G. and Tronche, F. (2000) Hepatocyte-specific expression of Cre recombinase. genesis 26, 151–153.

[184] Clausen, B.E., Burkhardt, C., Reith, W., Renkawitz, R. and Förster, I. (1999) Conditional gene targeting in macrophages and granulocytes using LysMcre mice. Transgenic research 8, 265–277.

[185] Agah, R., Frenkel, P.A., French, B.A., Michael, L.H., Overbeek, P.A. and Schneider, M.D. (1997) Gene recombination in postmitotic cells. Targeted expression of Cre recombinase provokes cardiac-restricted, site-specific rearrangement in adult ventricular muscle in vivo. The Journal of clinical investigation 100, 169–179.

[186] Rehmani, T., Salih, M. and Tuana, B.S. (2019) Cardiac-Specific Cre Induces Age-Dependent Dilated Cardiomyopathy (DCM) in Mice. Molecules (Basel, Switzerland) 24.

[187] Alessi, D.R., James, S.R., Downes, C.P., Holmes, A.B., Gaffney, P.R., Reese, C.B. and Cohen, P. (1997) Characterization of a 3-phosphoinositide-dependent protein kinase which phosphorylates and activates protein kinase Balpha. Current biology : CB 7, 261–269.

[188] Thomas, G. and Hall, M.N. (1997) TOR signalling and control of cell growth. Current opinion in cell biology 9, 782–787.

[189] Wang, N.D. et al. (1995) Impaired energy homeostasis in C/EBP alpha knockout mice. Science (New York, N.Y.) 269, 1108–1112.

[190] Scheuner, D. et al. (2001) Translational control is required for the unfolded protein response and in vivo glucose homeostasis. Molecular cell 7, 1165–1176.

[191] Kuma, A. et al. (2004) The role of autophagy during the early neonatal starvation period. Nature 432, 1032–1036.

[192] Shaw, R.J., Bardeesy, N., Manning, B.D., Lopez, L., Kosmatka, M., DePinho, R.A. and Cantley, L.C. (2004) The LKB1 tumor suppressor negatively regulates mTOR signaling. Cancer cell 6, 91–99.

[193] Choo, A.Y., Yoon, S.-O., Kim, S.G., Roux, P.P. and Blenis, J. (2008) Rapamycin differentially inhibits S6Ks and 4E-BP1 to mediate cell-type-specific repression of mRNA translation. Proceedings of the National Academy of Sciences of the United States of America 105, 17414–17419.

[194] Feldman, M.E., Apsel, B., Uotila, A., Loewith, R., Knight, Z.A., Ruggero, D. and Shokat, K.M. (2009) Active-site inhibitors of mTOR target rapamycin-resistant outputs of mTORC1 and mTORC2. PLoS biology 7, e38.

[195] Kang, S.A. et al. (2013) mTORC1 phosphorylation sites encode their sensitivity to starvation and rapamycin. Science (New York, N.Y.) 341, 1236566.

[196] Fujiwara, T., Oda, K., Yokota, S., Takatsuki, A. and Ikehara, Y. (1988) Brefeldin A causes disassembly of the Golgi complex and accumulation of secretory proteins in the endoplasmic reticulum. Journal of Biological Chemistry 263, 18545–18552.

[197] Tărlungeanu, D.C. et al. (2016) Impaired Amino Acid Transport at the Blood Brain Barrier Is a Cause of Autism Spectrum Disorder. Cell 167, 1481-1494.e18.

[198] Xu, J. et al. (2020) Intervening upregulated SLC7A5 could mitigate inflammatory mediator by mTOR-P70S6K signal in rheumatoid arthritis synoviocytes. Arthritis research & therapy 22, 200.

[199] Kanai, Y. (2022) Amino acid transporter LAT1 (SLC7A5) as a molecular target for cancer diagnosis and therapeutics. Pharmacology & therapeutics 230, 107964.

[200] The UniProt Consortium (2023) UniProt: the Universal Protein Knowledgebase in 2023. Nucleic acids research 51, D523-D531.

[201] Misumi, Y., Miki, K., Takatsuki, A., Tamura, G. and Ikehara, Y. (1986) Novel blockade by brefeldin A of intracellular transport of secretory proteins in cultured rat hepatocytes. Journal of Biological Chemistry 261, 11398–11403.

[202] Aryal, R.P., Ju, T. and Cummings, R.D. (2010) The endoplasmic reticulum chaperone Cosmc directly promotes in vitro folding of T-synthase. The Journal of biological chemistry 285, 2456–2462.

[203] Ju, T., Brewer, K., D'Souza, A., Cummings, R.D. and Canfield, W.M. (2002) Cloning and expression of human core 1 beta1,3-galactosyltransferase. The Journal of biological chemistry 277, 178–186.

[204] Kirchhoff, C., Habben, I., Ivell, R. and Krull, N. (1991) A major human epididymis-specific cDNA encodes a protein with sequence homology to extracellular proteinase inhibitors. Biology of reproduction 45, 350–357.

[205] Nakajima, K. et al. (2019) Lack of whey acidic protein (WAP) four-disulfide core domain protease inhibitor 2 (WFDC2) causes neonatal death from respiratory failure in mice. Disease models & mechanisms 12.

[206] Das, S. et al. (2019) Structural Organization and Dynamics of Homodimeric Cytohesin Family Arf GTPase Exchange Factors in Solution and on Membranes. Structure (London, England : 1993) 27, 1782-1797.e7.

[207] DiNitto, J.P., Lee, M.-T., Malaby, A.W. and Lambright, D.G. (2010) Specificity and membrane partitioning of Grsp1 signaling complexes with Grp1 family Arf exchange factors. Biochemistry 49, 6083–6092.

[208] Sharma, S. and Zhu, J. (2014) Immunologic applications of conditional gene modification technology in the mouse. Current protocols in immunology 105, 10.34.1-10.34.13.

[209] Efeyan, A. et al. (2013) Regulation of mTORC1 by the Rag GTPases is necessary for neonatal autophagy and survival. Nature 493, 679–683.

[210] Zhen, H. et al. (2015) Regulation of the plasma amino acid profile by leucine via the system L amino acid transporter. Bioscience, biotechnology, and biochemistry 79, 2057–2062.

[211] Egan, D., Kim, J., Shaw, R.J. and Guan, K.-L. (2011) The autophagy initiating kinase ULK1 is regulated via opposing phosphorylation by AMPK and mTOR. Autophagy 7, 643–644.

[212] Kim, J., Kundu, M., Viollet, B. and Guan, K.-L. (2011) AMPK and mTOR regulate autophagy through direct phosphorylation of Ulk1. Nature cell biology 13, 132–141.

[213] Dunlop, E.A., Hunt, D.K., Acosta-Jaquez, H.A., Fingar, D.C. and Tee, A.R. (2011) ULK1 inhibits mTORC1 signaling, promotes multisite Raptor phosphorylation and hinders substrate binding. Autophagy 7, 737–747.

[214] Jung, C.H., Seo, M., Otto, N.M. and Kim, D.-H. (2011) ULK1 inhibits the kinase activity of mTORC1 and cell proliferation. Autophagy 7, 1212–1221.

[215] Löffler, A.S. et al. (2011) Ulk1-mediated phosphorylation of AMPK constitutes a negative regulatory feedback loop. Autophagy 7, 696–706.

[216] Sarbassov, D.D. et al. (2004) Rictor, a novel binding partner of mTOR, defines a rapamycin-insensitive and raptor-independent pathway that regulates the cytoskeleton. Current biology : CB 14, 1296–1302.

[217] Banerjee, C., Mehra, D., Song, D., Mancebo, A., Park, J.-M., Kim, D.-H. and Puchner, E.M. (2023) ULK1 forms distinct oligomeric states and nanoscopic structures during autophagy initiation. Science advances 9, eadh4094.

[218] Klionsky, D.J. et al. (2016) Guidelines for the use and interpretation of assays for monitoring autophagy (3rd edition). Autophagy 12, 1–222.

[219] Demeter, A., Romero-Mulero, M.C., Csabai, L., Ölbei, M., Sudhakar, P., Haerty, W. and Korcsmáros, T. (2020) ULK1 and ULK2 are less redundant than previously thought: computational analysis uncovers distinct regulation and functions of these autophagy induction proteins. Scientific reports 10, 10940.

[220] Avrahami, L., Farfara, D., Shaham-Kol, M., Vassar, R., Frenkel, D. and Eldar-Finkelman, H. (2013) Inhibition of glycogen synthase kinase-3 ameliorates β-amyloid pathology and restores lysosomal acidification and mammalian target of rapamycin activity in the Alzheimer disease mouse model: in vivo and in vitro studies. The Journal of biological chemistry 288, 1295–1306.

[221] Dufner, A., Andjelkovic, M., Burgering, B.M., Hemmings, B.A. and Thomas, G. (1999) Protein kinase B localization and activation differentially affect S6 kinase 1 activity and eukaryotic translation initiation factor 4E-binding protein 1 phosphorylation. Molecular and cellular biology 19, 4525–4534.

[222] Qin, X., Jiang, B. and Zhang, Y. (2016) 4E-BP1, a multifactor regulated multifunctional protein. Cell cycle (Georgetown, Tex.) 15, 781–786.

[223] Shah, O.J., Anthony, J.C., Kimball, S.R. and Jefferson, L.S. (2000) 4E-BP1 and S6K1: translational integration sites for nutritional and hormonal information in muscle. American journal of physiology. Endocrinology and metabolism 279, E715-29.

[224] Bill, A., Schmitz, A., König, K., Heukamp, L.C., Hannam, J.S. and Famulok, M. (2012) Anti-proliferative effect of cytohesin inhibition in gefitinib-resistant lung cancer cells. PloS one 7, e41179.

[225] Xu, K., Gao, J., Yang, X., Yao, Y. and Liu, Q. (2013) Cytohesin-2 as a novel prognostic marker for hepatocellular carcinoma. Oncology reports 29, 2211–2218.

[226] Peterson, R.T., Beal, P.A., Comb, M.J. and Schreiber, S.L. (2000) FKBP12-rapamycin-associated protein (FRAP) autophosphorylates at serine 2481 under translationally repressive conditions. The Journal of biological chemistry 275, 7416–7423.

[227] Zhou, X., Clister, T.L., Lowry, P.R., Seldin, M.M., Wong, G.W. and Zhang, J. (2015) Dynamic Visualization of mTORC1 Activity in Living Cells. Cell reports 10, 1767–1777.

[228] Aliu, E., Kanungo, S. and Arnold, G.L. (2018) Amino acid disorders. Annals of translational medicine 6, 471.

[229] Brooks, D.L. et al. (2023) Rapid and definitive treatment of phenylketonuria in variant-humanized mice with corrective editing. Nature communications 14, 3451.

[230] Golbahar, J., Al-Jishi, E.A., Altayab, D.D., Carreon, E., Bakhiet, M. and Alkhayyat, H. (2013) Selective newborn screening of inborn errors of amino acids, organic acids and fatty acids metabolism in the Kingdom of Bahrain. Molecular genetics and metabolism 110, 98–101.

[231] Buonocore, F., Balys, M., Anderson, G. and Achermann, J.C. (2023) Investigating ultrastructural morphology in MIRAGE syndrome-derived fibroblasts using transmission electron microscopy. F1000Research 12, 155.

[232] Kaur, G. and Lakkaraju, A. (2018) Early Endosome Morphology in Health and Disease. Advances in experimental medicine and biology 1074, 335–343.

[233] Wang, Y. et al. (2009) Regulation of endocytosis via the oxygen-sensing pathway. Nature medicine 15, 319–324.

[234] Naslavsky, N. and Caplan, S. (2023) Receptor-mediated internalization promotes increased endosome size and number in a RAB4- and RAB5-dependent manner. European journal of cell biology 102, 151339.

[235] Claing, A., Chen, W., Miller, W.E., Vitale, N., Moss, J., Premont, R.T. and Lefkowitz, R.J. (2001) beta-Arrestin-mediated ADP-ribosylation factor 6 activation and beta 2-adrenergic receptor endocytosis. The Journal of biological chemistry 276, 42509–42513.

[236] Meecham, A., Cutmore, L.C., Protopapa, P., Rigby, L.G. and Marshall, J.F. (2022) Ligand-bound integrin αvβ6 internalisation and trafficking. Frontiers in cell and developmental biology 10, 920303.

[237] Shmuel, M., Santy, L.C., Frank, S., Avrahami, D., Casanova, J.E. and Altschuler, Y. (2006) ARNO through its coiled-coil domain regulates endocytosis at the apical surface of polarized epithelial cells. The Journal of biological chemistry 281, 13300–13308.

[238] Yamaoka, M. et al. (2016) PI3K regulates endocytosis after insulin secretion by mediating signaling crosstalk between Arf6 and Rab27a. Journal of cell science 129, 637–649.

[239] Maranda, B., Brown, D., Bourgoin, S., Casanova, J.E., Vinay, P., Ausiello, D.A. and Marshansky, V. (2001) Intra-endosomal pH-sensitive recruitment of the Arf-nucleotide exchange factor ARNO and Arf6 from cytoplasm to proximal tubule endosomes. The Journal of biological chemistry 276, 18540–18550.

[240] Tjelle, T.E., Brech, A., Juvet, L.K., Griffiths, G. and Berg, T. (1996) Isolation and characterization of early endosomes, late endosomes and terminal lysosomes: their role in protein degradation. Journal of cell science 109 (Pt 12), 2905–2914.

[241] Solomatina, A. (2020) The role of cytohesins in the regulation of immune responses. https://nbn-resolving.org/urn:nbn:de:hbz:5-57402.

[242] Oh, S.J. and Santy, L.C. (2010) Differential effects of cytohesins 2 and 3 on beta1 integrin recycling. The Journal of biological chemistry 285, 14610–14616.

[243] Frank, S.R., Hatfield, J.C. and Casanova, J.E. (1998) Remodeling of the actin cytoskeleton is coordinately regulated by protein kinase C and the ADP-ribosylation factor nucleotide exchange factor ARNO. Molecular biology of the cell 9, 3133–3146.

[244] Yang, J., Yao, W., Qian, G., Wei, Z., Wu, G. and Wang, G. (2015) Rab5-mediated VE-cadherin internalization regulates the barrier function of the lung microvascular endothelium. Cellular and molecular life sciences : CMLS 72, 4849–4866.

[245] Rodriguez-Gil, J.L. et al. (2019) NPC1 Deficiency in Mice is Associated with Fetal Growth Restriction, Neonatal Lethality and Abnormal Lung Pathology. Journal of clinical medicine 9.

[246] Sheth, J., Joseph, J.J., Shah, K., Muranjan, M., Mistri, M. and Sheth, F. (2017) Pulmonary manifestations in Niemann-Pick type C disease with mutations in NPC2 gene: case report and review of literature. BMC medical genetics 18, 5.

[247] Hayakawa, N. et al. (2014) The ADP-ribosylation factor 1 gene is indispensable for mouse embryonic development after implantation. Biochemical and biophysical research communications 453, 748–753.

[248] Suzuki, T. et al. (2006) Crucial role of the small GTPase ARF6 in hepatic cord formation during liver development. Molecular and cellular biology 26, 6149–6156.

[249] Gjeta, I., Sala, D., Bakalli, I., Celaj, E. and Kola, E. (2023) Surfactant Deficiency Causing Severe Pneumonia in a Child. Current health sciences journal 49, 134–138.

[250] Linder, M.D., Uronen, R.-L., Hölttä-Vuori, M., van der Sluijs, P., Peränen, J. and Ikonen, E. (2007) Rab8-dependent recycling promotes endosomal cholesterol removal in normal and sphingolipidosis cells. Molecular biology of the cell 18, 47–56.

[251] Naslavsky, N. and Caplan, S. (2005) C-terminal EH-domain-containing proteins: consensus for a role in endocytic trafficking, EH? Journal of cell science 118, 4093–4101.

[252] Schweitzer, J.K., Pietrini, S.D. and D'Souza-Schorey, C. (2009) ARF6-mediated endosome recycling reverses lipid accumulation defects in Niemann-Pick Type C disease. PloS one 4, e5193.

[253] Loh, W.P., Yang, Y. and Lam, K.P. (2017) miR-92a enhances recombinant protein productivity in CHO cells by increasing intracellular cholesterol levels. Biotechnology journal 12.

[254] Frye, K.B., Zhu, X., Khodjakov, A. and Kaverina, I. (2023) Unbiased Quantification of Golgi Scattering and Golgi-Centrosome Association. Methods in molecular biology (Clifton, N.J.) 2557, 529–541.

[255] Pennauer, M., Buczak, K., Prescianotto-Baschong, C. and Spiess, M. (2022) Shared and specific functions of Arfs 1-5 at the Golgi revealed by systematic knockouts. The Journal of cell biology 221.

[256] García, I.A. et al. (2017) CREB3L1-mediated functional and structural adaptation of the secretory pathway in hormone-stimulated thyroid cells. Journal of cell science 130, 4155–4167.

[257] Rohn, W.M., Rouillé, Y., Waguri, S. and Hoflack, B. (2000) Bi-directional trafficking between the trans-Golgi network and the endosomal/lysosomal system. Journal of cell science 113 (Pt 12), 2093–2101.

[258] van Bommel, D.M., Toonen, R.F. and Verhage, M. (2022) Vti1a/b support distinct aspects of TGN and cis-/medial Golgi organization. Scientific reports 12, 20870.

[259] Ramírez-Peinado, S. et al. (2017) TRAPPC13 modulates autophagy and the response to Golgi stress. Journal of cell science 130, 2251–2265.

[260] Wang, Y., Li, X., Zhou, Q. and Zhang, S. (2024) GOLPH3 knockdown alleviates the inflammation and apoptosis in lipopolysaccharide-induced acute lung injury by inhibiting Golgi stress mediated autophagy. Prostaglandins & other lipid mediators 174, 106865.

[261] Posor, Y., Jang, W. and Haucke, V. (2022) Phosphoinositides as membrane organizers. Nature reviews. Molecular cell biology 23, 797–816.

[262] Geiger, C. et al. (2000) Cytohesin-1 regulates beta-2 integrin-mediated adhesion through both ARF-GEF function and interaction with LFA-1. The EMBO journal 19, 2525–2536.

[263] Ong, Y.S., Tran, T.H.T., Gounko, N.V. and Hong, W. (2014) TMEM115 is an integral membrane protein of the Golgi complex involved in retrograde transport. Journal of cell science 127, 2825–2839.

[264] Ioffe, E. and Stanley, P. (1994) Mice lacking N-acetylglucosaminyltransferase I activity die at mid-gestation, revealing an essential role for complex or hybrid N-linked carbohydrates. Proceedings of the National Academy of Sciences of the United States of America 91, 728–732.

[265] Metzler, M., Gertz, A., Sarkar, M., Schachter, H., Schrader, J.W. and Marth, J.D. (1994) Complex asparagine-linked oligosaccharides are required for morphogenic events during post-implantation development. The EMBO journal 13, 2056–2065.

[266] Wang, Y. et al. (2010) Cosmc is an essential chaperone for correct protein O-glycosylation. Proceedings of the National Academy of Sciences of the United States of America 107, 9228–9233.

[267] Xia, L. et al. (2004) Defective angiogenesis and fatal embryonic hemorrhage in mice lacking core 1-derived O-glycans. The Journal of cell biology 164, 451–459.

[268] Alexander, W.S. et al. (2006) Thrombocytopenia and kidney disease in mice with a mutation in the C1galt1 gene. Proceedings of the National Academy of Sciences of the United States of America 103, 16442–16447.

[269] Hadar, N. et al. (2023) X-linked C1GALT1C1 mutation causes atypical hemolytic uremic syndrome. European journal of human genetics : EJHG 31, 1101–1107.

[270] Herzog, B.H., Fu, J. and Xia, L. (2014) Mucin-type O-glycosylation is critical for vascular integrity. Glycobiology 24, 1237–1241.

[271] Kudo, T. et al. (2013) C1galt1-deficient mice exhibit thrombocytopenia due to abnormal terminal differentiation of megakaryocytes. Blood 122, 1649–1657.

[272] Ioffe, E., Liu, Y. and Stanley, P. (1996) Essential role for complex N-glycans in forming an organized layer of bronchial epithelium. Proceedings of the National Academy of Sciences of the United States of America 93, 11041–11046.

[273] Zhang, T., Long, H., Li, J., Chen, Z., Wang, F. and Jiang, S.-W. (2020) WFDC2 gene deletion in mouse led to severe dyspnea and type-I alveolar cell apoptosis. Biochemical and biophysical research communications 522, 456–462.

Acknowledgements

I would like to thank my supervisor Prof. Dr. Waldemar Kolanus for entrusting me with this interesting project. In lively discussions, he provided insightful feedback and great advice, helping me to drive this project forward despite any drawbacks and obstacles we faced.

I also want to thank Dr. Bettina Jux, for the foundation of the project, the continuous assistance - especially at the end of the project - and the stimulating scientific exchange. Additionally, I would like to thank her for any advice – professional and personal, the high investment in the project, her feedback on my thesis, and a new understanding of the 80's.

For feedback on my thesis, I would also like to thank Nicole Dörffer, Helena Boll, Marlene Gottschalk, and Lillian Hickox.

I further want to acknowledge the members of my doctoral committee - Prof. Dr. Waldemar Kolanus, Prof. Dr. Jörg Höhfeld, Prof. Dr. Irmgard Förster, and Prof. Dr. Anton Bovier - for taking the time to evaluate my work.

I would like to express my gratitude to all collaborators, especially Prof. Dr. Jörg Höhfeld and his lab members, Prof. Dr. Felix Meissner with Dr. Sebastian Kallabis and Anushka Kudaliyanage, Dr. Marc Sylvester (Core Facility Analytical Proteomics, University of Bonn), and Andreas Buness and Dr. Farhad Shakeri (Core Unit for bioinformatics Data Analysis, Universitä of Bonn) for their interest in my project, their support and advice.

I am very grateful to the whole Kolanus and Kiermaier lab, former and present members: for the support, inspiring discussions, and coffee breaks making every day more enjoyable and "sweet". Special thanks go to Dr. Thomas Quast for any help and scientific advice, Nicole Dörffer for co-working on KO cells and in the library, Christa Mandel and Andrea Raths for supporting me endlessly during my project, all lab members covering daily and administrative business, which allowed me to focus on my work. Special thanks go also to the students who accompanied me during my journey, Fernanda Vasquez Raffo, Jan Niklas Krämer, Lina Awad, Paul Kolbe, Amirmohammad Khodabandeh, and Marie Kannengießer.

Appendix

I am really grateful to all the members of the LIMES Institute, for providing a wonderful and supporting work atmosphere.

Finally, I would like to thank my friends and family. There are no words to describe what your support and having you in my life means to me.

Appendix

Table 1: Relative abundance per fraction of proteins pooled in Fig. 3.13F-G

mTORC1		WT					KO					
Gene	Protein group	3 K	5 K	12 K	24 K	78 K	3 K	5 K	12 K	24 K	78 K	Exp.-No.
Mtor	Q9JLN9	0,198	0,250	0,152	0,154	0,246	0,174	0,194	0,187	0,205	0,240	1
		0,330	0,201	0,133	0,177	0,159	0,129	0,404	0,135	0,154	0,178	2
Akt1s1	Q9D1F4	0,197	0,253	0,155	0,235	0,160	0,186	0,210	0,162	0,244	0,198	1
Rptor	Q8K4Q0	0,358	0,264	0,128	0,117*	0,133	0,250	0,211	0,186	0,182	0,171	1
Deptor	Q570Y9	0,172	0,244	0,141	0,181	0,261	0,112	0,165	0,181	0,243	0,299	1
		0,177	0,217	0,179	0,204	0,223	0,131	0,185	0,182	0,223	0,278	2
Mlst8	Q9DCJ1	0,225	0,282	0,088	0,168	0,237	0,163	0,212	0,198	0,216	0,211	1
		0,190	0,268	0,165	0,199	0,178	0,134	0,206	0,205	0,201	0,254	2

mTORC2		WT					KO					
Gene	Protein group	3 K	5 K	12 K	24 K	78 K	3 K	5 K	12 K	24 K	78 K	Exp.-No.
Mtor	Q9JLN9	0,198	0,250	0,152	0,154	0,246	0,174	0,194	0,187	0,205	0,240	1
		0,330	0,201	0,133	0,177	0,159	0,129	0,404*	0,135	0,154	0,178	2
Deptor	Q570Y9	0,172	0,244	0,141	0,181	0,261	0,112	0,165	0,181	0,243	0,299	1
		0,177	0,217	0,179	0,204	0,223	0,131	0,185	0,182	0,223	0,278	2
Mlst8	Q9DCJ1	0,225	0,282	0,088	0,168	0,237	0,163	0,212	0,198	0,216	0,211	1
		0,190	0,268	0,165	0,199	0,178	0,134	0,206	0,205	0,201	0,254	2
Rictor	Q6QI06	0,113	0,122	0,152	0,240	0,373	0,088	0,110	0,159	0,211	0,431	1
		0,104	0,142	0,213	0,286	0,255	0,080	0,146	0,178	0,224	0,373	2
Telo2		0,148	0,189	0,188	0,228	0,248	0,106	0,105	0,146	0,236	0,407	1

Appendix

CYTH2		WT										
Gene	Protein group	3 K	5 K	12 K	24 K	78 K	Exp.-No.					
Cyth2	P63034	0,216	0,143	0,211	0,132	0,298	1					
Cyth2	P63034	0,057	0,144	0,099	0,312	0,388	2					

ARFs		WT					KO					
Gene	Protein group	3 K	5 K	12 K	24 K	78 K	3 K	5 K	12 K	24 K	78 K	Exp.-No.
Arf5	P84084	0,236	0,340	0,139	0,137	0,148	0,105	0,218	0,195	0,331	0,150	1
		0,164	0,204	0,209	0,286	0,136	0,189	0,246	0,245	0,189	0,132	2
Arf4	P61750	0,252	0,301	0,167	0,174	0,108	0,147	0,249	0,229	0,244	0,131	1
Arf4;Arf5	P61750;P84084	0,324	0,289	0,218	0,073	0,096	0,192	0,292	0,201	0,207	0,107	1
Arf1	P84078	0,257	0,380	0,248	0,070	0,045	0,066	0,292	0,227	0,355	0,060	1
Arf6	P62331	0,217	0,275	0,269	0,113	0,126	0,136	0,207	0,232	0,280	0,145	1
		0,140	0,196	0,230	0,256	0,177	0,179	0,197	0,242	0,210	0,172	2

V-ATPase		WT					KO					
Gene	Protein group	3 K	5 K	12 K	24 K	78 K	3 K	5 K	12 K	24 K	78 K	Exp.-No.
Atp6v0a2	P15920	0,228	0,358	0,225	0,094	0,094	0,186	0,239	0,262	0,199	0,113	1
Atp6v1a	P50516	0,291	0,365	0,200	0,082	0,062	0,204	0,312	0,260	0,143	0,081	1
		0,269	0,344	0,213	0,116	0,058	0,201	0,309	0,243	0,158	0,089	2
Atp6v1e1	P50518	0,291	0,355	0,220	0,075	0,059	0,226	0,296	0,250	0,155	0,073	1
		0,259	0,329	0,191	0,158	0,063	0,197	0,265	0,260	0,130	0,147	2
Atp6v0d1	P51863	0,234	0,387	0,209	0,088	0,082	0,142	0,293	0,285	0,193	0,086	1
		0,277	0,361	0,195	0,113	0,054	0,195	0,328	0,264	0,147	0,067	2
Atp6v1d	P57746	0,298	0,359	0,211	0,071	0,061	0,213	0,258	0,241	0,194	0,093	1
		0,265	0,337	0,227	0,106	0,065	0,198	0,282	0,246	0,172	0,102	2
Atp6v1b2	P62814	0,291	0,363	0,198	0,090	0,059	0,212	0,319	0,252	0,143	0,073	1

		0,266	0,333	0,228	0,116	0,057	0,197	0,297	0,256	0,166	0,083	2
Atp6v1b1;Atp6v1b2	P62814;Q91YH6	0,296	0,424	0,178	0,051	0,051	0,134	0,305	0,277	0,214	0,070	1
Atp6v1h	Q8BVE3	0,269	0,412	0,175	0,079	0,065	0,218	0,317	0,247	0,146	0,072	1
		0,281	0,361	0,193	0,101	0,065	0,194	0,309	0,249	0,166	0,082	2
Atp6v1f	Q9D1K2	0,248	0,409	0,188	0,082	0,073	0,134	0,274	0,270	0,234	0,087	1
		0,258	0,305	0,228	0,138	0,071	0,185	0,304	0,247	0,165	0,099	2
Atp6v1c1	Q9Z1G3	0,297	0,302	0,186	0,117	0,099	0,247	0,277	0,218	0,162	0,096	1
		0,228	0,348	0,195	0,144	0,085	0,200	0,333	0,224	0,151	0,092	2

Table 2: Overlapping proteins significantly re-distributed in differential centrifugation assay.
Protein Group, UniProt Accession Number; -Log (p-value), based on multidimensional significance testing; Delta sum, sum of absolute delta values for each fraction.

		-Log (p-value)	Delta sum	-Log (p-value)	Delta sum	Cluster
Genes	Protein Group	Exp.-No. 1		Exp.-No. 2		
Abca5	Q9D6X6	4,028	0,284	8,873	0,222	1
Acot7	P21619	3,107	0,340	3,538	0,270	1
Adamtsl3	Q8VHR0	14,696	0,505	17,608	0,481	1
Alkbh5	Q9CR39	4,567	0,339	7,597	0,440	1
Ap5b1	Q3TNL8	5,942	0,514	8,479	0,292	1
Arap1	Q8CJF7	3,062	0,269	10,084	0,474	1
Bax	Q02053	3,835	0,317	7,426	0,299	1
Bin3	E9QAT4	2,870	0,286	53,828	0,654	1
Blmh	Q499E4	3,697	0,367	3,491	0,476	1
Bltp1	Q9D5V6	5,553	0,543	10,818	0,292	1
C3	Q8R2U4	16,509	0,633	8,037	0,278	1

Appendix

Camk2g	P18052	3,373	0,242	5,756	0,208	1
Camsap2	Q8CIW5	34,580	0,833	24,383	0,879	1
Cdc27	Q9JI08	5,550	0,385	47,629	1,304	1
Cntrob	F8VPZ5	3,177	0,346	6,710	0,323	1
Col6a1	Q3TAP4	10,052	0,491	2,034	0,268	1
Col6a2	P08122	2,341	0,180	23,684	0,411	1
Crybg1	P50543	12,002	0,482	5,987	0,280	1
Csgalnact1	F6VAN0	2,258	0,175	16,851	0,371	1
Ctsl	Q7TMQ7	2,617	0,277	13,247	0,195	1
Ddx24	P18406	2,473	0,435	2,636	0,255	1
Ddx50	Q6NSU3	9,000	0,377	3,026	0,391	1
Degs1	O70281	9,120	0,567	27,436	0,206	1
Dnajc7	Q8C3Y4	3,604	0,233	7,581	0,230	1
Dock6	Q3TTY5	11,293	0,555	6,836	0,288	1
Eif2d	P02535	2,177	0,440	5,679	0,581	1
Emilin1	Q99K70	3,514	0,569	2,869	0,779	1
Epb41l5	Q5U4H9	2,569	0,377	12,200	0,406	1
Fads3	Q8C6M1	4,083	0,311	3,903	0,231	1
Focad	O35343	8,385	0,746	8,343	0,290	1
Frmd6	Q8K2Z2	9,471	0,460	2,644	0,427	1
Gemin8	Q6PD26	2,651	0,466	9,247	0,352	1
Glt8d1	Q02788	4,618	0,600	11,433	0,324	1
Grk5	E9PXF8	2,241	0,448	4,671	0,190	1
Hmces	P61211	2,637	0,363	6,071	0,203	1
Idh1	Q3TDK6	7,866	0,363	4,215	0,306	1

Igfbp7	O88844	14,558	0,436	7,175	0,335	1
Ip6k1	Q9JMH9	2,382	0,217	15,156	0,357	1
Irf2bp1	Q8CHP8	3,500	0,223	21,086	0,321	1
Isoc1	Q8R5L3	4,474	0,431	10,216	0,466	1
Itih3	P58802	11,484	0,498	19,704	0,224	1
Itpr2	Q922R8	33,190	0,699	2,606	0,777	1
Itprip	Q8BVL3	3,063	0,467	4,719	0,262	1
Khnyn	A3KGV1	2,402	0,506	3,880	0,312	1
Kifc3	Q60952	2,589	0,279	14,465	0,411	1
Kpna4	Q8BJQ9	4,520	0,602	5,397	0,368	1
Krt2	Q8CB62	6,292	0,508	5,628	0,520	1
Lama2	Q9DCD2	14,245	0,507	2,802	0,502	1
Lpcat1	A2AAE1	9,762	0,344	2,985	0,214	1
Lrrc8a	Q07813	7,440	0,693	3,753	0,193	1
Luzp1	Q9QYI3	6,980	0,472	3,352	0,710	1
Mad1l1	Q99PG2	2,905	0,352	12,486	0,336	1
Med1	Q9WUN2	2,247	0,218	23,951	0,211	1
Mta2	P06797	5,195	0,590	3,552	0,571	1
Nexn	Q8R570	11,671	0,441	9,973	0,402	1
Nolc1	E9PYG6	6,026	0,468	92,290	0,434	1
Ntmt1	Q3TIU4	10,327	0,416	7,065	0,493	1
Pacs2	Q9CXY9	2,545	0,374	4,530	0,429	1
Parp4	Q8R087	3,334	0,433	2,114	0,453	1
Pcdh18	Q91V64	7,891	0,512	18,584	0,473	1
Pde12	Q91V12	5,951	0,261	3,996	0,300	1

Pdia6	G3UXC7	23,591	0,603	14,036	0,140	1
Pds5b	Q80WG5	14,200	0,420	2,790	0,292	1
Pip4p1	Q3TWL2	131,734	1,113	4,546	0,337	1
Plcb4	Q8BVG4	2,136	0,308	2,901	1,410	1
Plcl2	P54728	3,754	0,349	2,182	0,244	1
Pms1	Q91X88	6,201	0,396	3,165	0,347	1
Polk	P39098	2,671	0,390	3,844	0,762	1
Pomgnt1	Q8BRV5	3,136	0,209	3,581	0,290	1
Prpf39	Q8BS45	5,165	0,625	11,900	0,210	1
Prss23	Q4VAA7	2,196	0,417	3,262	0,413	1
Ptpn11	Q8VDR9	16,614	0,470	3,642	0,346	1
Ptpn21	Q9EPL0	31,897	0,818	2,630	0,761	1
Pum3	P46935	2,333	0,417	3,708	0,971	1
Pus7l	Q8CFG0	2,515	0,474	3,823	0,462	1
Rad50	Q61581	22,120	0,503	2,828	0,304	1
Rasa1	Q8K354	3,113	0,210	12,672	1,017	1
Riok3	Q8BUE4	2,245	0,195	5,144	0,733	1
Rogdi	Q8VEB1	4,086	0,315	2,429	0,246	1
Rpgrip1l	O09005	15,230	0,401	2,949	0,374	1
Rps10	Q9JJ06	2,759	0,454	4,656	0,421	1
S100a11	Q8K394	7,316	0,574	2,087	0,442	1
Sart1	Q9JJE7	7,692	0,398	3,132	0,542	1
Sec23ip	Q61704	17,341	0,724	2,118	0,294	1
Sipa1l3	Q91W34	3,504	0,202	52,011	0,259	1
Smg1	P35235	27,087	0,985	2,490	0,403	1

Snap47	Q8R016	7,198	0,333	14,794	0,338	1
Syap1	Q91XA2	2,895	0,490	15,775	0,434	1
Sympk	Q9WTX8	5,681	0,308	6,666	0,990	1
Syne2	Q8K2V1	2,768	0,343	3,291	0,620	1
Synpo2	P70398	4,795	0,419	21,381	0,258	1
Tbc1d10a	Q99K41	6,689	0,531	86,073	0,605	1
Togaram1	Q7TPW1	17,417	0,478	7,842	1,090	1
Tpst1	Q6PD10	4,646	0,607	3,435	0,664	1
Ttc26	Q8C080	2,613	0,515	2,651	0,431	1
Tut7	Q6A070	31,138	0,681	110,031	1,365	1
Twnk	P01027	26,926	0,515	2,301	0,638	1
Usp20	Q99N17	2,232	0,247	9,006	0,387	1
Usp9x	P97355	2,431	0,284	12,643	0,547	1
Vps39	Q8K0U4	2,254	0,277	8,744	0,378	1
Wdr45b	P16092	2,287	0,259	2,340	0,603	1
Xab2	Q8K448	7,638	0,553	2,765	0,252	1
Xylt2	Q60675	20,514	1,003	26,385	0,192	1
Zc3h14	Q3TFD2	16,075	0,481	2,052	0,368	1
Actr1b	Q8BHE1	5,266	0,326	2,409	0,255	2
Ahctf1	Q91YE8	9,144	0,688	2,645	0,385	2
Aifm2	Q9DB90	2,469	0,429	2,932	0,258	2
Arl1	Q8CE46	4,986	0,379	10,277	0,253	2
Atf6	Q8VE10	2,604	0,279	2,264	0,588	2
Atn1	Q61043	2,762	0,494	3,513	0,291	2
B4galt7	Q8C0V9	15,752	0,581	9,362	0,217	2

Bcas3	O35231	5,110	0,576	4,560	0,388	2
Bod1l	E9Q5C9	11,111	0,399	9,054	0,852	2
Bud31	Q91UZ1	3,931	0,396	63,535	0,296	2
C1galt1	Q9QUG2	5,334	0,328	36,419	0,441	2
Cbr3	Q8K119	11,255	0,368	6,566	0,552	2
Ccn1	Q9QZD4	3,468	0,275	2,503	0,245	2
Cep250	Q925J9	4,441	0,304	3,539	0,508	2
Col4a2	Q8R5C5	2,727	0,477	3,119	0,722	2
Cyp4f16	Q9CR56	2,449	0,324	6,742	0,482	2
Dctn5	Q8K224	2,175	0,219	2,892	0,437	2
Dpp9	Q8CBE3	2,141	0,312	2,497	0,245	2
Dxo	Q62407	2,886	0,251	22,293	0,347	2
Dzip1l	Q5BLK4	39,255	0,664	131,630	0,310	2
Ercc4	Q4VA53	19,813	0,672	4,949	0,195	2
Ercc6	A2AKG8	14,919	0,519	5,344	0,386	2
Fgfr1	Q8CCN5	2,707	0,314	7,034	0,190	2
Golm1	Q8R3Y8	6,464	0,536	3,967	0,466	2
Hspa12a	Q6PGH1	2,525	0,344	3,493	0,454	2
Kiaa1671	Q9Z315	14,359	0,552	28,124	0,258	2
Kntc1	Q8BKX6	38,321	0,637	11,921	0,373	2
Krt10	O70348	2,383	0,501	7,369	0,442	2
Lmnb2	Q80X82	9,793	0,537	28,728	0,263	2
Man1a2	Q8BGS1	5,094	0,328	2,745	0,298	2
Mki67	Q99P88	3,259	0,271	2,890	0,381	2
Mrfap1	Q8R1M0	5,198	0,463	2,350	0,479	2

Mtmr10	Q9Z329	106,867	1,082	19,028	0,618	2
Mtss1	Q8CG73	23,594	0,740	9,151	0,406	2
Myo18a	Q8VHN8	2,858	0,309	4,890	0,469	2
Naa40	Q8BKS9	4,583	0,298	62,636	0,187	2
Nat10	O35126	2,353	0,238	2,861	0,281	2
Ncoa4	Q9DBU3	4,396	0,254	35,705	0,528	2
Nedd4	Q9CQL7	2,708	0,373	16,828	0,290	2
Nin	P63325	5,361	0,353	2,358	0,272	2
Nkiras2	O88622	3,116	0,325	4,357	0,333	2
Nudt16l1	Q4LDD4	5,894	0,423	6,852	0,281	2
Nup155	Q99MJ9	15,023	0,585	12,948	0,260	2
Odf2	P47968	3,022	0,261	3,657	0,299	2
Ogfr	G3X9J0	6,524	0,390	2,679	0,484	2
Parg	Q8R4U7	11,619	0,468	31,283	0,438	2
Pgp	Q8BJ05	24,381	0,933	4,238	0,520	2
Pigk	Q61211	3,934	0,325	25,474	0,267	2
Pigs	Q3V3Q7	5,050	0,536	4,587	0,329	2
Poc1a	Q04857	16,101	0,834	3,037	0,574	2
Ppp4r1	Q6ZWQ0	5,441	0,552	24,365	0,221	2
Ptpra	A0A0G2JG52	19,342	0,616	5,389	0,504	2
R3hdm4	Q4VBF2	2,135	0,348	20,632	0,541	2
Rad23b	Q62136	84,599	1,035	57,033	0,218	2
Rpia	Q3TSG4	8,958	0,302	11,581	0,335	2
Rragc	P70388	32,622	0,726	2,934	0,338	2
Rusf1	Q6NZC7	28,226	0,716	4,786	0,865	2

Sbf2	E9PVX6	2,457	0,234	3,020	0,297	2
Sec16a	E9PYK3	6,292	0,322	9,579	0,963	2
Smg9	Q8JZX3	3,354	0,251	28,827	0,349	2
Sms	E9Q6J5	3,112	0,256	39,847	0,570	2
Snx16	Q80U38	4,659	0,533	3,289	0,246	2
Snx17	Q9R190	9,579	0,395	5,405	0,227	2
Snx33	Q6ZPZ3	2,423	0,292	6,075	0,232	2
Speg	Q923T9	6,420	0,580	2,386	0,600	2
Sulf2	Q7TPM9	3,809	0,415	8,269	0,289	2
Tbk1	Q9JM98	2,508	0,234	12,275	0,554	2
Tsr1	A2A6Q5	9,650	0,435	132,194	0,375	2
Uba1	Q8C1B1	111,230	1,317	22,316	0,406	2
Wdr37	Q9QZB9	2,152	0,246	4,882	0,437	2
Wdr91	Q9ESV0	4,928	0,322	3,767	0,491	2
Wrap73	Q8R1S4	3,482	0,225	2,108	0,460	2
Zc3h4	Q5SWD9	3,068	0,328	6,397	0,315	2